UNIVERSITY OF BIRMINGHAM

Synthesis and characterisation of new materials for use in Solid Oxide Fuel Cells and Electrolysers

By

Matthew James
Supervisor: Prof Peter Slater
2nd Supervisor: Dr Paul Anderson

A thesis submitted to the University of Birmingham for a degree of Doctor of Philosophy

School of Chemistry

College of Engineering and Physical Sciences

University of Birmingham

16th of December 2022

Abstract

In this thesis, the work presented focuses on the development of anion doping strategies (Oxyanions and Halides) into a variety of different structures for potential use as cathodes within solid oxide fuel cells and electrolysers.

The thesis examines the use of phosphate doping of the mixed perovskite Mn/Fe system, $Sr_{2-x}Ca_xMnFeO_{6-\delta}$, to design a novel low-cost cathode material. The work shows the successful incorporation of phosphate into these systems and show that conductivities are higher than the previously reported silicon doped variant.

The work on $Ba_{1-x}Sr_xFeO_{3-\delta}$ systems demonstrates the successful incorporation of borate and characterises the effect on the structure and conductivity with a view to possible utilise as a cathode material in a ceramic fuel cell (H^+ or O^{2-} conducting). The incorporation of low levels of borate was shown to be sufficient to cause a change in cell symmetry to give a cubic perovskite structure.

Lanthanum germanate apatite was studied to try to confirm which oxide ion conduction mechanisms are present within the $La_{10}Ge_6O_{27}$ and $La_{10-x}Y_xGe_6O_{27}$ (x = 0, 1 and 2) structures with literature proposing two possible mechanisms; through the channel and perpendicular to the channel. Despite blocking the centre channel in the apatite structure with borate, the observation of high oxide ion conductivity provided support for an alternative oxygen interstitial conduction method perpendicular to the channel was presented. The addition of borate into the structure also introduced larger amounts of interstitial oxide ions, therefore increasing the conductivity in some of these systems.

The first use of two types of biopolymer, Iota and Kappa Carrageenan, was demonstrated as both a gelation agent and a precursor material with a novel sol-gel synthesis for the manufacture of $SrFe_{1-x}S_xO_{3-\delta}$ materials with comparable results to the standard high-temperature solid-state synthesis.

Finally, the successful synthesis of a range of K_2NiF_4 structured La doped Sr_2CoO_3F phases was demonstrated. Contrary to undoped Sr_2CoO_3F which required high pressure synthesis, La doping was shown to allow synthesis under ambient pressure. We also evaluated these materials for their potential applications as SOFC cathode/ FIB electrode materials via conductivity and thermal characterisation, with some showing high conductivities.

Acknowledgements

To begin I would like to thank my supervisor Prof Peter Slater for offering a place on this project. I would like to thank him from the bottom of my heart for his guidance, experience, advice, and empathy throughout my studies.

I would also like to thank Dr Paul Anderson for his role as my secondary supervisor.

Thanks to Dr Louise Male for her time teaching me the use of the Powder X-ray diffraction instruments as well as her expertise within crystallography which were invaluable to the start of the project. I would like to thank Professor Frank Berry, Dr Jose Marco and Dr Artur Majewski for the collection and analysis of Mössbauer Spectroscopy and Diltometery data presented in this thesis.

I would like to thank all members of the Slater group for the warm welcome when I moved to the group aswell as their support and wise words during the process. I would especially like to thank Abbey, Ivan, Josh and Mark for their contribution to my studies.

I would like to also give my thanks to the rest of the floor 5; past and present. The floor was a place of humour and friendship during my time there and long may that continue for the next cohort of students. A special mention to Dan and Rosie for putting up living with me for a year.

Finally, I would like to thank my family (Mum, Dad, Ben and Izzy) who have been with me throughout my entire academic studies. I'm grateful for all their support and encouragement and hope I've made them all proud.

Contents

Abbreviations

AAEMFC	Anion exchange membrane fuel cell
AFC	Alkaline Fuel Cell
ASR	Area specific resistance
BSCF	Barium strontium cobalt iron oxide
BSZF	Barium strontium zinc iron oxide
BZCY	Barium zirconia cerium yttrium oxide
CGO	Cerium gadolinium oxide
CHP	Combined heat and power
DEFC	Direct Ethanol Fuel Cell
DMFC	Direct Methanol Fuel Cell
HOR	Hydrogen Oxidation Reaction
H-SOFC	Proton conducting solid oxide fuel cell
ICE	Internal combustion engine
LNF	Lanthanum nickel iron oxide
LNO	Lanthanum nickel oxide
LSC	Lanthanum strontium cobalt oxide
LSCF	Lanthanum strontium cobalt iron oxide
LSCV	Lanthanum strontium cobalt vanadium oxide
LSGM	Lanthanum strontium gadolinium manganese oxide
LSM	Lanthanum strontium manganese oxide
MCFC	Molten carbonate fuel cell
MEA	Main Electrode Assembly
MIEC	Mixed ionic and electronic conductor
MPEC	Mixed protonic and electronic conductor
MPIEC	Mixed protonic, ionic and electronic conductor
MPOEC	Mixed protonic, oxide ion and electronic conductor
NASA	National Aeronautics and Space Administration
NiO	Nickel Oxide

OER	Oxygen evolution reaction
ORR	Oxygen reduction reaction
PAFC	Phosphoric acid fuel cell
PCCFC	Proton conducting ceramic fuel cell
PCFC	Proton conducting fuel cell
PEMFC	Proton exchange membrane fuel cell
SEC	Single electronic conductor
SOE	Solid oxide electrolyser
SOFC	Solid Oxide Fuel Cell
YSZ	Yttria stabilised zirconia or yttrium zirconia oxide

Chapter 1: Introduction

1.1 Critical materials in modern energy devices

As the global population is ever increasing, the need for energy storage devices in our modern day-to-day life is growing. From combined heat and power (CHP) for housing and manufacturing, electric vehicles and portable devices such as smartphones as well as a host of everyday devices require high performance energy storage materials. However, one of the largest issues relates to the supply of some critical materials and their sustainability.

Materials such as Pt, Ir, Ru and Pb are seen as either unsustainable (with a rising threat with increased usage), precious e.g (ever increasing tin price when combined with limited supply) or like other materials such as Li and Co are primarily mined within a certain regions or countries, meaning that there is a monopoly on price and supply. A possible solution would be to look at the recycling of the energy devices after use. However, as research continues within a field there are still extreme recycling challenges including accounting for technological advances in materials used are constantly changing as improving materials are found and the economic cost. (1) Until recycling and reclaiming of materials becomes economically viable or legislatively required, we should look at researching sustainable and low-cost materials. (2-3)

1.2 A case for a future hydrogen economy

Due to issues with critical materials along with global warming and the volatile cost of crude oil, there is need for unprecedented change to clean, abundant, renewable energy system across the globe[3]. Hydrogen, the most abundant element within the universe, meets all the mentioned criteria and is seen as a long-term future of energy storage for renewable energy generation (Solar, wind, tidal etc) ,working in tandem with batteries. (4-6)

Currently, the cost of conversion of markets of CO_2 producing energy (Oil and gas) to H_2 is remote due to the enormous cost of new infrastructure meaning that the introduction of H_2 will be minimal until 2025, a target for introduction by governments, and 2050 a goal for full conversion. (7)

In the short-term, the research and development of technology, to support lowering the cost and smooth transition for hydrogen markets to develop, with successful programs already in places in countries such as Japan (8) and Germany (9).

Fuel cell and electrolyser technology is a critical element of the hydrogen economy. However, this sector is currently in need of further research in numerous areas including the materials used, fabrication of cells, fuel development, testing of devices for performance and degradation analysis before being ready for wider commercialisation. (10)

1.3 History of fuel cells

Fuel cells are electrochemical devices that convert chemical energy into electrical energy. Electrolysers preform the reverse process. Fuel cells were first invented by William Grove, a Welsh scientist who published in 1838 his “Grove gas battery”. (11) Developed from his named primary cell (of platinum wires and sulfuric acid), Grove discovered that a constant electrical current could be achieved by forming a rudimentary cell using iron and copper and porcelain plate sheets immersed in a copper sulphate and dilute acid solution. (12)

It would take further research by Swiss scientist Christian Fredrich Schönbein to discover the working principle of a fuel cell by combining hydrogen and oxygen dissolved in water. (13)

Fuel cells transitioned into objects of scientific intrigue when Wilhelm Ostwald referred to the Grove gas battery as "lacking in practical relevance but noteworthy for its theoretical implications." This generated considerable debate regarding the validity of fuel cells in

supporting either the contact theory, which argues that electricity is produced through the physical interaction of materials, or the chemical theory, which attributes electricity generation to chemical reactions. Subsequent findings in the 19th century eventually affirmed the accuracy of the chemical theory. (14)

It's took until 1959, that major developments within the field were produced by Francis Thomas Bacon, a British engineer. Bacon developed a 5 kW stack of forty cells that were made by using activated electrodes made by porous nickel sheets and a liquid potassium hydroxide solution as the electrolyte, thus forming the first alkaline fuel cell (AFC). (15) The patent for such cells was acquired by Pratt and Whitney and were produced for the Apollo Space Program to provide electrical power. Although expensive, the cell was chosen for their high operating efficiency of around 60% compared to conventional heat engines and the presences of hydrogen and oxygen gases already being stored on-board the ship (The latter for life support). (16) Alkaline fuel cells would also be in the first fuel cell vehicle, a tractor-built by Harry Karl Ihrig for Allis-Chalmers, with a 15-kW stack producing 20 horsepower. (17)

A decade later, General Electric employees Willard Thomas Grubb and Leonard Niedrach made further developments by producing the first proton-exchange membrane fuel cell (PEMFC). The pair invented an electrolyte made from a sulfonated tetrafluoroethylene named Nafion which was used in the NASA Gemini spacecraft. However, PEMFC have only become a practical technology recently due to the high cost of materials including the platinum catalyst used as an electrode and the need for high purity hydrogen and oxygen. (18)

Although the space industry reverted to AFC's for the Apollo-Soyuz, Skylab and Shuttle programs, PEMFC's have seen major developments over the past half a century, mainly by the automotive industry. In 1993, Ballard power systems exhibited the first fuel cell bus in

Vancouver, Canada powered by a PEMFC. With a reported stack power density of 700 watts per kilogram, over the next 10 years, fuel cell buses were trialled in major cities across the world including Vancouver, London, Reykjavik, Perth and Beijing and by 2017, Ballard reported that their PEMFC's powered buses had travelled a cumulative distance of more than 10 million kilometres. Other developments include of PEMFC vehicles being demonstrated and becoming commercially available include automobiles, motorbikes, rail, maritime and UAV's. (10,19)

1.4 Types of fuel cells

There are many types of fuel cell, which relate to the materials used within the fuel cell. The naming nomenclature of fuel cell are related to the material used for the electrolyte. However, fuel cells broadly fall into two distinct types; low-temperature fuel cells and high-temperature fuel cells (also containing intermediate temperatures).

1.4.1 Lower temperature fuel cell types

Low temperature fuel cells have operating temperature below 400 °C. There are currently four main types of low temperature fuel cell; alkaline fuel cell (AFC) / anion exchange membrane fuel cell (AAEMFC), Phosphoric acid fuel cell (PAFC), Polymer exchange membrane fuel cell (PEMFC) and direct methanol / ethanol (DMFC or DEFC).

Generally, these types are most suited for transport and portable applications, given the lower temperatures and good start-up capabilities, but can be used within stationary applications such as grid balancing. Most low temperature fuel cells are only compatible with hydrogen gas unless otherwise stated. (20)

1.4.1.1 Alkaline fuel cell (AFC) and anion exchange membrane fuel cell (AAEMFC)

Alkaline fuel cells were one of the first fuel cell types to gain commercial success, notably being developed for NASA for the Apollo space programs and therefore these are the fuel cell type with the most maturity.

The basic design of an AFC cell contains a porous matrix which contains an aqueous alkaline solution usually potassium hydroxide, allowing for hydroxide ions to flow from the cathode to the anode. Electrode materials are usually formed of non-precious metal catalyst (usually nickel on the anode and silver at the cathode) which is loaded onto the porous carbon; however, spinel and perovskite structures have been researched as alternatives. The cell operating temperature is around 70 °C, lower than acidic fuel cells (PAFC and PEMFC). (21)

Due to the lower operating temperature and inexpensive materials within the cells, AFC's are easily the cheapest and have the longest lifetime than the rest of the fuel cell types. Compared with other low temperature fuel cell types, which use an acidic reaction mechanism, AFC's have higher electrical efficiency. This is due to accelerated kinetics within the cathode side (oxygen reduction reaction) as there are lower over potentials associated with high pH oxidation-reduction reaction.

Although the materials used within an AFC are inexpensive, the cells only run on pure fuels (Hydrogen and Oxygen) unlike other fuel cell types which could use oxygen from an air supply and potentially hydrocarbon fuels. This is related to the fact that potassium hydroxide reacts with poisons such as carbon dioxide, resulting in the formation of potassium carbonate within the electrolyte. Even very small concentrations of CO_2 can degrade the cell. Another unique aspect of AFC's compared to other cells, is the use of water as a reactant at the cathode side.

This can be an issue at the interface of the cathode and the electrolyte, as excess water may dilute the concentration of the alkaline solution within the electrolyte. (22)

Relatively recently, an adaption of AFC, Alkaline anion-exchange membranes fuel cells have generated considerable attention. (23-24) A simplification of the cell mechanism is the same as AFC however using a polymer-based electrolyte. The polymer usually has a functional group for ion-exchange to introduce OH^- species and thus facilitate hydroxide ion conductivity.

However, the issues with water management persists and ionomer stability within the electrolyte material are still challenging.

The AFC and AAEMFC have been shown to have wide potential applications including as water electrolysis cells, and with other variations of alkaline fuel cells (25) such as metal hydride fuel cells and direct borohydride fuel cells they are still being developed. (26)

1.4.1.2 Phosphoric acid fuel cell (PAFC)

Designed within the 1960's, phosphoric acid fuel cells were an early candidate for use in stationary applications, becoming commercialised in 2001.

The cell consists of an electrolyte of phosphoric acid immobilised within a porous SiC matrix, in a similar vein to AFC. However in contrast to AFCs, the cell requires precious-group metals as a catalyst (usually platinum) dispersed on a carbon sheet as an electrode material, which increases the cost compared to cell types using inexpensive anode/cathode materials.(27-28)

However, unlike other fuel cell types, the platinum is resistant to carbon monoxide poisoning, a key poison which can cause carbon deposition (carbon formation) within pores of electrodes. This is due to the fuel cell have a relatively high operating temperature of around

180 ^{o}C. Studies examining the use of a lower operating temperatures has shown that carbon monoxide poisoning increases with decreasing temperature. Despite the higher operating temperature, PAFC stacks are generally reliable, with good endurance and low stack failure.

One of the main disadvantages of running PAFC compared to a higher operating temperature fuel cell, is the poor efficiency. Electrical efficiency is usually no higher than 40% (mostly energy is lost as heat) and this is the lowest of most types of fuel cells; even with the utilisation of heat, the PAFC's can only exceed 80% which is much lower than MCFC stacks used within stationary applications requiring fuel cells to be compact. (29)

Due to the higher operating temperature, electrolyte evaporation can occur and so this requires replenishment. There is also an issue of the corrosive nature of phosphoric acid on the main electrode assembly (MEA).

A benefit of Phosphoric Acid Fuel Cells (PAFC) is their ability to operate on hydrocarbon fuels, like gasoline, owing to their relative resistance to carbon monoxide poisoning. Nonetheless, these fuels often contain sulfur, a common impurity found in most crude oil derivatives, which must be eliminated. Sulfur acts as a significant contaminant for platinum-based cells, necessitating its removal for efficient operation

1.4.1.3 Polymer exchange membrane fuel cell

Currently PEMFC are one of the most researched fuel cell types. (31) They contain a very thin polymer as an electrolyte, typically Nafion®. Nafion® is a sulfonated tetrafluoroethylene-based polymer which was discovered by DuPont scientist Walther Grot. It was made from one of the very first ionomers which has both neutral and ionising units. Its ionic properties along with good thermal and mechanical stability makes it a strong candidate compared to other

low temperature fuel cell polymer electrolytes. The Nafion® layer is sandwiched between platinum particles (the catalyst) coated onto a carbon support with teflon polymer coated in-between to prevent flooding.

PEMFC's are currently the leading fuel cell type with 42,600 units sold in 2018. (10) One of the advantages of PEMFC is the operating temperature of 80-90 ^{o}C. The electrolyte is hydrated with water to ensure optimum conductivity and therefore water must be prevented from evaporating, thus this has the lowest operating temperature of all fuel cell types. However, this lower temperature doesn't have a dramatic effect on the cell power density which is one of the largest of all fuel cell types. One of the other advantages, especially over high temperature fuel cell types, is the relatively short start-up capabilities leading to PEMFC being well suited for transportation applications, in addition to portable and stationary applications. PEMFC are currently being used to replace older fuel cell technology such as AFC and PAFC.

One of the leading disadvantages for PEMFC, especially compared to other technology such as the internal combustion engine and batteries, is the expensive materials used within the fuel cell. Platinum is expensive and the manufacturing cost of producing Nafion® adds additional expenditure. Another issue with PEMFC is that due to low operating temperatures, only pure hydrogen may be used with this fuel cell type. With all factors considered, PEMFC compared to diesel generators were found to be over 5 times more expensive (fuel cell cost of £4, 275 and generator cost of £825 per kW) over a 13,200- hour period (equivalent to 10 years' service). (19)

Additional issues with PEMFC types are their poor tolerance to any poison, such as carbon monoxide (32) and sulphur-containing compounds (33), especially compared to other fuel cell

types. There is also the problem of water management within the electrolyte, used to keep the nafion® material active, with issues such as water evaporation adding complexity to the PEMFC system.

1.4.1.4 Direct methanol fuel cell (DMFC) and direct ethanol fuel cell (DEFC)

Direct methanol fuel cells (DMFC) and direct ethanol fuel cells (DEFC) have an operational similarity to PEMFC,. (34-35) However, methanol or ethanol may be introduced at the anode, instead of hydrogen gas. The allowance of a liquid hydrocarbon fuel is achieved by alloying of ruthenium with the platinum at the anode electrode, which is helpful to increase resistance towards carbon monoxide poisoning.(36-37)

Developed within the 1990's, DMFC and DEFC are some of the newest types of fuel cell technology introduced. Due to the ease of carrying methanol and ethanol, their most viable applications would be within portable technology however there is competition within the space between fuel cell technology and non-fuel cell technology such as Lithium ion batteries. (19)

Whilst methanol and ethanol have higher energy density than lithium ion batteries (15 times greater), DMFC and DEFC types have very low power densities (30-100 mW cm^{-2}) which is a magnitude smaller than other fuel cell types such as hydrogen fed PEMFC (300-1000 mW cm^{-2}). This low power density is due to poor kinetics at the anode side of the cell and explains the lower efficiency than most other fuel cells (roughly 40% compared to average 60% for other fuel cell technology).

1.4.2 Intermediate and High temperature fuel cell types

Intermediate and high temperature fuel cell types are cells with a higher operating temperature than 400 °C. There are two distinct fuel cell types, molten carbonate fuel cells (MCFC) and solid oxide fuel cells (SOFC). (38)

The main difference between these cell types and low temperature variants is the use of a solid or molten materials as the electrolyte. This higher operating temperature is mainly useful with fuel flexibility, allowing for other hydrocarbon material such as natural gas, biofuels such as biomethane and bioethanol can be used. The higher operating temperature means longer start up times, therefore, MCFC and SOFC have applications as stationary power (and potentially heating) devices.

1.4.2.1 Molten carbonate fuel cell (MCFC)

In the 1950's. Dutch scientists G.H.J Broers and J.A.A Ketelaar began expanding their research on ionic conductivity within oxide materials and carbonate salts. (39) They reported the successful running of a cell made from a mixture of lithium, sodium and potassium carbonate doped magnesium oxide disks for six months. However, there were diffusion issues within the electrolyte material. Further research allowed for large demonstration devices to be shown within the 1990's (around 2 MW stack running on natural gas).

The fuel cell operation is different to low temperature devices. Carbon dioxide and oxygen enter the cell at the cathode side to form carbonate ions when an electric circuit is added. The carbonate ions travel through the "molten" electrolyte made from lithium and potassium carbonate held within a lithium/aluminium oxide matrix. The carbonate ions then react with

the fuel at the anode-electrolyte interface, to release electrons (hence electrical power) and produce water and carbon dioxide. (40)

MCFC have an operating temperature of 650 ^{o}C which allows for fuel flexibility. (41) However, this high temperature is useful given that unlike low temperature variants, carbon monoxide, which is usually a poison cell, can be utilised as a fuel at the anode side. Another advantage of MCFCs is the high resistance to fuel impurity (such as aforementioned CO and sulphur poisoning) (42-43) due to the high operating temperature. The high temperature also gives rise to faster kinetics which means that expensive, platinum group materials may be replaced by cheaper nickel-based materials within the cell.

The largest issue for MCFC is due to the reaction mechanism and temperature. The fuel cell requires carbon dioxide to be consumed at the cathode, to produce carbonate ions. Therefore, carbon dioxide produced at the anode must be recirculated around to the cathode. Thus, this adds not only complexity but also cost and additional space requirements for the system. MCFC's also rely on a corrosive electrolyte which also causes long term stability issues. Adding such issues with the engineering solution required to help hinder or prevent issues caused by higher temperatures (delamination of the electrodes, deformation of the fuel cell, leaking of the molten electrolyte and cracking of the cell under strain) the cost of running and replacing MCFC is currently higher than lower temperature fuel cell types AFC and PAFC.

1.4.2.2 Solid Oxide fuel cell (SOFC) and Proton conducting ceramic fuel cell (PCCFC)

Emil Baur, A Swiss scientist began experimenting on the electronic conductivity of solid oxide fuel electrolytes in the 1930's. (44) Using a mixed oxide material of zirconium, yttrium and cerium oxide, he found they had lower electronic conductivity values than expected and that

unwanted chemical reactions would not take place between the electrolyte material and the gases introduced. This work was replicated by Davtyan in the 1940's. (45)

This was the start of solid oxide fuel cell research leading Siemens to produce a tubular SOFC that showed no degradation after 1,500 hours.

Solid oxide fuel cells contain an oxide ion conducting ceramic as the electrolyte. (46-47) These ceramics only conduct oxide ions at high temperature, hence an operating temperature ranging from 500 to 1000 °C. The advantage of running at higher temperature is the fuel cell is fuel flexible and may use a variety of fuel such as hydrogen, biogas, natural gas and ammonia. (48-49)

Another advantage of operating at high temperature is that the SOFC may be used to produce recoverable heat as well as electrical power. Therefore, SOFC's have very high thermal and electrical efficiencies. (50-51)

While precious metals are common in low temperature fuel cells, the SOFC does not require such expensive materials due to the high operating temperature. The anode of a SOFC is usually a Ni/electrolyte cement and the cathode is usually a perovskite transition metal oxide material.

Much of the solid oxide fuel cell research is looking at the physical and mechanical stability of these materials at high temperature. SOFCs tend to be brittle and there are issues regarding gas sealing and thermal expansion, which require expensive solutions.

Although the high temperature lowers the risk of certain issues concerning degradation, there are two main issues regarding poisoning an SOFC operation. (52) When running on a hydrocarbon fuel, the porous anode material may be blocked by the formation of carbon; this

effect is described as carbon deposition. This occurs when side reactions such as methane cracking reaction occurs forming a solid carbon product, blocking the active sites and thus deactivating the cell. This deposition is especially significant on nickel-based materials, but can be alleviated by either doping with other metal oxides such as gold, ruthenium and palladium or by adding water or an oxidant into the fuel feed (such as a small amount of air). (53-55)

Other issues of running SOFCs with a hydrocarbon-based fuel is sulphur poisoning. (56) Contaminants within natural gas include sulphur containing compounds which may react on the surface of the nickel-based anodes and produce nickel sulphides. The nickel is used as a catalyst for the hydrogen oxidation reaction (HOR taking place at the anode). Nickel sulphide has no catalytic activity towards hydrocarbon fuels and therefore leads to the degradation of the performance of the cell. It is possible to remove sulphur from the fuel feedstock, however, this adds an additional cost to the process.

There has been much research on SOFC's within the last two decades. Specifically, the operation temperature has been reduced from 1000 °C to lower than 750 °C with improved performance. There has also been a move to improve the mechanical stability of the cells, which has moved from being provided by either the electrolyte or the anode material to a metallic support. SOFC research continues to look at the three largest factors affecting this fuel type; cost, reliability and durability.

A novel attempt at solving these barriers is the use of proton-conducting oxides to form a proton conducting solid oxide fuel cells, otherwise called proton conducting ceramic fuel cells. (57) (H-SOFC;s or PCFC). (58-60) Conventionally, SOFC have an electrolyte carrier ion of oxide ions formed by the Oxygen Reduction Reaction (ORR) within the cathode which are

transported through the electrolyte to the anode where the ions oxidise the chosen fuel. (61) PCFC's work by changing the carrier ion to protons which migrate to the cathode. Theoretically, the use of proton-conducting oxides would allow for low-cost material use, lower operating temperatures with a maximum of around 700 °C (as the electrolyte conductivity is higher), and many of the issues around durability and voltage losses being reduced.

One of the biggest development challenges facing this new technology is that while the voltage losses were caused within the anode materials (usually a nickel-based material that had issues with carbon deposition and sulphur poisoning) are reduced, similar issues emerge within the cathode materials. Cathodes are now required to be have good conductivity of proton and electrons, be highly stable at the operating temperature and highly oxidised atmosphere, to have a similar thermal expansion coefficient (TEC) as the electrolyte (Usually barium cerium yttrium zirconate, BZCY) and to provide good catalytic activity to the ORR. This is a challenging task.

1.5 Potential applications of ceramic based fuel cells/ electrolysers.

This section reports current usage and potential applications for high-temperature ceramic material-based fuel cells, mainly portable and stationary applications. Although transportation has also been demonstrated for SOFC's.

Shipments of SOFC have increased by over an order of magnitude (from 2,700 to 27,800) in the last 5 years, and now is the third bestselling fuel cell type (after PEMFC and PAFC). (10)

1.5.1 Stationary power & combined heat and power (CHP)

The majority of SOFCs currently commercially available are for stationary applications. This is due to the unique features of operating SOFCs (high operating temperature and heat as an output energy). Fuel flexibility, high-power density and high efficiencies make SOFC's potentially more effective at powering (and heating) buildings than low-temperature fuel cells.

There are two scales of fuel cells for stationary applications; Large and Small.

1.5.1.1 Large scale fuel cells

Large stationary fuel cells are fuel cells that have capacities of large than 100 kW and are one of the largest sectors within fuel cell technologies. With projections of a global market value worth £14 billion and global capacity of 4,000 MW by 2025. (8)

One of the leading issues for large urban areas is air quality. In 2011, nine UK cities broke their PM10 limits (particulate matter 10 micrometres or less in diameter) and the world health organisation estimated that poor air quality cost £1.1 trillion for the European economy. (62) Fuel cells offers low local pollution emissions and low noise emissions with potential systems having high efficiencies (>60%). Therefore, despite the high capital costs, fuel cells can be commercially viable in urban locations against traditional power systems i.e gas fuelled boiler or internal combustion engine, as there is strong regulation about pollution emitted or subsidies available in certain countries. These factors can only improve by further regulation and enforcement on emission along with decreases in cost for these systems as they are mass produced.

Currently, most large-scale fuel cells are either MCFC or PAFC as these were the first commercialised systems, and most urban areas having natural gas infrastructure already in place which can fuel them. (7) As of September 2022, London has had 3 large scale fuel cell systems installed within the city (2 MCFC and 1 PAFC) making it the largest fuel cell capacity city within Europe. Although MCFCs is currently in more demand and has higher electrical efficiencies. PAFCs have higher overall efficiency and are believed to become competitive when global production increases to 100 units per manufacturer (UPM), estimated to occur after 2025. (10)

Potential prospective sectors that may adopt fuel cells would be local authorities, hospitals, large housing associations and large business headquarters to project and market a green and eco-friendly marketing strategy.

Large fuel cell systems fuelled by hydrogen, usually from existing processes within the chemical industry, are possible, with AFC being the leading candidate type. However, the current hydrogen infrastructure is less mature than natural gas and therefore it is difficult to find suitable candidate buildings to implement, especially in urban areas. Another major issue for hydrogen fuelled AFC's is that commercialisations is reliant on the cost of hydrogen. Costs can be reduced by using by-product hydrogen from chemical industry processes.

Like MCFC, solid oxide fuel cells have the possibility to help reduce increase revenue for a large-scale system due to the potential use as a carbon capture and storage, however scope for such application is not projected to be available till beyond 2025.(63-65)

1.5.1.2 Small scale fuel cells

Small scale fuel cells can be used within housing to provide power to homes and provide heating, and are known as a CHP device (combined heat and power). The scaling of fuel cells stacks required is dependent on the size of the building (microCHP <2 kW for individual houses and 2-20 kW for shared residential services). With both types of energy being used the efficiency of fuel cell rises to over 90%, and with combination of low CO_2, fuel cells could be a replacement to central heating systems and conventional water boilers. In addition, the other advantages of fuel cell devices, such as low noise pollution, make them suitable for residential buildings. (7)

Commercialisation of these types of devices have started in countries such as Japan (66) and South Korea (67). However, these countries provide heavy subsidies for greener devices and other countries have been slow to develop their own sectors.

As for large scale fuel cells, natural gas is currently preferred to hydrogen. However, with hydrogen infrastructure becoming more mature, conversion will become viable, and would not require new infrastructure (new fuel cells within homes).

The current best-selling fuel cell type is PEMFC. However, because the limitations of the materials used within PEMFC, a fuel processor is required to convert the methane within natural gas to hydrogen gas. (68-70) SOFC's, which have been slowly introduced into the market can reform methane internally which provides a cost-cutting benefit. (68,71-73)

Within the next ten years, the production of micoCHP fuel cell devices is predicted to rapidly grow as they become more commercially viable, with some manufacturers already targeting

production of 10,000 a year for SOFC devices. Projections suggest a global market value of up to £19 billion with millions of units being sold world-wide. (19)

One of largest barriers for large-scale scale use of SOFC is to show the longevity of the device compared to gas boilers, which have a life expectancy of over 10 years. Another issue is the effect of long-term carbon deposition and sulphur poisoning on the SOFC anode electrodes which still needs addressing.

1.5.2 Portable Fuel Cell

Portable energy devices encompass a wide variety of applications from small energy requirements, such as laptops, mobile phones or portable chargers to larger portable generators for off-grid power such construction sites, market stalls and national parks.

Although there have been previous attempts to enter the smaller portable devices market, they have been relatively unsuccessful and battery devices have a monopoly on this section of the market, with fuel cells being available for very niche and remote applications.

However, portable generators larger than 1 kW would be more viable for the fuel cells than batteries, which have a long charge-up time but short-duration of use and would be possibly competitive against conventional petrol and diesel generators against which fuel cells can provide a quiet and clean alternative. (7)

SOFC's would potentially be a stronger option than other types of fuel cell due to its fuel flexibility allowing a range of fuels to be used. (74) However, PEMFC and DMFC are more mature device types and the choice of which fuel cell type is very much dependant on the buyer's requirements. Another issue for all types of fuel cell is the lack of familiarity with fuel cell technology with risk-adverse customers being hesitant to buy fuel cells along with the

issues within the supply-chain. However, Fuel cell devices used for portable applications have been projected up to have a market value to £5 billion by 2025. (7)

1.5.3 Unmanned Aerial Vehicles (UAV)

Transportation is a leading contributor to pollution and emissions across the globe. Although solid oxide fuel cells tend not be considered within this industry due to the higher operating temperature, there are niche possibilities for potential use; one being unmanned aerial vehicles (UAV's). (75-77)

Fuel cells technology generally are highly advantageous for potential use within UAV's compared to other technologies. Batteries have lower energy densities than fuel cell systems, and so a fuel cell powered UAV may travel far further than a UAV powered by batteries. Another advantage of fuel cell systems are that they are scalable, and so unlike internal combustion engines powered by diesel or petrol can be used in smaller applications with similar efficiencies.

The UAV's market has increased rapidly within the last 10 years and is now projected to be worth around $8 billion, and with a wide range of applications include military, commercial and hobbyist flyers, the market is projected to triple in value by 2025. (7) Military application and other services, such as surveillance, infrastructure maintenance, agriculture, deliveries and surveying require long-range flight-time. Lithium-ion and other types of batteries are insufficien to provide such range, with fuel cells being shown to provide enhanced endurance, approximately four times that of equivalent lithium-ion systems due to higher volumetric and gravimetric energy densities.

SOFC's have been developed for use within UAV's and have been shown to be successfully fuelled with propane, butane and liquefied petroleum gas (LPG). (78-81) PEMFC and DMFC have also been used to power UAV's and have an advantage due to SOFC's higher operating temperature. Another issue for fuel cell systems more generally requirement that if hydrogen is to be used for a low-emissions application, then the development of hydrogen storage materials such a metal hydride may be a limit factor on their use, with the reuse and recycling of such materials also an issue.

1.5.4 Use of Hydrogen in liquid fuel production

Although new regulations within Europe and other developed countries will prevent or hinder the sale of new transportation devices such as automobiles powered by hydrocarbons such as diesel and petrol, there is still expectation that there will still be a high demand for such fuel past 2030. (82) Therefore, there will still be a dependency on liquid fuels, especially looking wider to the larger- transport sector such as aviation and maritime.

Biofuels sourced from arable crops, a carbon-neutral process is currently the most viable option of producing liquid hydrocarbon fuels. However there are serious issues regarding this process, mainly the unpracticable changes on yield of crops for biofuels within a giving year, affected by weather and climate. There are also significant ethical issues regarding human starvation, sustainability impacts, biodiversity impacts, issues of cash crops and competition with other technological processes such as carbon capture and storage. (83-85)

A possible solution could be the production of liquid fuels using hydrogen produced via electrolysis technology in combination with carbon capture and storage technology. The operation mechanism of such a process would be the introduction of water for electrolysis with electricity being used from a renewable source such as solar panels or wind turbines.

The resulting electrolysis cell would produce hydrogen gas which when added to carbon dioxide from the air, biomass or waste product gas streams produces liquid hydrocarbon fuel via a catalytic reaction. One of the biggest benefits would be the ability to have a fuel flexible product within this process, dependant on the carbon dioxide and hydrogen reagent amount and catalytic process used. Potential fuels which may be produced include; methanol, ethanol, diesel, petrol, dimethyl ether and complex blends such as these contained within jet fuel.

A successful project of this type of operation is the Carbon Recycling Imitative (CRI) in Iceland (86-87), which uses geothermal energy to power its' electrolysis process and its' geothermal power plant as its' sources of carbon dioxide to produce methanol. The project currently produces 4,000 tonne per annum with further constructions for projects in the rest of Europe and China in development. CRI has also been shown to produce 90% savings of greenhouse gas emissions compared to petrol production via crude oil

Solid oxide electrolysis cells have already been shown to be a viable option within this process already. (8,88) A plant in Dresden, Germany, currently produces 160 litres a day of "blue crude" which can be converted into diesel. The process is slightly different to CRI as the hydrogen is produced via steam electrolysis via a SOEC which is used in both a reverse water-gas shift reaction and Fischer-Tropsch synthesis with carbon dioxide from the air. The advantage of using solid oxide electrolysis cells compared other fuel cells types is the improved efficiency and thus improved hydrogen production.

One of the largest drawbacks for this application is not the fuel cell technology but the cost of the renewable energy used. It's reported that 70-90% of the cost of the hydrogen from water electrolysis is due to the cost of electricity, therefore the viability is heavily reliant on

renewable energy becoming increasingly affordable. A possible solution would be government backed subsidies for this types of technology and renewable energy used.

1.5.5 Hydrogen production

Currently, there two factors limiting the use of mainstream use of hydrogen as a fuel which are the lack of infrastructure for bulk (several thousand tonnes of H_2 a year) production of hydrogen, and the lack of conversion of pipelines and distribution network to transport the H_2. (89) The former issues are expected to be solved by an increase in capacity within the next 10 years as demand for hydrogen within transport sector increases. (8) However, demand for hydrogen is expected to exponentially rise towards 2050 with a UK government modelling predicts that hydrogen demand will range from 2.7 million tonnes of hydrogen to 18 million tonnes of hydrogen a year if at "full contribution mode". The larger value would require 23,000 electrolysers (size of 10 MW at 50% efficiency). (8,10)

There are several ways of producing hydrogen, with numerous methods currently being researched.

The most common form of hydrogen production currently, is the steam reforming of hydrocarbons (SMR). (90-92) Whilst this technology is currently is not ideal, due to the production of CO_2, it currently is the preferred method of 95% of hydrogen production. This form of hydrogen production is called "brown hydrogen" due to use of non-renewable energy or materials (Natural gas within this example). However, increasing technological advances within carbon capture technology (CCS) may be used within the set-up of SMR and thus be more environmentally friendly, named "blue hydrogen production" use of non-renewable energy or materials by reusing waste products. Other "Blue" methods may include coal gasification with CCS. (93-95)

The alternative to SMR, would be water electrolysis. Although non-renewable sources may potentially be used as the form of electrical production, ideally, energy from renewable sources such as wind, solar, wave and tidal power would be used, defined as “green hydrogen production”, use of renewable sources of energy and materials. (96) Other technologies which may be described as “green” is the gasification of biomass with CCS, by-product hydrogen production from chlor alkali plants and ethylene plants and photo-electrochemical and thermochemical cycles. However, these other “green forms” of hydrogen are in their infancy and would not expect commercial use until after 2025. (97-99)

1.5.5.1 Hydrogen production from water electrolysis via ceramic electrolysers

Large scale electrolysis is available currently. However, commercial barriers include high cost, especially when compared to SMR. The largest variable in cost is within the choice of renewable energy sources chosen and its current operating cost. Therefore, electrolysers require high efficiency to maximise the use of electricity and obtain the best “value-for-money” from their electricity source.

Currently, Alkaline electrolysers are globally the largest electrolyser type, within PEM electrolysers growing rapidly. However, both types have issues regarding costs. Alkaline electrolysers would require further research into its electrode coatings and PEM electrolysers require a new low-cost catalyst. Anion Exchange membrane electrolysis is also being developed. (100-102)

Solid oxide electrolyser cells (SOEC) have the potential to provide large cost reductions, due to their high efficiency. Potential formation of large-scale solid oxide electrolysis plants may also be beneficial as a form of heating for neighbour communities. However, as with fuel cell technology, cost is still the largest barrier. (102-107)

1.6 Current materials used as electrodes within fuel cell types

1.6.1 Platinum

Platinum has been the state-of –the-art metal catalyst used throughout most of the history of fuel cell technology, especially at low temperatures. Its performance in the adsorption and dissociation of gases makes it an ideal electrode material. Platinum also has useful properties in being inert to HOR and ORR reactions. (108-109) However, as cost as a raw material and rarity makes it very difficult to be mass-produced and stay commercially viable within the long-term. Ultimately, the need for the reduction in the amount of platinum within the cell is the deciding factor for the commercialisation of low temperature fuels cells.

Previous work on increasing surface area and controlling particle size have reduced the catalyst loading required, however, more research is needed. A successful example of a commercially available, platinum-containing device is a catalytic converter used within the automotive industry, to curb emission from internal combustion engine vehicles (ICE) showing the viability by reducing the platinum loading. Another alternative is the use of alloying with other precious metals such as rhodium and ruthenium, although issues regarding cost and sustainability are still present. (110)

1.6.2 Nickel compounds

Nickel has a lower catalytic activity than platinum and other precious metals (cobalt included). However, nickel has a significantly reduced cost compared to these other metals. (111-112) Therefore, it can be used in fuel cells with higher operating temperature such as MCFC, SOFC's and PCCFC, which have faster reaction kinetics at the electrodes, meaning catalytic performance is less of an issue.

1.6.3 Perovskites and related structures

Research, especially within SOFC materials, has looked at novel oxide structures for optimising the highest efficiency at the lowest given operating temperatures. Currently, the optimal materials for cathodes are perovskite materials. (113-114)

Based on the mineral of the same name, the ideal perovskite structure is a based on a formula of ABO_3. The A site is usually a large cation from either alkaline earth metal group or rare earth metal group. The B site is generally a small cation transition metal group. O usually defines oxygen but can be replaced by another anion such as fluorine, nitrogen or hydroxide ion.

Perovskite may be visualised in two forms. The A cation in the centre of the structure, whilst B cations are arranged on the corner of the cube, with the oxygen or anions contained on the edge of the cube. The other visualisation is the in-verse with B cation central and A cation on the corners. Although a perfect perovskite structure, has cubic symmetry. Different relationships between bond distances and between cation-anion radius size may distort the structure to a lower symmetry, The likelihood of such a distortion can be predicted by the Goldschmidt tolerance factor. (113,115)

Equation 1: Goldschmidt tolerance factor

$$t = \frac{r_A + r_O}{\sqrt{2}\,(r_B + r_O}$$

Where:

t = Goldschmidt tolerance factor

r_A = Radius of the A cation

r_B = Radius of the B cation

r_o = Radius of the anion

The composition of a perovskite can vary greatly and allows it for wide variety of properties to be optimised for applications. Perovskite structured materials which display proton-conducting or oxide-conducting along with electrical conductivity are of most interest in the application of SOFC electrodes.

This section discusses the basis of perovskite and perovskite-based structures used in electrode material research and specifically developments of cathodes for in oxygen-ion and proton-ion electrolyte SOFC's.

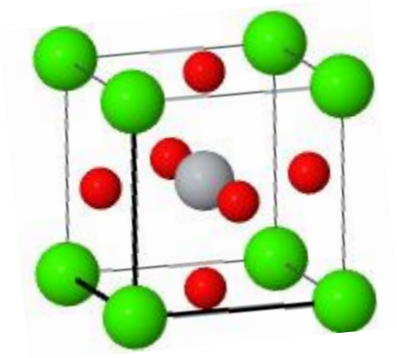

Figure 1.1. Cubic Perovskite structure, ABO_3 Structure

1.6.3.1 Cathode perovskite materials

Cathodes ideally need to be mixed ionic electronic conductors (MIEC) and traditionally, the choice of material has predominately of been perovskite type (ABO_3). The traditionally employed material is lanthanum strontium manganite (LSM or $La_{1-x}Sr_xMnO_3$). (116-117) Doping the material with strontium was found to enhance the mixed variance of the manganese (Mn^{3+}/Mn^{4+}) forming a p-type semiconductor material. The mixed valance means LSM has high catalytic activity for the ORR. However, the material has poor oxygen ion conductivity. Efforts have been made to combine the material in a composite with yttria-stabilised zirconia, (a well-used electrolyte material) to combat the poor ion conductivity at lower temperatures. However, issues remain with the use of YSZ due to it decreasing the performance of the cells. (118)

A similar cathode material is lanthanum strontium cobalt oxide (LSC or $La_{1-x}Sr_xCoO_3$). (119-120) LSC has been found to have improved cell performance, especially when used with cerium gadolinium oxide (CGO) electrolytes. The main research of this material is looking at how to reduce the materials high thermal expansion coefficient (TEC) in comparison to other materials within the cell. The main interest appears to be focussed on either doping with Fe

($La_{1-x}Sr_xCo_{1-y}Fe_yO_{3-\delta}$, LSCF) which improves high temperature stability and reduces TEC, or forming other Co containing perovskites for low temperature uses i.e. Gadolinium strontium cobalt oxide (GSC or $Gd_{1-x}Sr_xCoO_3$) (121) and samarium strontium cobalt oxide (SSC or $Sm_{1-x}Sr_xCoO_3$). (122)

Substitution of lanthanum for another alkaline earth metal such as barium has also been investigated. $Ba_{0.5}Sr_{0.5}Co_{1-x}Fe_xO_{3-\delta}$ (BSCF), combines the cubic structure of LSCF but with strong amount of oxygen vacancies at low temperature. (123-124) The substitution increases the oxidation state of the B-site metals and the mixed A-site prevents oxygen vacancy ordering, increasing ion conductivity. However, this material has lower stability than LSM and LSCF and may form a hexagonal structure at intermediate temperature (700-900 ^oC). Further optimisation found that doping with small amounts of lanthanide produced a high performing cathode. (125-127)

Another material, which has gained much interest due to it not containing cobalt is $Ba_{1-x}Sr_xFe_{1-y}Zn_yO_{3-\delta}$ (BSZF). The material has been shown to show similar ionic and electronic conductivity compared to BSCF and improved durability. However, the material has a large TEC at temperatures above 700 ^oC.

Recently, research into the implementation of perovskite materials on the anode side of the cell has attracted interest.

1.6.3.2 Anode perovskite materials

A strong candidate to replace NiO/YSZ is LSCV ($La_{1-x}Sr_xCr_{1-y}V_yO_{3-\delta}$). (128) Nickel oxide is known to be severely poisoned when a cell is fuelled with a hydrocarbon, leading to coking and carbon deposition occurring. LSCV was tested within in a cell fuelled with propane and

demonstrated no effects of coking over 30 cycles of 30 minutes. (129) This result suggests that perovskite structured anodes may improve long-term stability whilst using hydrocarbons as a fuel.

LSCM ($La_{1-x}Sr_xCr_{1-y}Mn_yO_{3-\delta}$), has shown similar performances to that of LSCV, (130) with improved use with hydrocarbon fuels compared to NiO/YSZ and has been further optimised with cerium and palladium doping. (131-132) Specifically, doping of cerium on the A-site of the perovskite has shown an improvement in the tolerance to the other poison of anode materials, sulphur. Testing showed that there was no presence of degradation after 120 hours operation. The material has been shown to result in low polarization resistances when mixed with YSZ and using this anode gave a cell power density within a cell of 177 mW cm^{-2} at 850 ^oC.

Due to the reducing conditions at the anode side of the cell, a perovskite material must be highly stable at within these conditions. Early work began on the perovskite $SrTiO_3$ due to it's stability under reducing conditions. However, the material has poor conductivity. (133)

Doping $SrTiO_3$ on both sites, has been shown to give improved performances. Examples include doping of Lanthanum on the A-site (134), and Niobium doping on the B-site which have both shown improved compared to un-doped $SrTiO_3$. (135)

1.6.4 Ruddlesden-popper phase materials as cathodes

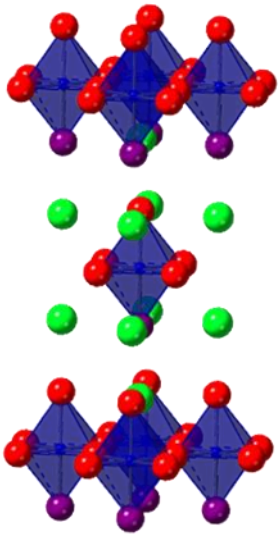

Figure 1.2. Example of a Ruddlesden-Popper Phase, K_2NiF_4 Structure

In terms of the material structure, an alternative to perovskites are the Ruddlesden-Popper phase materials ($A_{n+1}B_nO_{3n+1}$), where an increase in n means more distortions. (53,136) Their structures consist of perovskite blocks separated by rock salt units (Figure 1.2). They can show good electronic conductivity as well as oxide ion conductivity. The most researched of these materials is $La_2NiO_{4+\delta}$ (an n = 1 system). There has also been testing of the material which has been doped on the Ni sites. Materials chosen have included Co, Fe and Cu (137) and all have been shown to perform well with lanthanum strontium gallium manganate electrolytes (LSGM). However, all types of these Ruddlesden-Popper structures have also shown reactivity with numerous electrolytes including CGO and YSZ, thus reducing the effectiveness of the cell. A variety of higher order (n>1) $La_{n+1}Ni_nO_{3n+1}$ are also being researched for fuel cell applications.

Modifications of rare earth metals on the A-site have been explored, with Pr_2NiO_4 demonstrating a notable power density of 487 mW cm^{-2} at 800°C. This indicates its promising potential for application in high-temperature Solid Oxide Fuel Cells (SOFCs). (138)

1.6.5 Double perovskites

Another perovskite related structure is receiving much interest are double perovskites ($AA'B_2O_{6-\delta}$). Usually the A-site is a mixture of alkaline earth metals and rare earth metals of barium and praseodymium or neodymium e.g $PrBaCo_2O_{6-\delta}$ and $NdBaCo_2O_{6-\delta}$. The mixed site tends to A-site cation ordered, which leads to higher oxygen vacancies at lower temperatures. (113,139)

Further testing of such material is still required, especially optimisation of long-term stability and compatibility with electrolyte materials.

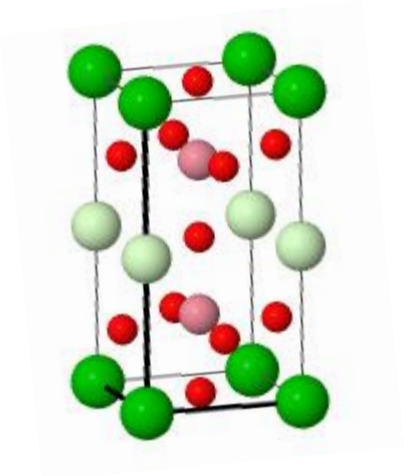

Figure 1.3. Double perovskite phase, $AA'B_2O_{6+\delta}$ structure

1.6.6 Pyrochlore

Pyrochlores have also attracted interest, These have a fluorite related structure which been distorted by the mixture of cations. The formula of the these materials is $A_2B_2O_7$ (Figure 1.4) and they have been shown to have a range of applications such as electronic insulators and low temperature superconductors. (114)

Ru based pyrochlore materials have been shown to have promising performances at lower temperature within the literature. $Ba_2Ru_2O_7$ is the best performing pyrochlore with testing showing area specific resistance (ASR) of around 0.03 Ω cm^{-2} at 700 ^oC. (46, 140-141)

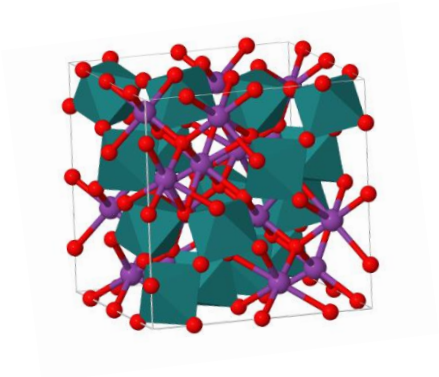

Figure 1.4. Pyrochlore phase, A_2BO_7 structure

1.7 Anion-doping strategies

Traditionally, in SOFC material design, both electrolyte and electrode conductivities have been optimised via doping with aliovalent cations of similar sizes (as seen in section 1.6). However, more recently, a variety of anion-doping strategies have been illustrated as being able to stabilise phases that would otherwise not be obtained under ambient pressure. (142)

1.7.1 Oxyanion doping strategies

Prior studies of perovskite-type cuprate superconducting materials such as $YBa_2Cu_3O_{7-x}$ showed the propensity of the perovskite structure to accommodate oxyanions (carbonate,

borates, nitrate, sulphates and phosphates). The central cations of the oxyanion occupied the B cation site of the perovskite structure, with the oxide ions filling 3 or 4, (depending on the oxyanion) of the 6 available anion sites surrounding the B site. These stable empty anion sites allowed for the stabilisation of phases which were previously not possible under ambient pressure synthesis routes, for example $Sr_2CuO_2CO_3$, $Ba_4ScCu_2O_{7-x}CO_3$. (143-148)

Further work showed that oxyanions could also be incorporated into other perovskite systems with borate and carbonate doping successfully including into manganese and iron and rare earth containing systems, for example in $Sr_5Mn_4O_{10}CO_3$ (149), $Sr_4Mn_{3+x}B_{1-x}O_{10}$ (150) $Ba_3Yb_2O_5CO_3$ (151) and Ruddlesden Popper phase $Sr_4Fe_{3-x}(CO_3)_xO_{10-4x}$. (152-154)

More recently, it has been shown that oxyanions (phosphate, silicate and sulphate) can be incorporated into $Ba_2In_2O_5$. (155-156) $Ba_2In_2O_5$ has a ready ability to accommodate oxide ion vacancies ($x > 0.5$) with an ordering of vacancies forming the brownmillerite structure ($Ba_2In_2O_5$). Studies showed that oxyanion groups, such as phosphate could be doped into the In sites to give $Ba_2In_{2-x}P_xO_{5+x}$ ($x = 0.1$-0.3) changing the structure from orthorhombic to cubic at room temperature. Due to the cubic structure having disordered oxide ions, an improvement in the ionic conductivity was observed. Further studies showed that oxyanions doped $Ba_2In_2O_5$ showed proton conductivity due to water incorporation. Therefore, oxyanion doped brownmillerite structures became of interests as potential SOFC electrolytes.

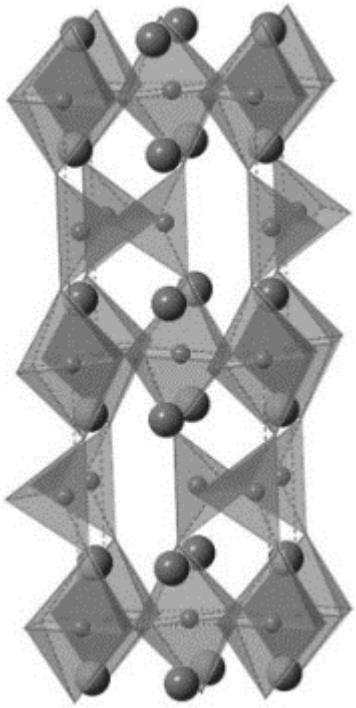

Figure 1.6. Brownmillerite structure $Ba_2In_2O_5$

Work was extended on other types of oxyanion doped brownmillerite structures for example, $Ba_2Sc_2O_5$ and $Ba_2Sc_{2-x}Ga_xO_5$ with the addition of Ga doping shown to improve the CO_2 stability of the material. (157-158)

Additional work also demonstrated the potential for the oxyanion doping strategy to be used within candidate SOFC electrode materials. For example, both $SrMnO_3$ and $SrCoO_3$ have been shown to successfully incorporate phosphate, sulphate and silicate within the structure. (159-161) A phase change was observed when oxyanions were introduced, changing from a hexagonal to a cubic cell. The incorporation of oxyanions meant an increase in oxygen vacancies causing a reduction in the oxidation state of the B-site cation (Mn and Co) leading to an increase in the average size of the B cation, thus altering the tolerance factor and favouring the cubic perovskite. The reduction of the average oxidation state of the B cation

led to an increase in conductivity of 2 orders of magnitude, leading to these materials being of interests as SOFC cathode materials.

Other perovskite analogues have also been further studied for their potential as SOFC electrode materials for example, $CaMnO_3$, $Sr_{1-x}Ca_xMnO_{3-\delta}$, $Ba_{1-x}Sr_xCo_{0.8}Fe_{0.2}O_{3-\delta}$, $SrFeO_{3-\delta}$ and the Ruddlesden Popper phase $Sr_4Fe_3O_{10-\delta}$. (161, 162-167)

1.7.2 Fluorine doping

An early example of tailoring properties using fluorine doping was the incorporation of fluorine into Sr_2CuO_3 (an insulator) to form $Sr_2CuO_2F_{2+\delta}$ (a superconducting material ($T_c \approx$ 46K)). In this material, the introduction of F in the interstitial sites raises the Cu oxidation state and introduces superconductivity. (168) One of the key challenges with such fluorine incorporation approaches is the thermal instability of the resultant oxide fluoride. In this particular case, it can be related to the high thermodynamic stability of SrF_2, such that it will tend to act as a thermodynamic "sink" for the fluorine. Consequently, attempts to prepare $Sr_2CuO_2F_{2+\delta}$ by a standard high temperature solid state route are unsuccessful and will simply give a mixture of SrF_2 and $SrCuO_2$. Therefore, the aforementioned low temperature fluorination of a structurally related oxide precursor is required, in this case fluorination of Sr_2CuO_3 with F_2 gas at low temperature (200°C) gives the superconducting $Sr_2CuO_2F_{2+\delta}$ phase. The low temperature allows for fluorine insertion and substitution for oxygen, but limits cation migration thus preventing decomposition. One can therefore consider a simplified energy profile (Figure 1.7), where there is a low activation energy for the fluorination of Sr_2CuO_3 to give $Sr_2CuO_2F_{2+\delta}$, while there is a higher activation energy for the substantial cation migration to give the thermodynamically stable product mixture of SrF_2 and $SrCuO_2$. Thus,

provided the fluorination is done at low temperature, one can stop at the metastable intermediate phase, $Sr_2CuO_2F_{2+\delta}$.

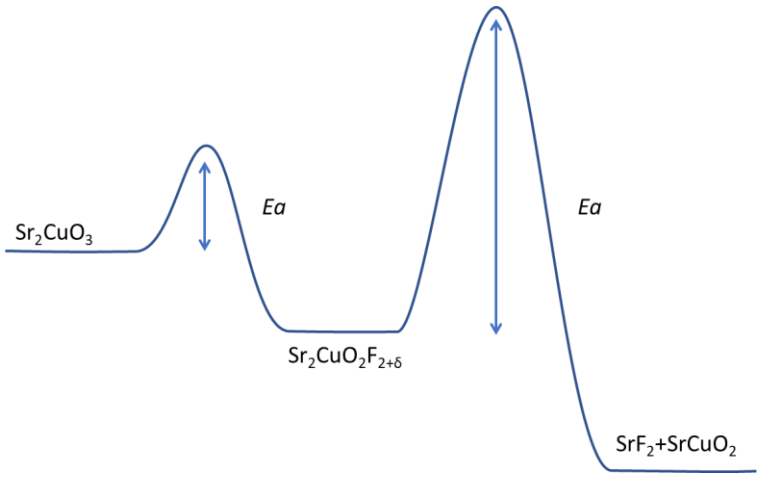

Figure 1.7 Simplified energy profile for the fluorination of Sr_2CuO_3. Provided the temperature of reaction is kept low, the reaction can be stopped to give the metastable $Sr_2CuO_2F_{2+\delta}$. Higher temperatures allow the second activation energy to be overcome resulting in a mixture of SrF_2 and $SrCuO_2$.

Whilst early work focused on the use of gaseous reagents, such as F_2 and NF_3 gas, this approach led to difficulties in controlling the level of fluorination, as well as safety concerns regarding the toxicity and handling of these gases. To overcome such issues; solid state fluorination reagents were investigated. These included NH_4F, XeF_2 and MF_2 (M = Cu and Zn) however there are challenges associated with each of these reagents. (169) Of these latter reagents NH_4F attracted the most interest; however, the low thermal decomposition temperature of this phase tended to mean that a large excess of reagent was required, and this fact, coupled with the water by-product which tended to facilitate material decomposition, meant that typically large impurities were observed. Consequently, there was a need for another fluorine containing compound, which had higher decomposition

temperature (more in line with the fluorination temperature required), and so fluorine containing polymer reagents were investigated and shown to be highly effective reagents for the synthesis of these oxide fluoride phases. In particular Poly(vinylidene fluoride) PVDF and other F containing polymers (e.g. poly(tetrafluoroethylene) (PTFE)) were shown to be successful in preparing a range of perovskite related oxyfluorides e.g. $Ca_2CuO_2F_2$ and $Sr_2TiO_3F_2$ with the main benefit being that the amount of fluorine incorporation could be controlled through the amount of polymer added.

Since the first demonstration of fluorination with PVDF, the use of such Fluorine containing polymers (mainly PVDF and PTFE) has attracted significant use for low temperature (below 400 °C) fluorination of oxide systems. (170) More recently such polymers have also been used to fluorinate thin film oxide precursor with reports of successful fluorination at temperatures as low as 150 °C. (171) The fluorination reaction using these polymers can be either performed in air or N_2. Air heat treatment ensures ready decomposition of the polymer and complete burn off of any C by products. With N_2 treatment, the presence of C in the polymers means that additional reduction can occur, and so this can be potentially used to direct the synthesis of heavily reduced transition metal oxide fluoride systems.

1.8 Project aims

The project primarily focuses on the synthesis of novel materials for the application as cathodes for solid oxide fuel cells/ solid oxide electrolysers (SOFC/SOE). A range of materials including perovskite, and Ruddlesden Popper phases have been identified as promising candidates for further research.

To improve the electrical conductivity required for within SOFC electrodes, oxyanion (carbonates, borate, silicate, phosphate and sulphate) doping was investigated. In all cases,

characterisation to determine the purity of samples was carried out by powder X-ray diffraction, thermogravimetric analysis and Mössbauer Spectroscopy. If purity was established, 4-probe DC conductivity measurements were carried out to determine the variation of conductivity with temperature.

With regards to benchmarking materials, literature suggest that a conductivity that is higher than 100 S/cm at 600 ^{o}C is acceptable for SOFC/SOEC cathode materials. (172) If any series of material did not reach this threshold, the series be adapted or considered for an alternative application. If materials showed promise i.e. high conductivity compared to currently used SOFC cathode materials, further conductivity measurements such as ASR (Area-specific resistance) and fuel testing would be conducted.

Where some series of materials has lower conductivities than expected compared to standard SOFC cathode materials, potential alternative applications are mentioned at within the conclusions of the chapters.

1.9 References

1. X Jinqiu, H Thomas, R Franci, K Lum, J Wang, B Liang, *J. Power Sources*, **177,** 512-527 (2008)
2. European Chemical Society, https://www.euchems.eu/euchems-periodic-table/, (accessed June 2019)
3. R Pachauri, L Meyer, *Climate Change 2014 Synthesis Report,* Intergovernmental Panel on Climate Change, IPCC, Geneva, Switzerland, (2015)
4. B Sørensen, G Spazzafumo, *Hydrogen and Fuel Cell: Emerging Technologies and Applications*, Academic Press, 3rd edition, (2018)
5. J Rifkin, *The Hydrogen Economy,* Jeremy P Tarcher, (2004)
6. P Hoffmann, *Tomorrow's Energy: Hydrogen, Fuel Cells, and the Prospects for a Cleaner Planet.*
7. D Hart, J Howes, B Madden, E Boyd *Hydrogen and Fuel Cells: Opportunities for Growth, A Roadmap for the UK,* E4tech and Element Energy, United Kingdom, (2016)
8. K Horiuchi, *ECS Trans*, **57,** 3-10 (2013)
9. International association for hydrogen energy, *Electronic Newsletter*, IAHE, Tennessee, United States of America, **10,** 6, December 2018.
10. D Hart, F Lehner, S Jones, J Lewis, M Klippensten, *The Fuel Cell Industry Review 2018,* E4tech, United Kingdom, (2019)
11. A Appleby, *J. Power Sources,* **, 29,** 3-11 (1990)
12. W Grove, *Note sur une Pile Voltaique d'une grande energie construtruite; communication de M Becquerel; Comptes Rendus,* **8**, 497 (1839)
13. R Oesper, *J. Chem. Educ.*, **6**, 4, 677 (1929)
14. G Harper, *Fuel Cell Projects for the Evil Genius,* McGraw- Hill Education Tab, United Kingdom, (2008)
15. K Williams, *Biogr. Mems Fell. R. Soc,* **39, (**1994)

16. *US Pat.,* US2969325A, (1961)

17. National Museum of American History, https://americanhistory.si.edu/collections/search/object/nmah_687671, (accessed Sep 2022)

18. Smithsonian National Air and Space Museum, https://airandspace.si.edu/collection-objects/fuel-cell-gemini-cutaway, (accessed Sep 2022)

19. D Hart, J Howes, B Madden, E Boyd *Hydrogen and Fuel Cells: Opportunities for Growth Mini roadmaps (appendix to roadmap report),* E4tech and Element Energy, United Kingdom, (2016)

20. A Kirubakaran, S Jain, R Nema, *Renew Sust Energ Rev,* **13,** 2430-2440 (2009)

21. A Appleby, F Foulkes, *Fuel Cell Handbook,* Van Nostrand Reinhold, New York, 1st Edn, (1989)

22. K Kordesch, V Hacker, J Gsellmann, M Cifrain, G Faleschini, P Enzinger, R Fankhauser, M Ortner, M Muhra, R Aronson, *J. Power Sources,* **86,** 162-165 (2000)

23. G Merle, M Wessling, K Nijmeijer, *J. Membrane Sci,* **377,** 1-35, (2011)

24. J Varcoe, P Atanassov, D Dekel, A Herring, M Hickner, P Kohl, A Kucernak, W Mustain, K Nijmeijer, K Scott, T Wu, L Zhuang, *Energy Environ. Sci.,* **7,** 3135-3191 (2014)

25. B MacDonald, A Rowe, *J. Power Sources,* **161,** 346-355 (2006)

26. N Choudhury, R Raman, S Sampath, A Shukla, *J. Power Sources,* **143,** 1-8 (2005)

27. M Watanabe, K Tsurumi, T Mizukami, T Nakamura, P Stonehart, *J. Electrochem. Soc,* **141,** 2659-2668 (1994)

28. N Sammes, R Bove, K Stahl, *Curr Opin Solid St M,* **8,** 372-378 (2004)

29. J Aragane, T Murahashi, T Osaka, *J. Electrochem. Soc.*, **135,** 844-850 (1988)

30. A Iodanidis, P Kechagiopoulous, S Voutekakis, A Lemonidou, I Vasalos, *Int, J. Hydrog, Energy,* **31,** 1058-1065 (2006)

31. S Peighambaroust, S Rowshanzamir, M Amjadi, *Int. J. Hydrog. Energy.,* , **35,** 9349-9384 (2010)

32. C Bonnet, L Lacaze, S Ronasi, S Basse, F Laqicque, *Chem. Eng. Sci.,* **65,** 3050-3058 (2010)

33. T Lopes, V Paganin, E Gonzalez, *J. Power. Sources.,* **196,** 6256-6263 (2011)

34. S Sharma, B Pollet, *J. Power Sources,* 96-119 (2012)

35. A Serov, C Kwak, *Appl Catal B,* **90,** 313-320 (2009)

36. A Hamnett, *Catal Today,* **38**, 445-457 (1997)

37. E Antolini, *J. Power Sources,* , **170,** 1-12 (2007)

38. S Singhal, K Kendall, *High-temperature Solid Oxide Fuel cells: Fundamentals, Design and Applications,* Elsevier Science, (2003)

39. M Schenke, G Broers, J Ketelaar, *J. Electrochem. Soc.,* **113,** 404 (1966)

40. S Cavallaro, N Mondello, S Freni, *J. Power Sources,* **102,** 198-204 (2001)

41. N Cherepy, R Krueger, K Fiet, A Jankowski, J Cooper, *J. Electrochem. Soc.,* **152,** A80-A87 (2005)

42. D Cao, Y Sun, G Wang, *J. Power Sources,* **167,** 250-257 (2007)

43. A Sammells, S Nicholson, P Ang, *J. Electrochem. Soc., **1**27,* 350-357 (1980)

44. H Kragh *Bull. Hist. Chem.,* **40,** 74-85 (2015)

45. L Blomen, M Mugerwa, *Fuel Cell Systems,* Springer Science, *(*1993)

46. A Orera, P Slater, *Chem. Mater.,* **22**, 675-690 (2010)

47. J Kilner, *Annu. Rev. Mat. Sci.,* **44**, 365-393 (2014)

48. A Stambouli, E Traversa, *Renew. Sust. Energ. Rev.,* **6**(5), 433-455 (2002)

49. C Laycock, J Staniforth, M Ormerod, *Dalton Trans.,* **40,** 5494-5504 (2011)

50. B Hobbs, A Tseung, *Nature,* **222***,* 556-558 (1969)

51. N Mahato, A Banerjee, A Gupta, S Omar, K Balani, *Prog. Mater. Sci.,***72,** 141-337 (2015)

52. T Takahashi, H Iwahara, *Energy Convers.*, **11**(3), 105-111 (1971)

53. I Sliverwood, N Hamilton, J Staniforth, C Laycock, S Parker, M Ormerod, D Lennon, *Catal Today.,* **155,** 319-325 (2010)

54. C Laycock, J Stanifoth, M Ormerod, *J. Electrochem. Soc.,* **16**(50),177-188 (2008)

55. I Sliverwood, N Hamilton, C Laycock, J Staniforth, M Ormerod, C Frost, S Parker, D Lennon, *Phys. Chem. Chem. Phys.,* **12,** 3102-3107 (2010)

56. A Hauch, A Hagan, J Hjelm, T Ramos, J. Electrochem. Soc., **161,** 6 *(*2014)

57. M Marrony, *Proton-Conducting Ceramics*, Pan Stanford Publishing, Boca Raton, 1ST edition, (2015)

58. K Kreuer, *Annu. Rev. Mat. Sci.,* **33**,333-359 (2003)

59. H Iwahara, H Uchida, S Tanaka, **9**(2), 1021-1025 (1983)

60. N Minh, *J. Am. Ceram. Soc.,* **76**(3), 563-588 (1993)

61. H Iwahara, *Solid State Ion.,* 77, 289-298 (1995)

62. WHO Regional Office for Europe. Economic cost of the health impact of air Cop enhagen: OCED; (2015) **https://www.euro.who.int/__data/assets/pdf_file/0004/276772/Economic-cost-health-impact-air-pollution-en.pdf** (Accessed Sep 2022)

63. E J Naimaster, A K Sleiti, *Energy Build,* **61**,153-160 (2013)

64. P Marocco, M Gandiglio, M Santarelli, *Energy Reports,* 8709-8721 (2022)

65. A Alns, A Sleiti, *Sustain. Energy Technol. Assess.,* 101615 (2021)

66. H Ren, W Gao, *Energy Build,* **42**(6)853-861 (2010)

67. Y Jung, J Kim, H Lee, *Energy Build,* **193**, 201-215 (2019)

68. L Barelli, G Bidini, F Gallorini, A Ottavio, *Int. J. Hydrog. Energy.,* **36**(4), 3206-3214 (2011)

69. J Romdhane, H Louahlia, M Marion, *Energy Build,* **166**, 93-108 (2018)

70. Y Yung, H Zhang, P Yan, K Jermsittiparsert, *Int. J. Hydrog. Energy.,* **45**(11), 6970-6981, (2020)

71. S Farhad, F Hamdullahpur, Y Yoo, *Int. J. Hydrog. Energy.,* **35**(8), 3758-3768 (2010)

72. L Nousch, M Hartmann, A Michaelis, *Processes,* **9**(7), 1113 (2021)

73. J Kupecki, M Skrypkiewicz, M Wierbicki, M Stepien, *Int. J. Hydrog. Energy.,* **42**(5), 3487-3497 (2017)

74. N Margaritis, L Blum, P Barfalsky, D Bohmann, S Ceschini, Q Fang, D Federmann, J Kromer, R Peters, R Steinberger-Wilckens, *ECS. Trans.,* **68**, 209 (2015)

75. G Giacoppo, O Barbera, N Briguglio, F Cipitì, M Ferraro, G Brunaccini, E Erdle, V Antonucci, *Int. J. Hydrog. Energy.,* **42(**46), 28022-28033 (2017)

76. M Bahari, M Rostami, A Entezari, S Ghahremani, M Etminan, *Fuel.,* **319**, 123796 (2022)

77. A D Meadowcroft, S Howroyd, K Kendall, M Kendall, *ECS Trans.* **57,** 451 (2013)

78. H Sumi, S Nakabayashi, T Kawada, Y Uchiyama, N Uchiyama and K Ichiahara, **,** *ECS Trans.* **91**, 149 (2019)

79. K Kendall, B Liang, M Kendall, *ECS Trans.***, 78**, 237 (2017)

80. M Kendall, A Meadowcroft, K Kendall, *ECS Trans.* **57,** 123 (2013)

81. G Beveniste, M Pucciarelli, M Torrell, M Kendall and A Tarancon, *J. Clean. Prod.,* **165**, 312-322 (2017)

82. A Bauen, A Chase, C Chudziak, J D Ouwens, B Denvir, N Owen, R Ripken, M v d Berg, F Vuille, *A harmonised Auto-Fuel biofuel roadmap for the EU to 2030,* E4tech, United Kingdom, (2013)

83. M V Rodionova, R S Poudyal, I Tiwari, R A Voloshin, S K Zharmukhamedov, H G Nam, B K Zayadan, B D Bruce, H J M Hou, S I Allakhverdiev, *Int. J. Hydrog. Energy.,* **, 42**(12), 8450-8461 (2017)

84. X Cai, X Zhang, D Wang, *Environ. Sci. Technol.,* **45** (1) 334-339 (2011)

85. S J Malode, K K Prabhu, R J Mascarenhas, N P Shetti, T M Aminabhavi, *Energy Convers. Manag.***, 10**, 100070 (2021)

86. B Denvir, R Taylor, A Bauen, G Toop, S Alberici, *Novel Low Carbon Transport Fuel and the RTFO: sustainability implications,* e4tech, United Kingdom *(*2015)**,**

87. A. Goeppert, G A Olah, G K Surya Prakash, *Green Chemistry: An Inclusive Approach,* **, 3.26**, 919-962 (2018)

88. A Heintzel, *ATZ Worldwide,***120**, 10-15 (2018)

89. J D Holladay, J Hu, D L King, Y Wang, *Catal. Today.,* **139** (4), 244-260 (2009)

90. Y Matsumura, T Nakamori, *Appl. Catal.,* **258**, 107-114 (2004)

91. P G Krishna, C Kanchi, H H Lou, *Chem. Eng. Res. Des,* 1956-1968 (2012)

92. H Zhang, Z Sun, Y H Hu, *Renew. Sustain. Energy Rev.,* **, 149**, 111330 (2021)

93. M Yu, K Wang, H Vredenburg, *Int. J. Hydrog. Energy.,* **46** (41) 21261-21273 (2021)

94. M H A Khan, R Daiyan, P Neal, N Haque, I MacGill, R Amal, *Int. J. Hydrog. Energy.,* **, 46** (44) 22685-22706 (2021)

95. H Ishaq, I Dincer, C Crawford, *Int. J. Hydrog. Energy.,* **47** (62) 26238-26264 (2022)

96. I Dincer, *Int. J. Hydrog. Energy.,* **37** (2) 1954-1971 (2012)

97. D-Y Lee, A Elgowainy, Q Dai, *Appl. Energy.,* **217**, 467-479 (2018)

98. I Rossetti, A Tripodi, G Ramis, *Int. J. Hydrog. Energy.,* **45** (17) 10292-10303 (2020)

99. H Yoneyama, H Sakamoto, H Tamura, *Electrochim. Acta.,* **20**(5), 341-345 (1975)

100. M David, C Ocampo-Martinex, R Sanchez-Pena, *J. Energy. Storage.,***23**, 392-403 (2019)

101. D S Falcao, A M F R Pinto, *J. Clean. Prod.,* **261**, 121184 (2020)

102. B Zhang, L Fan, R B Ambre, T Liu, Q Meng, B J J Timmer, L Sun, *Joule.,* 1408-1444 (2020)

103. G Schiller, A Ansar, M Lang, O Patz, *J. Appl. Electrochem.,* **39**, 293-301 (2009)

104. M N Manage, D Hodgson, N Milligan, S J R Simsons, D J L Brett, **, 36** 10) 5782-5796 (2011)

105. X Yue, J T S Irvine, *J. Electrochem. Soc.,* **159**(8) F442 (2012)

106. X Yang, J T S Irvine, *J. Mater. Chem.,* **18**, 2449-2354 (2008)

107. A Nechache, S Hody, *Renew. Sust. Energy Rev.,* **149**, 111322 (2021)

108. C Duan, J Tong, M Shang, S Nikodemski, M Sanders, S Ricote, A Almansoori, R O'Hayre, **349**, 1321-1326 (2015)

109. C Lamy, S Rousseau, E Belgsir, C Couranceau, J Leger, *Electrochim. Acta.,* **49**(22-23), 3901-3908 (2004)

110. S Lister, G Mclean, *J. Power Sources,* **130,** 61-76 (2004)

111. T Kawadam N Sakai, H Yokokawa, M Dokiya, M Mori, T Iwata, *J. Electrochem. Soc.,* **137,** 3042-3047 (1990)

112. H Koide, Y Someya, T Yoshida, T Maruyama, *Solid State Ion.,* **132,** 253-260 (2000)

113. A West, *Solid State Chemistry and it's Applications,* Willy-Blackwell, 2nd edition, (2014)

114. E Moore, L Smart, *Solid State Chemistry: An Introduction,* CRC Press, 4th edition, (2012)

115. Norsk Geologisk Tidsskrifft, **8,** 201-219 (1925)

116. S Jiang, *J. Mater. Sci.* **43**(21), 6799-6833 (2008)

117. J Irvine, J L M Rupp, G Liu, X Xu, S Halie, X Qian, A Snyder, R Freer, D Ekren, S Skinner, O Celikbilek, S Chen, S Tao, T H Shin, R O'Hayre, J Huang, C Duan, M Papac, S Li, V Celorrio, A Russell, B Hayden, H Nolan, X Huang, G Wang, I Metcalfe, D Neagu, S G Martin, *J. Phys. Energy,* **3**, 031502 (2021)

118. G Stochniol, E Syskakis, A Naoumidis, *J. Am. Ceram. Soc.,* ***7*8**(4),929-932 (1995)

119. J Liu, A Co, S Paulson, V Birss, *Solid State Ion.,* **177**(3-4) 377-387 (2006)

120. I Taniguchi, R Van Lanschoot, J Schoonman, *Solid State Ion***, 156**(1-2) 1-13 (2003)

121. Y Takeda, H Ueno, N Imanishi, O Yamamoto, N Sammes, M Phillipps, *Solid State Ion.,* **86-88**, 1187-1190 (1996)

122. H Fukunaga, M Koyama, N Takahashi, C Wen, K Yamada, *Solid State Ion.,* **132** (3), 279-285 (2000)

123. Z Shao, S Haille, *Nature,* **431,** 170 (2003)

124. M Arnold, T Gesing, J Martynczuk, A Feldhoff, *Chem. Mater,* **20**(18), 5851-5858 (2008)

125. P Muller, H Störmer, M Meffert, L Dieterle, C Niedrig, S Wagner, E Ivers-Tiffee, D Gerthsen, *Chem. Mater.,* **25**(4), 564-573 (2013)

126. F Lang, H Jiang, H Luo, J Caro, A Feldhoff, *Chem. Mater.,* **23**(21), 4765-4772 (2011)

127. S Primdahl, J Hansen, L Grahl-Madsen, P Larsen, *J. Electrochem. Soc.,* **148,** A74-A81 (2001)

128. S Primdahl, J Hansen, L Grahl-Madsen, P Larsen, *J. Electrochem. Soc.,* **148,** A74-A81 (2001)

129. P Vernoux, M Guillodo, J Fouletier, A Hammou., *Solid. State. Ion.,* **135,** 425-431 (2000)

130. I Jung, D Lee, S-O Lee, D Kim, J Kim, S-H Hyun, J Moon, *Ceram. Int.,* 9753-9758 (2013)

131. E Lay, G Gauthier, S Rosini, C Savaniu, J Irvine, *Solid. State. Ion.,* **173,** 1562-1566 (2008)

132. Y Ye, T He, Y Li, E Tang, T Reitz, S Jiang, *J. Electrochem. Soc.,* **155,** B811-B818 (2008)

133. M Verbreaken, T Ramos, K Agersted, Q Ma, C Savaniu, B Sudireddy, J Irvine, P Holtappels, F Tietz, *RSC Adv.,* **5,** 1168-1180 (2015)

134. D Miller, J Irvine, *J. Power Sources,* **196,** 7323-7327 (2011)

135. B Zhang, J Wang, T Zou, S Zhang, X Year, N Ding, C Liu, L Mao, Y Li, Y Wum, *J. Mater. Chem. C.,* **3,** 11406-11411. (2015)

136. J Jorgensen, B Dabrowski, S-Y Pei, D Richards, D Hinks, *Phys. Rev. B.,* **40**(4), 2187-2199 (1989)

137. F Bidrawn, G Kim, N Aramrueang, J Vohs, R Gorte, *J. Power Sources,* 195(3),720-728 (2010)

138. M Laguna-Bercero, H Monzon, A Larrea and V Orera, *J. Mater. Chem. A.,* **4,** 1446 (2016)

139. B Mace, Z Harrell, X Xu, C Chen, E Enriquez, A Chen, Q Ji, *J. Materiomics.,* **4,** 51-55 (2018)

140. T Takeda, R Kanno, Y Kawamoto, Y Takeda, O Yamamoto, *J. Electrochem. Soc.,* **147,** 1730-1733 (2000)

141. M Avdeev, M Haas, J Jorgensen, R Cava, *J. Solid. State. Chem.,* **69,** 24-34 (2002)

142. C A Hancock, J M Porras-Vazquez, P J Keenan, P R Slater, *Dalton Trans.,* **44**, 10559-10569 (2015)

143. C Greaves, P R Slater, *Physica C*, **175**, 172-178. (1991)

144. C Greaves, P R Slater, *J. Mater. Chem.,* **1**, 17-21. (1991)

145. A Maignan, M Hervieu, C Michel, B Raveau, *Physica C*, **208**, 116-120. (1993)

146. P R Slater, C Greaves, M Slaski, C M Muirhead, *Physica C,* **208**, 193- 196. (1993)

147. Y Miyazaki, H Yamane, N Ohnishi, T Kajitani, K Hiraga, Y Morii, S Funahashi, T Hirai, *Physica C*, **198**, 7-13 (1992)

148. K Kinoshita, T Yamada, *Nature,* **357**, 313-315. (1992)

149. V Caignaert, B Domenges, B Raveau, *J. Solid State Chem.,* **120**, 279-289. (1995)

150. D Pelloquin, M Hervieu, C Michel, N Nguyen, B Raveau, *J. Solid State Chem.,* **134**, 395-408. (1997)

151. J Deakin, I Trussov, A Gibbs, E Kendrick, P R Slater, *Dalton Trans,* **47**, 12901-12906 (2018)

152. B Raveau, M Hervieu, D Pelloquin, C Michel and R Retoux, *Zeitschrift Fur Anorganische Und Allgemeine Chemie,* **631**, 1831-1839. (2005)

153. Y Breard, C Michel, M Hervieu, N Nguyen, A Ducouret, V Hardy, A Maignan, B Raveau, F Boure, G Andre, *Chem. Mat.,* **16**, 2895-2905. (2004)

154. Y Breard, C Michel, M Hervieu, B. Raveau, *J. Mater. Chem.,* **10**, 1043- 1045. (2000)

155. J F Shin, L Hussey, A Orera, P. R. Slater, *Chem. Comm.,* **46**, 4613-4615. (2010)

156. J F Shin, A Orera, D C Apperley P R Slater, *J. Mater. Chem.,* **21**, 874- 879. (2011)

157. J F Shin, D C Apperley, P. R. Slater, *Chem. Mat.,* **22**, 5945-5948. (2010)

158. A D Smith, J F Shin, P R Slater, *J. Solid State Chem.,* **184**, 2972 (2011)

159. C A Hancock, P R Slater, *Dalton Trans,* 40, 5599 (2011)

160. J M Porras-Vazquez, E R Losilla, P J Keenan, C A Hancock, T F Kemp, J V Hanna, P R Slater, *Dalton Trans,* **42**, 5421 (2013)

161. J M Porras-Vazquez, T F Kemp, J V Hanna, P R Slater, *J. Mater. Chem.,* **22**, 8287 (2012)

162. J M Porras-Vazquez, P R Slater, *J. Power Sources,* **209**, 180 (2012)

163. J M Porras-Vazquez, P R Slater, *Fuel Cells,* **12**, 1056 (2012)

164. J M Porras-Vazquez, T Pike, C A Hancock, J F Marco, F J Berry, F R Slater, *J. Mater. Chem. A.,* **1**, 11834 (2013)

165. A Jarvis, F J Berry, J F Marco, P R Slater, *ECS Trans.,***91**, 1467 (2019)

166. A Jarvis, P R Slater, *Crystals,* **7(**6), 169 (2017)

167. L J Ford, P R Slater, J K Christie, P Goodard, *Phys. Chem. Chem. Phys.,* **22**, 25146-25155 (2020)

168. M Al-Mamouri ,P P Edwards, C Greaves, M Slaski, *Nature*, **369**,382 (1994)

169. O Clemens, P R Slater, *Rev. Inorg. Chem.*, **33**, 105 (2013)

170. P R Slater P.R., *J. Fluor. Chem.,* **117,** 43-45 (2002)

171. E J Moon., Y Xie, E D Laird, D J Keavney, C Y Li, S J May, *J. Am. Chem. Soc.,* **136**(6) 2224-2227 (2014)

172. Y. Ni, S. Li, S.An, X.Du L. Xue, *ACS omega,* **8**(6), 5545-5552

Chapter 2: Experimental

2.1 Synthesis routes

2.1.1 Solid-state synthesis

The conventional method of synthesis for mixed metal oxides is Solid State synthesis. A standard solid-state synthesis route uses the metal oxides/carbonates reactants to form the desired material. Such reactants should be fine-grain powders and are mixed either by agate mortar and pestle or with a mechanical ball mill. This grinding process increases the surface area of the reactants to maximise the contact between reactants. (1,2)

Another way to encourage increased contact is pelletisation, pressing together reactants increases the contact between starting reagents. Pelletisation may be a chosen step after the mixing stage.

Once starting reagents have maximised contact area, samples are placed into sample containers (Usually Al_2O_3 ceramic crucibles due to being low cost, however others may be used if any reactivity with Al_2O_3) and heated at high temperatures in a furnace. Many solid-state reaction procedures suggest an initial heating cycle at a lower temperature before an intermediate grind and reheat at the desired temperature. This is to help to prevent volatilization of components in the sample during the initial heating stage. The heating stage is required to increase the rate of diffusion between the reactants and a maximum temperature usually allows the desired oxide product to form.

Another factor that is critical in the formation of desired products is the atmosphere. A range of different atmospheres may be used depending on the conditions required during the synthesis process such as oxidizing (Air or O_2), reducing (H_2/N_2 or CO_2), or inert (N_2 or Ar) as

well as reaction under vacuum. When reactions take place under an atmosphere other than air a tube furnace is used.

2.1.2 Sol-gel synthesis

An alternative synthesis route that has more recently been used for mixed metal oxides is a family of synthesis techniques described as sol-gel synthesis. (3)

Sol-gel synthesis is the preparation of a product via the transformation of a liquid solution of precursors into a gel formation, first performed in the 19th century with the hydrolysis and condensation of metal alkoxides.

Of this family of sol-gel techniques, one technique has been widely employed to synthesise mixed metal oxides, the Pechini method. Named after the author who first published the patent, the Pechini method is different from other sol-gel techniques in that it entrap metal ions within a gel polymer network originally formed by the addition of citric acid and ethylene glycol to initiate polyesterfication and form a covalent network.

The first step of the Pechini method is the dissolution of precursors into an aqueous solution. Reactants must be soluble in water, therefore typical precursors are salts such as hydroxides, acetates, chlorides, citrates, and most commonly due to their high solubility, nitrates.

Once precursors have dissolved within the solution the addition of polyesterification reagents are added. Originally the two commonly used were citric acid and ethylene glycol however more recently other gelation agents such as EDTA (ethylenediaminetetraacetic acid), PVA (polyvinyl alcohol) as well as biopolymers such as agar, starch, cellulose, pectin, alginate, chitin, chitosan and carrageenan may be used. Once added, the solution is heated (150-200 ^{o}C) to dry and drive the esterification process.

Once dried, the sample is then heated in an oven (400 ^{o}C) to decompose the covalent network which has formed, leaving a porous structure containing metal ions. Further heat treatment at a higher temperature is used to induce the crystallization of the desired product.

The advantage of such a synthesis route is the lower temperature reaction compared to the conventional solid-state route as well as the possibility to stabilise metastable phases which again cannot be achieved via high-temperature routes. However, sol-gel synthesis routes are nominally more difficult than solid-state synthesis and can be potentially difficult to control the stoichiometry of the final product.

2.1.3 Fluorination methods

When Fluorine is used within an anion doping strategy within mixed metal oxides several fluorination methods are possible

Some desired oxyfluoride materials may be formed via high-temperature synthesis of precursor reaction of metal fluorides and oxides, as shown in the below results chapters. However, for the most part, these syntheses are unsuccessful in forming the desired product due to the high thermodynamic stability of the fluorine containing reagents compared to that of the product. An example is the synthesis of superconducting material $Sr_2CuO_3F_{2+\delta}$, a standard solid-state synthesis (a high-temperature reaction) with SrF_2, $SrCO_3$ and CuO as starting reagents, would result in the formation of $SrCuO_2$ and SrF_2 with no $Sr_2CuO_2F_{2+\delta}$ formed.

Therefore, a range of low-temperature fluorination reagents is used to fluorinate an already-formed oxide intermediate, in this case Sr_2CuO_3. Previously this would involve the use of F_2 gas at a low temperature (200 °C) to form the oxyfluoride.

Whilst F_2 and NF_3 gas were used to fluorinate precursor oxides, the process was difficult to control the level of fluorination and there are safety concerns regarding toxicity and manual handling. To overcome such issues; solid state fluorination reagents were investigated. This included NH_4F, XeF_2 and MF_2 (M = Cu and Zn), however each had challenges associated with each of these reagents (see Table 1). (4)

PVDF (and other F-containing polymers) was also investigated as a potential as a fluorination agent and was shown to be successful in preparing a range of solid-state oxyfluorides e.g. $Ca_2CuO_2F_2$ and $Sr_2TiO_3F_2$ with the main benefit of using fluorine-based polymers being the good control of the amount of fluorine incorporation through the stoichiometric amount of polymer added.

The use of Fluorine-containing polymers (mainly PVDF and PTFE) is now widely used for low-temperature (below 400 °C) fluorination of oxide systems. (5) More recently such polymers have also been used to fluorinate thin film oxide precursor with some reported successful fluorination at temperatures as low as 150 °C. (6)

In the case of chapter 7, SrF_2 is used as the method to incorporate fluorine within mixed metal oxide fluorides. SrF_2 is added to the material, ground together and heated at 950 and 1050 °C (5 $^{o}C\ min^{-1}$ heating ramp) for 12 hours respectively.

2.2 Structural characterisation

2.2.1 Crystallography

Crystal structures contain three-dimensional arrangements of the atoms in a solid. In its simplest form, a crystal has a repeating arrangement, a unit cell, which can be defined by its angles (α, β and γ) and lengths (a, b and c parameters). The study of such crystal structures is known as crystallography.

There are 7 different crystal classes; Cubic, Tetragonal, Orthorhombic, Rhombohedral, Hexagonal, Monoclinic and Triclinic. Each class has distinct relationships which can be seen in Table 2.1. Alongside these classes there are 4 types of lattice, the representation of the repetition of atoms, ions or molecules in the crystal, which are represented by a letter; primitive (P), body-centered (I) and face-centered (F) and base-centered (C). The combination of crystal classes and lattices gives rise to a total of 14 Bravais lattices (Figure 2.1). (7-9)

Table 2.1: The seven crystal systems

Crystal Systems	Axial Relationships
Cubic	$a = b = c$
	$\alpha = \beta = \gamma = 90°$
Tetragonal	$a = b \neq c$
	$\alpha = \beta = \gamma = 90°$
Orthorhombic	$a \neq b \neq c$
	$\alpha = \beta = \gamma = 90°$
Monoclinic	$a \neq b \neq c$
	$\alpha = \gamma = 90°, \beta \neq 90°$
Triclinic	$a \neq b \neq c$
	$\alpha \neq 90°, \gamma \neq 90°, \beta \neq 90°$
Hexagonal	$a = b \neq c$
	$\alpha = \beta = 120°, \gamma = 90°$
Rhombohedral	$a = b = c$
	$\alpha = \beta = \gamma \neq 90°$

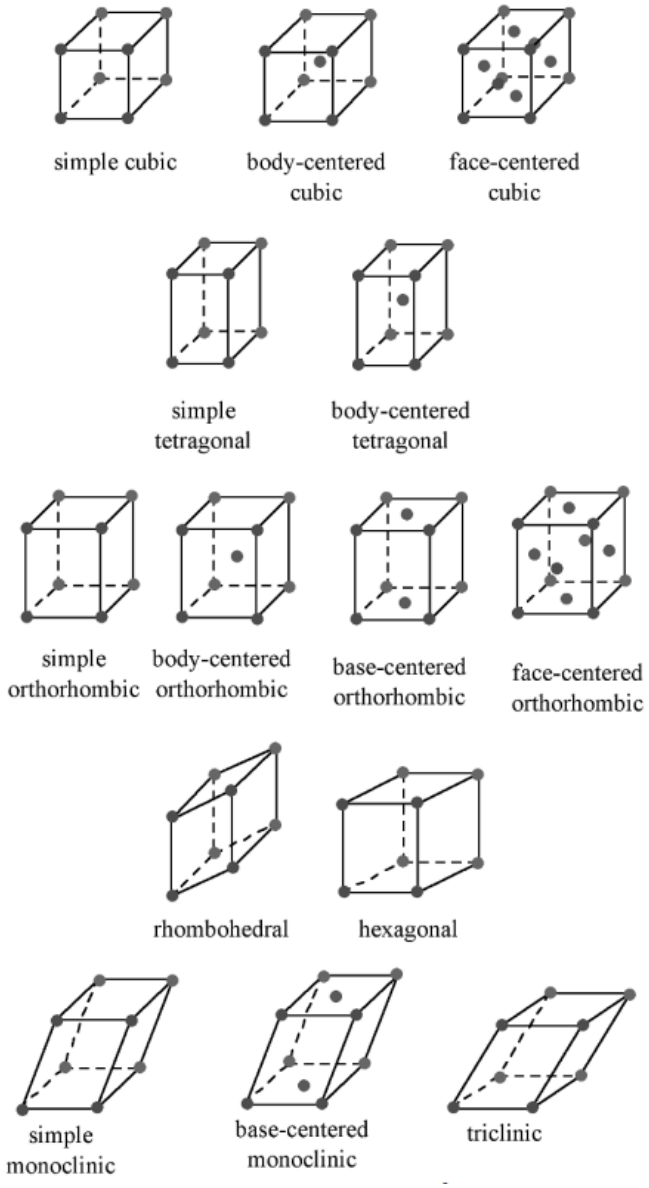

Figure 2.1: The 14 Bravais lattices (8)

The study of crystallography is important for understanding the properties of materials. For example, the ionic and electrical conductivity of a material is often related to the way the atoms are arranged in the crystal. The arrangement of the atoms can also affect the way a material conducts electrons or ions and how it responds to light. (10)

2.2.2 Powder X-ray diffraction

The crystal structure of a material can be determined by X-ray diffraction. In an X-ray diffractometer, X-rays are created when electrons accelerated from a source strike a metal target, say Cu. The accelerated electrons knock inner electrons out of the metal, as electrons in outer orbitals drop down to fill vacancies, given off characteristic X-rays. These X-rays are then ducted onto the sample. The X-rays interact with the electrons of the atoms in the crystal, and the pattern of the diffracted x-rays is recorded, see Figure 2.2. The diffraction pattern can be used to determine the spacing of the lattice planes, using Bragg's law. (7-8,11)

(Bragg's equation)

$$\text{Path Difference} = BD + DC = 2d_{hkl}\sin\theta$$

$$\text{For constructive interference } n\lambda = 2d_{hkl}\sin\theta$$

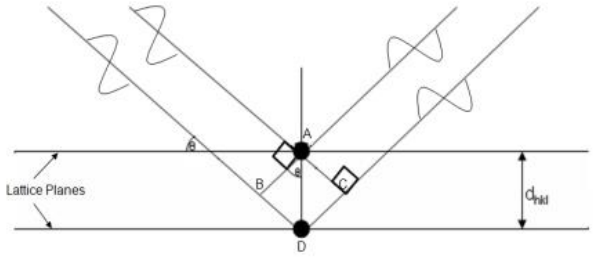

Figure 2.2 Derivation of Bragg's Law. (8)

For constructive interference the extra distance travelled by the second beam ($2d_{hkl}\sin\theta$) must equal an integer number of wavelengths.

X-ray diffraction is the process by which a beam of X-rays is scattered by a material. The scattering is a result of the interference of the waves that make up the X-ray beam. When the

waves are scattered by the atoms in the material, they produce a pattern of interference that can be used to determine the structure of the material.

X-ray diffraction is a powerful tool for understanding the structure of materials. It can be used to study the structure of crystals, proteins, and other molecules. (12-13) The diffraction pattern can provide information about the size, shape, and location of the atoms in the material.

X-ray diffraction analysis can be conducted on crystalline substances, utilizing either a single crystal or a powdered form composed of small crystallites. Given the random orientation of these crystallites, it becomes essential for both the X-ray source and the detector to be adjusted, altering the angle (known as the Bragg angle). This adjustment allows the analysis of minute differences in the crystal planes by positioning them appropriately for diffraction to take place.

For a powder sample, a monochromatic or filtered by foils beam of X-rays strikes a powder sample that is formed of crystals that are randomly arranged in various orientations. In such a sample, various lattice planes are present, with a least some of the crystals orientated at the Bragg angle, θ, to the beam and thus diffraction occurs for these crystals. The diffracted beam may be detected by a detector, which gives a series of peaks. Both peak position, height and area can be used to determine the crystalline phases which are present in a sample

Data analysis is an important part of X-ray diffraction. The data must be carefully analysed to determine the structure of the material (see below section on Rietveld analysis). This analysis is typically done by computer.

One of the advantages of Powder X-ray diffraction is that it is a non-destructive technique, which means that it can be used to study materials without damaging them. This means the same sample may be used for both structural characterisation and physical property analysis.

Powder X-Ray diffraction data were collected in order to determine lattice parameters and phase purity of samples. Data were collected on the Panalytical Empyrean diffractometer equipped with Pixcel 2D detector (Cu Kα radiation).

2.2.3 Rietveld analysis

Originally, structure determination could only be performed using by single crystal X-ray diffraction leaving many issues for scientists due to difficulty in producing single crystals of a suitable size. However, with the application of computers to conduct full pattern analysis, more complex structures may be determined. The main originator of the method, Hugo Rietveld designed this method originally to obtain structure determination using powder neutron diffraction data but this method is now the state-of-the-art method to extract structural details from powder X-ray diffraction data as well. (14-17)

In this method a starting model (that is as close as possible to the expected structure) is used to calculate initial intensity at each point. In the starting material, the following parameters are used; unit cell size, atomic position, occupancy and thermal motion of the atoms as well as non-structural parameters, such as the background, peak shape and microstructure. The model is modified using the least-square method (Equation 1) until the difference between the observed and the calculated diffraction patterns reaches a minimum. Numerical measurements of the refinement, known as the R-factors, (Equation 2-5) show how well the data matches the produced model with smaller values indicating a better fit.

(1)

$$I_{hkl} \propto |F_{hkl}|^2$$

$$F_{hkl} = \sum_{j=1}^{m} N_j F_j \exp\left[2\pi i \left(hx_j + ky_j + lz_j\right)\right]$$

(2) Least square refinement residual

$$Sy = \sum_i w_i (y_i - y_{ci})^2$$

y_i is the observed intensity at the i^{th}point

$y_{ci}$is the calculated intensity at the i^{th}point

w_i is the weighting of each data point

(3): R weighted profile

$$R_{wp} = \left[\frac{\sum_i w_i (y_i - y_{ci})^2}{\sum_i w_i (y_i)^2}\right]^{\frac{1}{2}}$$

(4) R expected profile

$$R_{exp} = \left[\frac{(N - P - C}{\sum_i w_i (y_i)^2}\right]^{\frac{1}{2}}$$

N is the number of observations

P is the number of parameters varied

(5) Goodness of fit equation

$$X^2 = \left[\frac{R_{wp}}{R_{exp}}\right]^2$$

The key parameters to look at in the in the final refinement are the R_{wp} value, the X^2 (which showed both be low) as well as the general X-ray profile for the model.

In this thesis, the GSAS-II suite of programs was used to determine unit cell parameters and structural determination. (18-19)

2.3 Thermogravimetric Analysis

Thermogravimetric analysis (TGA) is a technique used to measure weight changes in samples as a function of temperature. TGA can be used to help to determine the composition of a material, monitor reactions, or study decomposition processes. (20)

In a typical TGA experiment, a sample is heated at a constant rate while its weight is monitored. The resulting weight-versus-temperature curve can reveal important information about the sample, such as the temperature at which it begins to lose weight, the temperature at which the weight loss is complete, and the rate of weight loss.

There are many factors that can influence the outcome of a TGA experiment, including the type of sample, the heating rate, the atmosphere, and the presence of other materials. TGA is a powerful tool that can provide valuable insights into the behaviour of materials at elevated temperatures.

Within this thesis samples were analysed to determine transition metal oxidation states using thermogravimetric analysis (Netzch STA 449 F2 Jupiter Thermal Analyser). Samples were heated to 1200 °C (10 °C / min) in N_2 and held at this temperature for 30 minutes to reduce the iron and manganese oxidation states to +3, thus allowing the oxygen content and average metal oxidation to be determined.

Here is an example of the calculation of average metal oxidation for material $Ca_2MnFe_{0.95}P_{0.05}O_x$:

Molar mass (Mr) of $Ca_2MnFe_{0.95}P_{0.05}O_x$ is 189.6954 + 15.999x (x being the content of oxygen)

Upon heating to 1200 °C in N_2, iron and manganese oxidation states are reduced to +3, therefore the oxygen content of the reduced phase is known; $Ca_2MnFe_{0.95}P_{0.05}O_{5.05}$ (Mr: 270 .4924)

During the Thermogravimetric analysis the mass loss was found to be 1.57% (98.43 the original content)

Therefore:

$$15.999x = \left(\frac{270.4924}{0.9843}\right) - 189.6954$$

$$x = \frac{85.1115}{15.999}$$

$$x = 5.3198$$

Therefore, knowing that oxidation state O is -2, Ca is +2 and P is +5, The oxidation state of Mn/Fe can be inferred.

Average oxidation state of Mn/Fe is +3.28

2.4 Electrical 4-probe conductivity measurements

Electrical conductivity is a vital characteristic of any fuel cell electrode material. SOFC cathodes benefit from high electronic conductivity. Whilst there are several methods for quantifying the conductivity of materials, 4-probe DC conductivity was chosen as it is a relatively straightforward method and has previously been used to measure SOFC cathode material, both thin-film and bulk. (21-23) 4-probe DC conductivity is a beneficial technique for determining samples' conductivity with relatively low resistivities.

The measurement is carried out by attaching thin (less than 1 mm) electrode wires (either gold or platinum, depending on the temperature range of measurement) to a sintered dense bar sanded to a cuboid shape, as shown in Figure 2.3. Wires 1 and 4 are fixed around the edge of the bar whilst wires 2 and 3 are attached within the centre. A fixed current (0.10 A) is passed across the outer electrodes (1 and 4), with the difference in voltage between the inner two electrodes (2 and 3) measured. From this, it is possible to calculate the resistances, which can be used to calculate the material's conductivity. The equations involved can be seen in Equation 6.

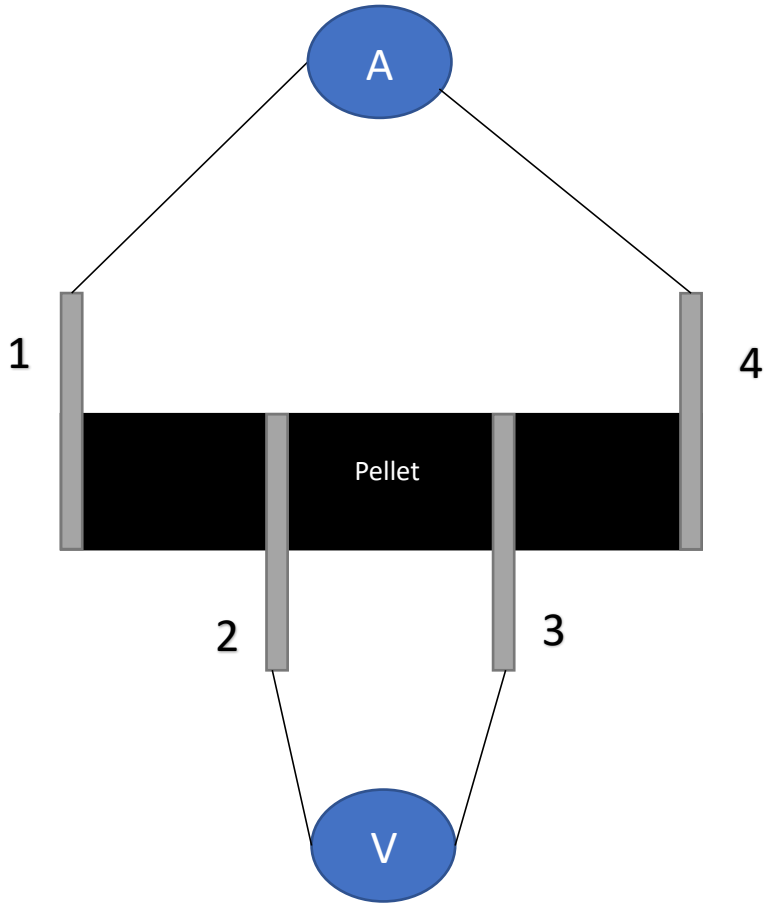

Figure 2.3 Schematic of 4-probe conductivity setup.

Equation 6. Calculation for 4-probe DC conductivity

$$\sigma = \frac{L}{A} \times \frac{I}{V}$$

Where:

σ is conductivity in S cm^{-1}

L is the distance between electrodes 2 and 3

A is the cross-sectional area of the bar; (Width and Height)

I is the current passed between electrodes 1 and 4

V is the voltage difference between electrodes 2 and 3.

Bars for conductivity measurements were prepared by ball-milling (350 rpm for 30 minutes) before compacting the material and sintering at the synthesis temperature for 12 hours. Four Pt electrodes were attached with Pt paste and the samples were heated to 950 °C for 1 hour in air to ensure good contact. Samples were then cooled to 350 °C and held at this temperature for 12 hours to ensure the maximum oxygen content. The distance between inner wires and cross-sectional area was measured by using a digital calliper.

For measuring the conductivity of materials at the desired temperature (400-800 °C), the electrode wires is attached to a measurement rig and put into a furnace where conductivity measurements are undertaken at the desired temperatures. Conductivities were then measured in air with varying temperatures (400 to 800 °C) using the four-probe dc method.

Here is an example of the calculation of 4-probe conductivity measurements:

$Sr_2MnFe_{0.95}P_{0.05}O_{6-\delta}$ at 700 °C

L is 0.645 cm

A is 0.1388 cm^2 (Diameter 1.228 × Thickness 0.113)

I is 0.10 A

V is 0.0276 V

Therefore;

$$\sigma = \frac{0.645}{0.1388} \times \frac{0.1}{0.0276}$$

$\sigma =$ 16.84 S cm^{-1}

2.5 Mössbauer spectroscopy

Mössbauer Spectroscopy is an analytical technique for determining the oxidation states and environment of iron ions or other mössbauer active species in a sample. It can be used to characterise magnetic properties, valence species and coordination polyhedron by the study of emission and absorption of nuclei gamma rays. The technique is non-destructive and may only be performed on solid samples, due to requiring a rigid crystal lattice. (24)

In this work, the iron nuclei are studied to distinguish between oxidation states through ^{57}Fe – Mössbauer spectroscopy. This specific type of spectroscopy requires a radioactive source ^{57}Co that decays to ^{57}Fe, an unstable product which emits gamma rays which are absorbed by other ^{57}Fe within iron containing samples (around 2% of iron is ^{57}Fe). (25-28)

^{57}Fe Mössbauer spectroscopy was carried out at 298 K in constant acceleration mode using approximately 25mCi Co/Rh source.

2.6 Scanning Electron Microscopy / Energy-dispersive X-ray spectroscopy

In a scanning electron microscope (SEM), a focused electron beam is raster scanned across a surface of an object, allowing the surface to be imaged with nanometer-scale resolution. The resolution of a SEM is limited by the wavelength of the electrons used to create the image, which is around 0.5 to 10 nanometers. (29)

A SEM image is created by using a scanning electron beam to interact with the surface of the sample. The electrons in the beam interact with the atoms in the sample, causing them to emit secondary electrons. These secondary electrons are then detected by an electron detector, which creates an image of the surface.

The resolution of a SEM is limited by the wavelength of the electrons used to create the image. The shorter the wavelength, the higher the resolution. However, shorter wavelength electrons are also more likely to damage the sample, so there is a trade-off between resolution and damage.

SEM can be used to image a variety of different materials, including metals, semiconductors, and insulators.

SEM images were collected on a Hitachi Tabletop Microscope TM4000Plus with EDS Oxford Instruments MICSF+ X-stream-2-attachment.

Energy-dispersive X-ray spectroscopy (EDS or EDX) is an analytical technique used for elemental analysis. EDX is a type of X-ray spectroscopy in which a beam of X-rays is directed at a sample, causing the sample to emit X-rays at specific energies (as outlined below). These emitted X-rays are then detected and analysed to identify the elemental composition of the sample. (30)

When X-rays strike a sample, they interact with the atoms in the sample, causing the electrons in the atoms to be excited to higher energy levels. When the excited electrons revert back to their original energy levels, they emit X-rays of specific energies, known as characteristic X-rays. The characteristic X-rays emitted by an element are unique to that element and can be used to identify it.

EDX instruments typically consist of an X-ray source, a sample holder, and a detector. The X-ray source is used to generate the beam of X-rays that interacts with the sample. The sample holder is used to position the sample in the beam of X-rays. The detector is used to detect the energetic X-rays emitted by the sample and to create a spectrum of these X-rays.

EDX spectra are typically analyzed using a computer program. The software will identify the characteristic X-rays emitted by the elements in the sample and quantify the amount of each element present.

EDX is a relatively quick and easy way to determine the elemental composition of a sample. It does not require the sample to be in a pure form, and it can be used on a variety of sample types. However, EDX analysis can suffer from inaccuracies particularly for low- atomic-number elements (below Carbon).

Alongside the SEM images, materials were analysed using an energy-dispersive X-ray spectroscopy to determine the elemental distribution across the sample.

2.7 Fourier-transform infrared spectroscopy

In Fourier-transform infrared spectroscopy (FTIR), a sample is exposed to infrared light and the resulting infrared absorption spectrum is recorded. The spectrum is a plot of the infrared absorption as a function of wavelength. The recorded spectrum is then analyzed using a mathematical technique called Fourier transformation to obtain information about the molecular structure of the sample. (31)

FTIR spectroscopy is therefore a tool for characterizing the molecular structure of materials. It can be used to identify functional groups in molecules, to determine the relative abundance of different isotopes of an element, and to study the vibrational and rotational states of mixed metal oxides. FTIR spectroscopy can also be used to study the structure of complex materials, such as polymers and biological samples.

The main advantage of FTIR spectroscopy over other infrared spectroscopic techniques is that it can be used to obtain information about very small quantities of material. In addition, FTIR

spectroscopy can be used to study samples that are not well-ordered, such as liquids and gases.

The interpretation of an infrared absorption spectrum requires an understanding of the molecular structure of the material being studied. The most important feature of an infrared absorption spectrum is the position of the absorption bands. The position of an absorption band is determined by the wavelength of the light that is absorbed. The wavelength of the light that is absorbed is related to the energy of the light by the equation:

$$E = hc/\lambda$$

where h is Planck's constant, c is the speed of light, and λ is the wavelength of the light.

The energy of the light is related to the vibrational and rotational states of the molecules/compound in the sample. The absorption of light by a molecule/compound can cause the molecule to transition to a higher energy state. The energy of the light that is absorbed is equal to the difference in energy between the initial and final states of the molecule/compound.

The position of the absorption bands in an infrared absorption spectrum can be used to identify the functional groups present in the molecule/compound.

The most common method for interpreting an infrared absorption spectrum is to compare the spectrum to a library of known spectra. The library of known spectra can be created by measuring the spectra of known compounds or by using theoretical calculations.

FT-IR Spectroscopy measurements were carried out to confirm the presence of functional groups such as oxyanion groups (carbonate, borate, sulphate, silicate and phosphate) and

compositions of ceramic materials. The measurements were collected on a Bruker Alpha II FTIR-Spectrometer with the platinum ATR attachment.

2.8 Dilatometry

Dilatometry is the study of the change in size or shape of a material as a result of a change in temperature. (32)

When a material is subjected to heat, its atoms begin to vibrate with increased intensity, causing them to move further apart. As a result, the material typically undergoes expansion. Conversely, cooling the material reduces the vibrational energy of its atoms, drawing the molecules closer to each other, leading to the contraction of the material.

The amount by which a material expands or contracts when heated or cooled can be defined by a coefficient of thermal expansion (TEC) which calculated by comparing with a known standard (such as metal alloy or ceramic). The coefficient of thermal expansion is a measure of how much an object expands or contracts in response to a change in temperature. Each material has a specific TEC.

The coefficient of thermal expansion also depends on the temperature at which the measurement is made. The coefficient of thermal expansion on metal oxides is usually greater at higher temperatures, commonly because the expansion can be increased by oxygen loss, and so reduction of the metal oxidation state.

Materials were studied to determine the thermal expansion coefficient and where compared to current SOFC electrolyte materials to determine the compatibility. Samples were prepared by ball milling samples for 30 minutes with small amounts of hexane than pressed into circular pellets and heated at 1100 °C in air for 12 hours. CTE was determined by a dilatometer

(Netzsch DIL 402C) from 110 to 900 ^{o}C using Al_2O_3 as a reference with heating rate of 5 ^{o}C min^{-1} in air.

2.9 References

1. M. Jensen *Angew. Chem. Int. Ed.* **41** (20), 3746-3766 (2002)

2. A. Stein, S Keller and T. E. Mallouk, *Science,* **259** (5101), 1558-1564

3. A. E. Danks, S. R. Hall and Z. Schnepp, *Mater. Horiz.,* **3,** 91-112 (2016)

4. Clemens O., Slater P.R., *Rev. Inorg. Chem.* **33** 105 (2013)

5. Slater P.R., *Journal of Fluorine Chemistry* **117** 43-45 (2002)

6. Moon E.J., Xie Y., Laird E.D., Keavney D.J., Li C.Y., May S.J. *Journal of American Chemical Society* **136**(6) 2224-2227 (2014)

7. E Moore, L Smart, *Solid State Chemistry: An Introduction,* CRC Press, 4th edition, (2012)

8. A West, *Solid State Chemistry and it's Applications*, Willy-Blackwell, 2nd edition, (2014)

9. N. W. Ashcroft, N. D Mermin, *Solid state physics,* AshcroftPublisger, 1st edition (1976)

10. M. I. Maryo, *Internatonal Tables for Crystallography Volume A: Space-group symmetry,* 2nd edition (2016)

11. K. D. M. Harris, M. Tremayne and B. M. Kariuki, *Angew. Chem. Int. Ed.* **40** (9), 1626-1651 (2002)

12. D. Ringe and G. A. Petsko, *Prog. Biophys. Mol. Biol.,* **45** (3), 197-235 (1985)

13. D. Ringe and G. A. Petsko, *Meth. Enzymol.,* **131,** 389-433 (1986)

14. H. M. Reitveld, *Acta. Crystallogr., **S21,*** A228 (1966)

15. H. M. Reitveld, *Acta. Crystallogr* **20,** 508 (1966)

16. H. M. Reitveld, *Acta. Crystallogr* **22,** 151 (1967)

17. H. M. Reitveld, *J. Appl. Crystallogr,* **2,** 65 (1969)

18. B. H. Toby, *Powder Diffr.,* **21,** 65-70 (2006)

19. B. H. Toby and R. B. Von Dreele, *J. Appl. Chem,* 46(2), 544-549 (2013)

20. A. W. Coats and J. P. Redfern, *Analyst,* **88,** 906-924 (1963)

21. J. Patakangas, Y. Ma, Y. Jing and P. Lund., *J. Power. Sources.,* **263,** 315-331 (2014)

22. A. A. Ramadan, R. D. Gould and A. Ashour, *Thin. Solid. Films.,* **239** (2), 272-275 (1994)

23. C. A. Hancock, *Anion substitution in Perovskite related materials for fuel cell applications,* [Thesis], University of Birmingham, (2012)

24. C. L. Bianchi, R. Djellabi, A. Ponti, G. S. Patience and E. Falletta., *Can. J. Chem. Eng.,* **99** (10), 2105-2114

25. F. J. Berry, C. Greaves, Ö. Helgason, J. McManus, H. M. Palmer. R. T. Williams., *J. Solid State Chem.,* **151,** 157-162 (2000)

26. F. J. Berry, M. H Loretto, M. R. Smith, *J. Solid State Chem.,* **83,** 91-99 (1989)

27. F. J. Berry, L. Liwu, C. Wang, R. Tang, S. Zhang, D. Liang., *J. Chem. Soc. Faraday. Trans. 1.,* **81** (10), 2293-2305 (1985)

28. F. J. Berry, S. Skinner, M. F. Thomas, *J. Condens. Matter. Phys.,* **10,** 215-220 (1998)

29. W. Zhou, R. Apkarian, Z. L. Wang and D. Joy, *Scanning Microsopy for Nanotechnology,* Springer, 1-40, (2007)

30. J. C. Russ, *Fundamentals of Energy Dispersive X-rat Analysis,* Elsevier (1984)

31. H. Kaur, B. Rana, D. Tomar, S. Kaur and K. C. Jena., *Modern Techniques of Spectroscopy,* Springer, 3-37 (2021)

32. H. Michael, R. Jervis, D. J. L. Brett and P. R. Shearing, *Batter. Supercaps.,* **4,** 1378-1396 (2021)

Chapter 3: Synthesis and Characterisation of Phosphate dope $(Ca/Sr)_2MnFeO_{6-\delta}$

3.1 Introduction

Perovskite structures have been overwhelmingly researched as novel electrode materials for Solid Oxide Fuel Cells and Electrolysers (SOFC's/SOE's). This is due to their high electronic and ionic conductivity. (1-4) Traditionally, doping strategies include the substitution of an A-site cation for an aliovalent of a similar size, e.g. Sr^{2+} for La^{3+}, within $La_{1-x}Sr_xMnO_{3-\delta}$ (LSM), a good mixed ionic electronic conductor. (5-9)

However, an alternative strategy has become more prominent in recent years; doping with much smaller cations, B^{3+}, C^{4+}, Si^{4+}, P^{5+} and S^{6+}, which is accommodated by oxyanion groups (Borate, Carbonate, Silicate, Phosphate, and Sulphate). (10) Previous work on superconducting perovskite demonstrated the successful incorporation of oxyanions into perovskite cuprate. (11-14) Studies showed that these materials demonstrated a great propensity to accommodate oxyanions (50% carbonate within $Sr_2CuO_2CO_3$) and, as such, resulted in the synthesis of novel materials which would not have been possible without this doping strategy. For example, low levels of $(PO_4)^{3-}$ were incorporated within $YBa_2Cu_3O_7$, resulting in the formation of a new superconducting material, $YBa_2Cu_{2.97}P_{0.03}O_{7-\delta}$, with a recorded critical temperature of 97 K. (15)

More recently, oxyanions doping strategies have been studied in more detail for their potential use in SOFC and SOE applications. (16-22) Due to the necessity of a high sintering temperature, oxyanions with a high thermal stability are required. Therefore, initial work has focused on phosphate (as well as sulphate) doping. (23) Previous work has shown that the incorporation of phosphate within $SrCoO_{3-\delta}$ stabilises a cubic perovskite structure, which allows for a substantial increase in conductivity compared to the undoped variant with a

hexagonal structure. (24) Phosphate doping has also been extended to $CaMnO_{3-\delta}$ and the doping strategy was shown to improve conductivity whilst adopting the cubic phase. This is due to the creation of oxygen vacancies associated with the substitution of phosphorous onto the B-site with tetrahedral coordination, compared to the manganese octahedral coordination, thus leading to the reduction of Mn^{4+} to give mixed valence Mn^{3+}/Mn^{4+}. (25)

This work was also carried out on $Ba_{1-x}Sr_xCo_{0.8}Fe_{0.2}O_{3-\delta}$ (BSCF) and $La_{1-y}Sr_yMnO_{3-\delta,}$ (LSM), adopting a cubic cell on incorporation of phosphate. (26-27) It was found with both perovskite structures that phosphate doped materials enhanced the conductivity and electrode performance. In addition, phosphate doping was shown to help improve the long-term stability of the cubic form of BSCF at intermediate temperatures with a negligible change in conductivity.

Herein, this chapter examines the use of phosphate doping of the mixed perovskite Mn/Fe system, $Sr_{2-x}Ca_xMnFeO_{6-\delta,}$ to design a novel low-cost cathode material. (28-30) Previous work by Smith et al. showed a silicon doping strategy was successful in synthesising $Ca_2MnFe_{1-x}Si_xO_{6-\delta}$ and $Sr_2MnFe_{1-x}Si_xO_{6-\delta}$ with the formation of a single-phase cubic perovskite structure. (31) For both systems, the conductivities improved with low levels of Si doping (≤ 0.1), with a decrease at higher silicate levels. The work shows that P can also be successfully incorporated into these $(Sr/Ca)_2MnFeO_{6-\delta}$ systems and show that conductivities are higher than the previously reported silicon doped variant.

3.2 Experimental

High purity $CaCO_{3,}$ $SrCO_{3,}$ $MnO_{2,}$ $Fe_2O_{3,}$ and $(NH_4)_3PO_4$ were used to prepare $Ca_{2-x}Sr_xMnFe_{1-x}P_xO_{6-\delta}$ (y = 0 and 2) materials. Stoichiometric calculated mixtures of the powders were intimately ground and initially heated to 1000 °C (10 °C min^{-1}) for 12 hours. Samples were

then reground and heated to 1250 °C (y=2), 1275 °C (y=1), and 1300 (y=0) for 24 hours with an intermediate regrind. To ensure maximum oxygen content, the resulting samples were held at 350 °C for 12 hours in air.

In order to study the effect of phosphate on the stability at lower temperatures, $Ca_{2-x}Sr_xMnFe_{1-x}P_xO_{6-\delta}$ were annealed at 1050 ^oC for 12 hours in air.

Powder X-Ray diffraction data was collected in order to determine lattice parameters and phase purity of samples. Data were collected on the Panalytical Empyrean diffractometer equipped with Pixcel 2D detector (Cu Kα radiation). The GSAS-II suite of programs was used to determine unit cell parameters. (32)

Samples were analysed to determine transition metal oxidation states using thermogravimetric analysis (Netzch STA 449 F2 Jupiter Thermal Analyser). Samples were heated to 1200 °C (10 °C / min) in N_2 and held at this temperature for 30 minutes to reduce the iron and manganese oxidation states to +3, thus allowing the oxygen content and average metal oxidation to be determined.

Pellets for conductivity measurements were prepared by ball-milling (350 rpm for 30 minutes) before compacting the material and sintering at the synthesis temperature for 12 hours. Four Pt electrodes were attached with Pt paste and the samples were heated to 950 °C for 1 hour in air to ensure good contact. Samples were then cooled to 350 °C and held at this temperature for 12 hours to ensure the maximum oxygen content. Conductivities were then measured in air with varying temperatures (400 to 800 °C) using the four-probe dc method.

SEM images were collected on a Hitachi Tabletop Microscope TM4000Plus with EDS Oxford Instruments MICSF+ X-stream-2-attachment. The materials were analysed using an energy-

dispersive X-ray spectroscopy to determine the elemental distribution of the phosphate across the sample.

3.3 Results and Discussion

3.3.1 Structural Characterisation

3.3.1.1 $Ca_2MnFe_{1-x}P_xO_{6-\delta}$

Powder X-ray diffraction shows the formation of a single-phase cubic perovskite phase (space group of *P m -3 m)* for $Ca_2MnFe_{1-x}P_xO_{6-\delta,}$ ($0 \leq x \leq 0.20$). The material x = 0.20 shows a small impurity (unable to assign but believed to be $Ca_3(PO_4)_2$ or hydroxyapatite), suggesting that the phosphate doping limit had been exceeded, Figure 3.1. Prior studies by Smith et al. also showed that higher values of silicon doping; above x = 0.15 resulted in a decrease in conductivity, and therefore, the investigation of higher phosphate contents was not attempted.

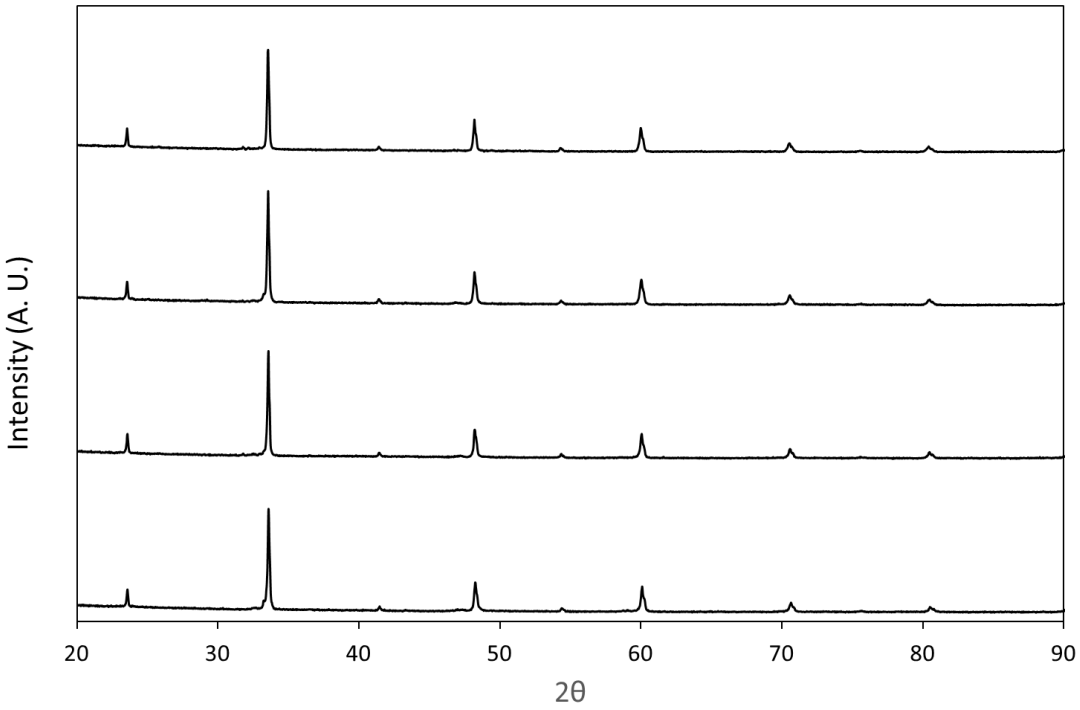

Figure 3.1. Powder X-ray diffraction from top to bottom: $Ca_2MnFe_{0.80}P_{0.20}O_{6-\delta}$, $Ca_2MnFe_{0.85}P_{0.15}O_{6-\delta}$, $Ca_2MnFe_{0.85}P_{0.15}O_{6-\delta}$, and $Ca_2MnFe_{0.80}P_{0.20}O_{6-\delta}$ showing the formation of single-phase perovskite samples.

Thermogravimetric analysis was performed on the materials to determine the mass loss in N_2, from which the average B-site oxidation state could be determined. The results of these analyses are shown in Table 3.1, indicating the oxygen content is equal to the previously reported silicon doping, with an increase in overall oxygen content on phosphate doping.

Table 3.1. Oxygen content and average B-site metal oxidation state for $Ca_2MnFe_{1-x}P_xO_{6-\delta}$

x	% Mass Loss	δ Value	Average B-site Metal Oxidation State
0.05	1.57	0.68	3.28
0.10	1.80	0.59	3.33
0.15	1.65	0.57	3.30
0.20	1.05	0.62	3.20

A structural model with space group *P m -3 m* was refined using the GSAS-II suite of programs using the experimental powder X-ray diffraction data. As with $Ca_{2-x}Sr_xMnFe_{1-x}Si_xO_{6-\delta}$ materials, the manganese, iron, and central atom of the oxyanion (phosphorus) were fitted to the B-site with the theoretical stoichiometric amounts. The calcium atom was placed on the A-site with fractional occupancies set at 1.0. The oxygen occupancy was set to the value calculated from the TGA data discussed above. The unit cell parameters from the refinements are shown in Table 3.2.

Table 3.2. Cell parameters and goodness of fit values for $Ca_2MnFe_{1-x}P_xO_{6-\delta}$

x	a (Å)	$_wRp$	Rp	χ^2
0.05	3.7678(7)	4.661	2.23	2.09
0.1	3.7712(8)	4.138	2.24	1.85
0.15	3.7719(9)	3.367	2.27	1.48
0.2	3.7738(9)	3.296	2.38	1.38

3.3.1.2 $Sr_2MnFe_{1-x}P_xO_{6-\delta}$

Powder X-ray diffraction collected on $Sr_2MnFe_{1-x}P_xO_{6\,\delta}$ materials for x = 0.05, 0.10, 0.15, and 0.20 indicated that a cubic perovskite phase was also obtained (Figure 3.2). However, with increased phosphate content, a small $Sr_3(PO_4)_2$ impurity appears, suggesting the phosphate solubility limit was exceeded for x>0.05.

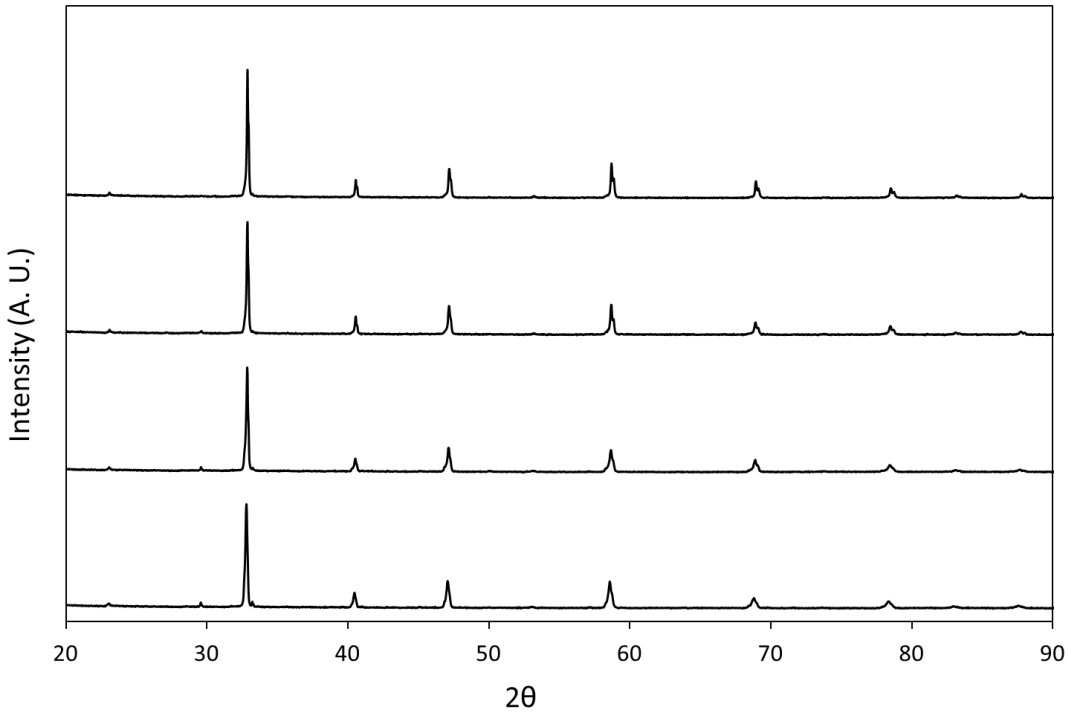

Figure 3.2. Powder X-ray diffraction from top to bottom: (a) $Sr_2MnFe_{0.95}P_{0.05}O_{6-\delta,}$ (b) $Sr_2MnFe_{0.90}P_{0.10}O_{6-\delta}$, (c) $Sr_2MnFe_{0.85}P_{0.15}O_{6-\delta}$, (d) $Sr_2MnFe_{0.80}P_{0.20}O_{6-\delta}$, showing formation of cubic perovskites. Impurity peaks, associated with $Sr_3(PO_4)_2$ can be seen increasing with phosphate doping at around 29^o and 32^o.

Thermogravimetric analysis was undertaken to measure the mass loss of the material under N_2, and so calculate the oxygen content and the average Mn/Fe oxidation states for the $Sr_2MnFe_{1-x}P_xO_{6-\delta}$ series, Table 3.3.

Table 3.3. Oxygen content and B-site Metal oxidation state for $Sr_2MnFe_{1-x}P_xO_{6-\delta}$

x	% Mass Loss	δ Value	Average B-site Metal Oxidation State
0.00	2.22	0.48	3.52
0.05	1.55	0.59	3.37
0.10	1.33	0.59	3.33
0.15	1.20	0.57	3.30
0.20	0.38	0.71	3.10

On increased doping with phosphate, an increase in oxygen vacancies is observed, along with a reduction in average Mn/Fe oxidation state. The Mn/Fe site oxidation state was shown to be lower than reported previously for Si doped materials.[32]

Mössbauer spectroscopy data for ^{57}Fe were obtained for samples with x=0 and x=0.05 to further investigate the iron environment. The observed chemical isomer shifts, $\delta \approx$ -0.23, 0.22/0.23, and 0.31/0.36 mm s^{-1} for Fe and $Fe_{0.95}P_{0.05}$, are indicative of the oxidation states Fe^{5+}, Fe^{4+}, and Fe^{3+}, respectively, as shown in Figure 3.3 and Table 3.4. These measurements verified an increase in the Fe^{3+} concentration upon doping with phosphate, a finding that is consistent with the thermogravimetric analysis (TGA) results.

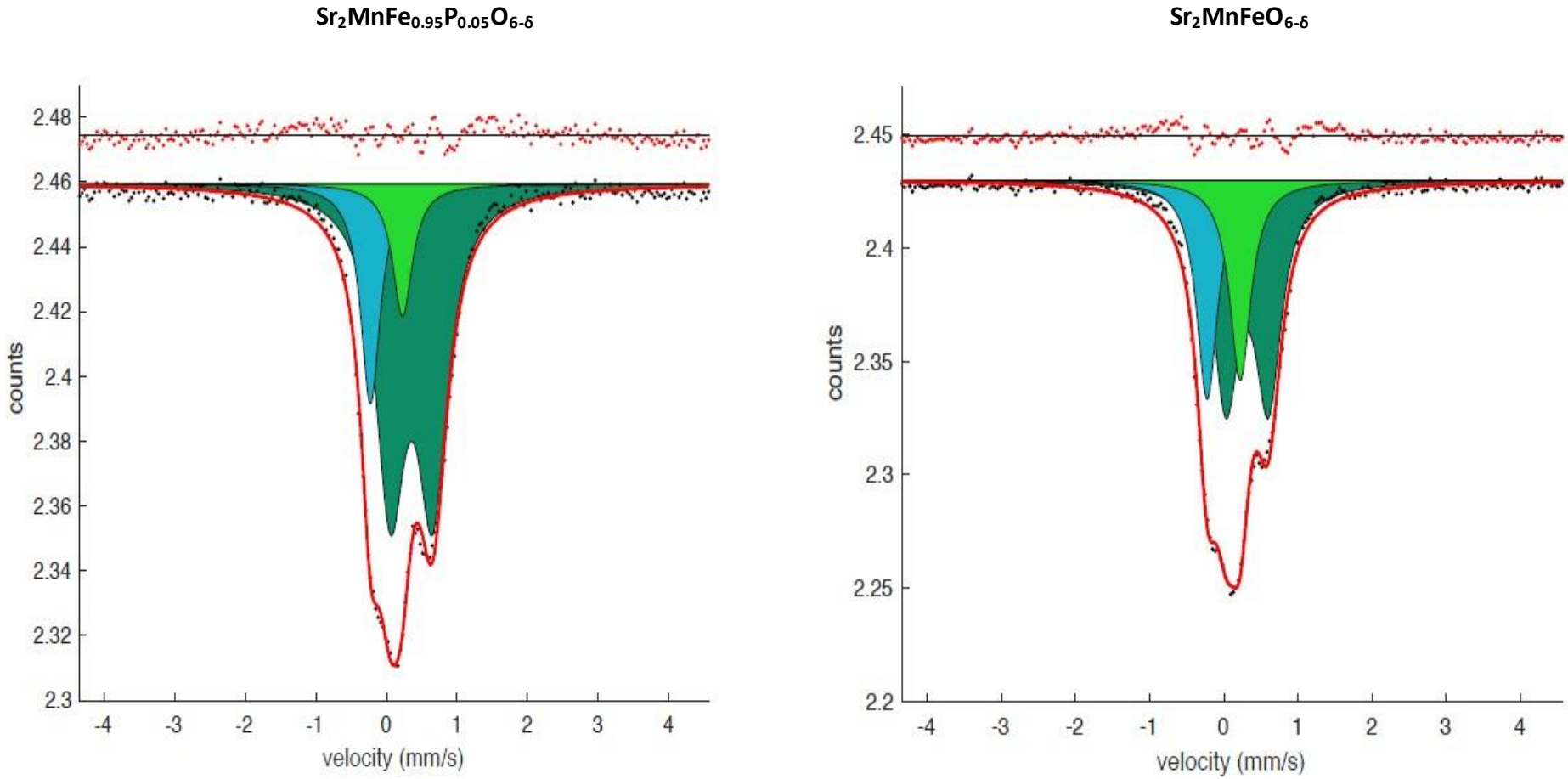

Figure 3.3. ^{57}Fe Mössbauer spectra for $Sr_2MnFe_{0.95}P_{0.05}O_{6-\delta}$ and $Sr_2MnFeO_{6-\delta}$ at 298 K

TABLE 3.4 ^{57}Fe Mössbauer Spectroscopy data for $Sr_2MnFeO_{6-\delta}$ and $Sr_2MnFe_{0.95}P_{0.05}O_{6-\delta}$

Compound	**Assignment**	**δ ± 0.02 (mms^{-1})**	**Δ ± 0.08 (mms^{-1})**	**Area ± 5% (%)**
$Sr_2MnFeO_{6-\delta}$	Fe^{3+}	0.31	0.57	55
	Fe^{4+}	0.22	---	23
	Fe^{5+}	-0.23	---	21
$Sr_2MnFe_{0.95}P_{0.05}O_{6-\delta}$	Fe^{3+}	0.36	0.60	72
	Fe^{4+}	0.23	---	11
	Fe^{5+}	-0.23	---	17

Rietveld refinement was performed using the GSAS-II suite of programs based on the space group *P m -3 m* perovskite model using the collected powder X-ray diffraction data for the phosphate doped phases. The unit cell parameters from the refinements are shown in Table 3.5.

TABLE 3.5. Cell parameters and goodness of fit values for $Sr_2MnFe_{1-x}P_xO_{6-\delta}$

X	**a (Å)**	**wRp**	**Rp**	**χ^2**
0.00	3.8452(7)	3.44	2.55	2.13
0.05	3.8490(3)	3.13	1.51	2.06
0.10	3.8510(8)	4.08	1.52	2.69
0.15	3.8541(3)	3.27	1.55	2.11
0.20	3.8573(1)	3.17	1.51	2.10

The lattice parameters were found to show a small increase with incorporation of phosphate. This observed increase in volume may be attributed to the increase in larger Fe^{3+}/Mn^{3+} ions upon doping with phosphate (as confirmed by ^{57}Fe Mössbauer Spectroscopy), which outweighs any decrease expected from the incorporation of the smaller P dopant. However, impurities are present in most of these samples, therefore it is difficult to give a clear explanation.

The elemental distribution of phosphorus across the samples was analysed using SEM-EDX. The $Sr_2MnFe_{0.95}P_{0.05}O_{5.41}$ shows a uniform distribution of phosphorous (thus phosphate) within the material, whereas $Sr_2MnFe_{0.80}P_{0.20}O_{5.29}$ showed regions of rich deposits of phosphorus within the material, emphasising that an impurity phase is present within higher phosphate doped systems, Figure 3.4.

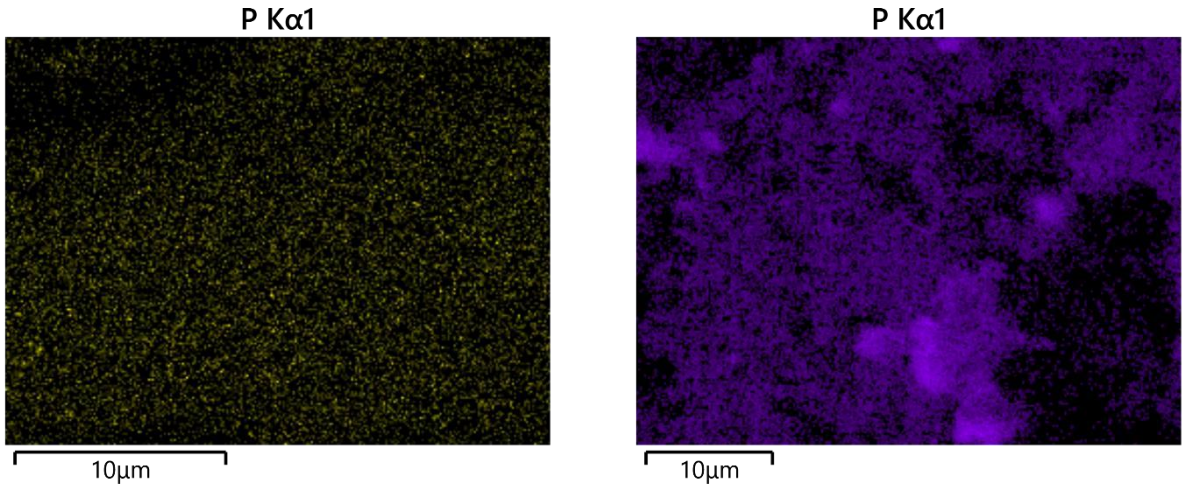

Figure 3.4. Energy-dispersive X-ray spectroscopy imaging of P (Kα1) content (left) $Sr_2MnFe_{0.95}P_{0.05}O_{5.41}$ and (right) $Sr_2MnFe_{0.80}P_{0.20}O_{5.29}$

3.3.2 Conductivity measurements

3.3.2.1 $Ca_2MnFe_{1-x}P_xO_{6-\delta}$

Conductivity measurements of the phosphate doped materials in air are shown in Figure 3.5.

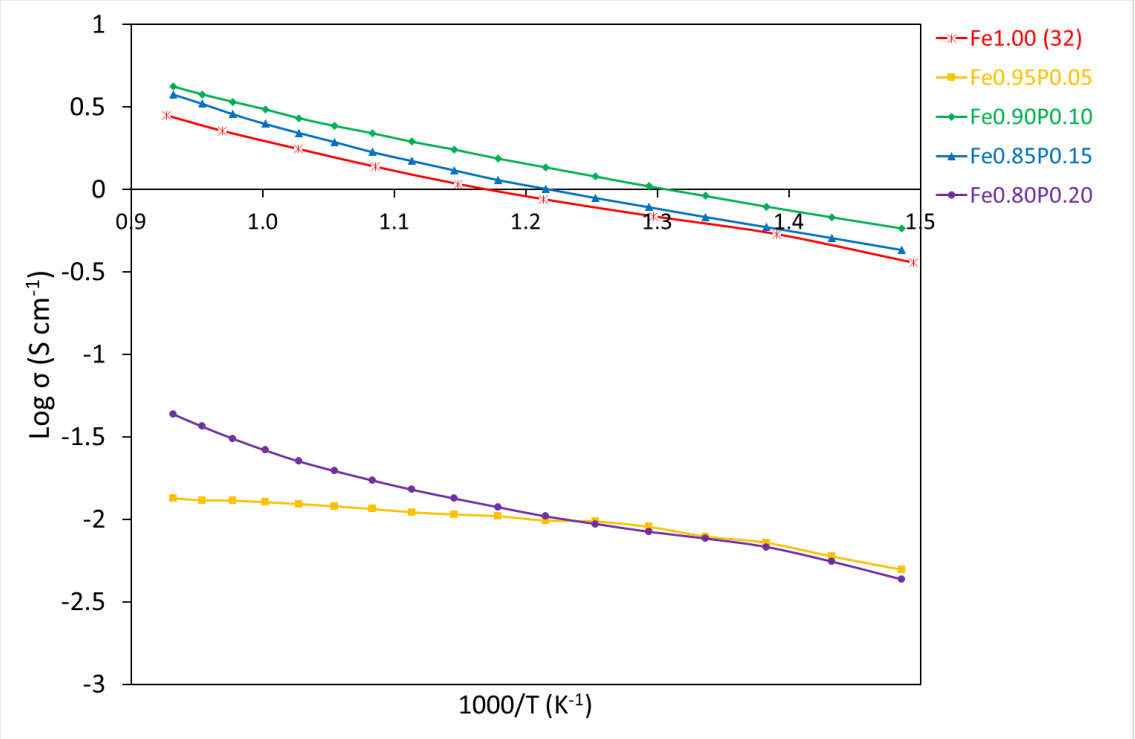

Figure 3.5. Plot of log σ versus 1000/T for $Ca_2MnFe_{1-x}P_xO_{6-\delta}$

The data show that at low phosphate doping (x=0.05), there is unusual trend, whereby x = 0.05 is lower than the undoped by Smith et al.[32] However, a significant increase in the conductivity was observed for x=0.1, 0.15, after which the conductivity decreases for the highest phosphate content (x=0.2) with the lowest conductivity being observed for this $Ca_2MnFe_{0.8}P_{0.2}O_{6-\delta}$ sample. The reduction in conductivity upon the higher dopant levels is either due to the phosphate disturbing the Mn/Fe-site/O network, and/or the presence of insulating impurities.

The initial increase in conductivity upon doping with an oxyanion is also observed with $Ca_2MnFe_{1-x}Si_xO_{6-\delta}$. We hypothesise that the increase in conductivity is caused by the disappearance of local oxygen vacancy ordering upon oxyanion doping.

3.3.2.2 $Sr_2MnFe_{1-x}P_xO_{6-\delta}$

Conductivity measurements of the phosphate doped materials in air are shown in Figure 3.6.

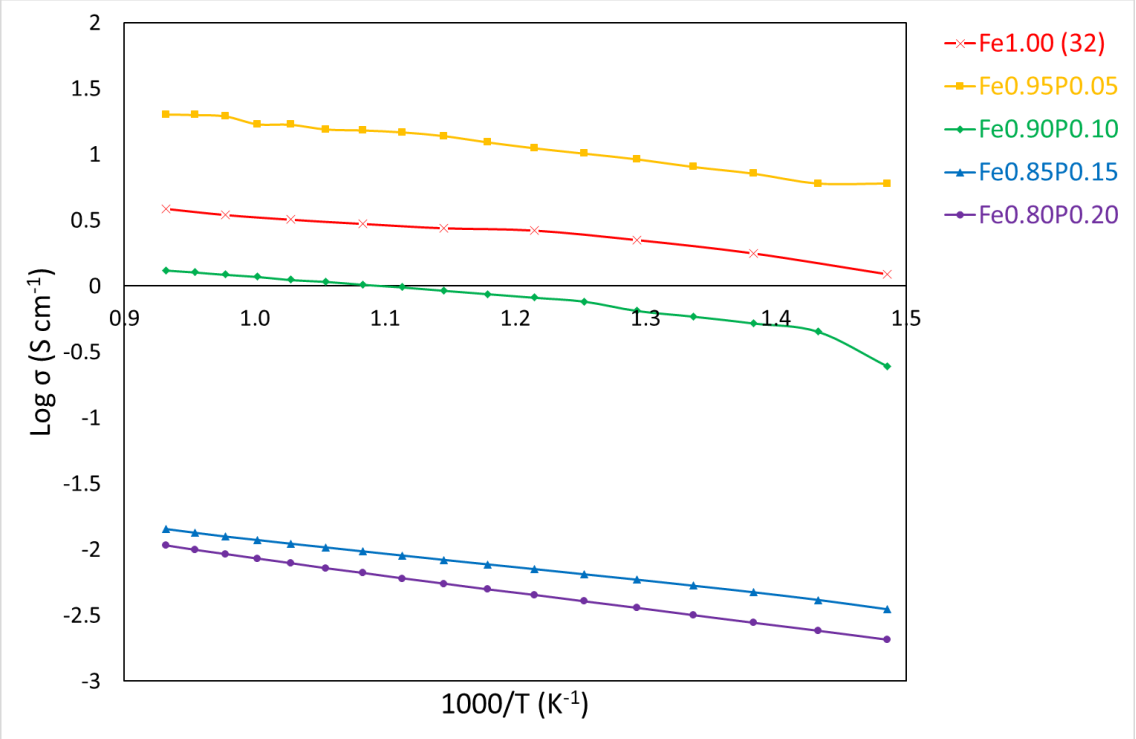

Figure 3.6. Plot of log σ versus 1000/T for $Sr_2MnFe_{1-x}P_xO_{6-\delta}$

The results highlight that the incorporation of phosphate at low levels (x = 0.05) improves the conductivity significantly before it subsequently reduces at higher phosphate contents. This reduction is attributed to presence of $Sr_3(PO_4)_2$ impurities as the solubility limit is exceeded. Overall, the conductivities of the $Sr_2MnFe_{0.95}P_{0.05}O_{5.41}$were higher than the undoped and silicate perovskite structure reported by Smith et al, Table 3.6 (32).

Table 3.6. Total conductivity data for $Sr_2MnFe_{1-x}(P,Si)_xO_{6-\delta}$ in air at 700 ^oC.

Compound	**Conductivity (S cm^{-1})**	**Ref**
$Sr_2MnFeO_{6-\delta}$	3.19	(32)
$Sr_2MnFe_{0.90}Si_{0.10}O_{6-\delta}$	10.26	(32)
$Sr_2MnFe_{0.95}P_{0.05}O_{6-\delta}$	16.84	This Work

Whilst the electronic conductivity values are generally lower than other SOFC cathode candidates, doping with low levels of other transition metals, e.g Co, may lead to further enhancement. In the current series, conductivity values are inferior to the standard SOFC cathode materials and therefore it was decided to not complete any other conductivity measurements such as ASR (Area-specfic resistance) tests.

3.4 Conclusions

In this work we have shown that phosphate can be incorporated into $(Ca/Sr)_2MnFeO_{6-\delta}$ resulting in the synthesis of a range of new cubic perovskite phases. Thermogravimetric analysis was used to calculate the oxidation states of the B-site metals and found that the materials had average Mn/Fe oxidation state in the range 3.10 to 3.47, lower than previously reported for silicon doping. Mössbauer Spectroscopy studies indicated that the amount of Fe^{3+} increased on phosphate doping, in agreement with the TGA data.

Conductivity measurements showed there was a general improvement for $(Ca/Sr)_2MnFeO_6\delta$ materials on low level of phosphate incorporation, with a decrease at higher phosphate levels attributed to the presence of impurities as the P solubility limit was exceeded. The conductivities are superior to that of silicon doping and so have potential for Solid Oxide Fuel Cell / Electrolysers applications, as well as potential interest as AFC catalysts. (33) However,

conductivity values are still inferior to standard SOFC cathode materials, and the 100 S cm^{-1} target, and therefore any further work should look at the effect of doping with low levels of other transition metals, e.g Co, which may lead to further enhancements closer to the required value.

As mixed-electron ion conducting materials, the Sr series may also be of interest of these materials as oxygen separation membranes. (34)

3.5 References

1. A. J. Jacobson, *Chem. Mat.,* **22,** 660-674 (2010)
2. C. Sun, R. Hui and J. Roller, *J. Solid. Stat. Electrochem.*, **22** 2329-2338 (2018)
3. N. Mahato, A. Banerjee, A Gupta, S Ormar and K Balani, *Prog. Mater. Sci.,* **72,** 141-337 (2015)
4. A. Orera and P. R. Slater, *Chem. Mat.,* **22**, 675-690 (2010)
5. J. B. Goodenough, *Phys. Rev.,* **100**(2) 564-573 (1955)
6. O. Chmaissem, B Dabrowki, S Kolesnik, J Maris, J.D. Jorgensen, S. Short, *Phys. Rev.,* **67**(9) 13 (2003)
7. G Corbel, S Mestiri, P. Lacorre, *Solid. State. Sci.,* **7**(10), 1216-1224 (2005)
8. L Suescun, O Chmaissem, J Mais, B Dabrowski, J Jorgensen, *J. Solid. State. Chem.,* **180**(5) 1698-1707 (2007)
9. P. S. Casey, D. Barker, M. A. Hayward, *J. Solid. State. Chem.,* **179**(5) 1375-1382 (2006)

10. C. A. Hancock, J. M Porras-Vazquez, P. J. Keenan and P. R. Slater *Dalton Trans.,* **44**, 10559-10569 (2015).

11. A. Maignan, D. Pelloquin, S. Malo, C. Michel, M. Hervieu and B. Raveau, *Physica C,* **249**(3) 220-233 (1995)

12. C. Greaves and P.R. Slater, *Physica C,* **175**(1), 172-178 (1991)

13. C. Greaves and P.R. Slater, *J. Mater. Chem.,* **1**, 17-21

14. M. A. Uribe Laverde, D.A. Landlnez Téllez and J. Roa-Rojas, *Mod. Phys. Lett. B.* **23**(6) 807-813 (2009)

15. P. R. Slater, C. Greaves, M. Slaski and C. M. Muirhead, *Physica C,* **208**(1-2) 193-196 (1993)

16. A. Jarvis, F. J. Berry, J. F. Marco and P. R. Slater. *ECS Trans,* **91**(1), 1467-1476 (2019)

17. J. Deakin, I. Trussov, A. Gibbs, E. Kendrick and P. R. Slater, *Dalton. Trans.,* **47**(37) 12901-12906 (2018)

18. A. Jarvis and P.R. Slater, *Crystals,* **7**(6) 169

19. J. M. Porras-Vazquez, R. I. Smith and P. R. Slater, *J. Solid. State. Chem.,* **213,** 132-137 (2014)

20. J. M. Porras-Vazquez, T. Pike, C. A. Hancock, J. F. Marco, F. J. Berry and P. R. Slater, *J. Mat. Chem. A.,* **1**(38) 11834-11841 (2013)

21. J. M Porras-Vazquez, E. R. Losilla, P. J. Keenan, C. A. Hancock, T. F. Kemp, J.V Hanna and P. R. Slater, *Dalton Trans.,* **42**(15) 5421-5429 (2013)

22. C. A. Hancock and P.R Slater, *Dalton Trans.,* **40**(20) 5599-5603 (2011)

23. J. F Shin, K. Joubel, D. C. Apperley and P. R. Slater *Dalton Trans.,* **41**(1), 261-266 (2012)

24. C. A. Hancock, R. C. T. Slade, J. R. Varcoe and P. R. Slater, *J. Solid. State. Chem.,* **184**(11)2972-2977, (2011)

25. J. M Porras-Vazquez, T.F. Kemp, J. V. Hanna and P. R. Slater *J. Mat. Chem.,* **22**(17) 8287-8293

26. J. M Porras-Vazquez and P. R. Slater *J. Power. Sources.,* **209**, 180-183 (2012)

27. J. M Porras-Vazquez and P. R. Slater, *Fuel. Cells.,* **12**(6) 1056-1063 (2012)

28. R. V Coates and J. W. McMillan, *J. Appl. Chem,* **14***,* 346*,* (1964)

29. F. Ramezanipour, J. E. Greedan, L. M. D. Cranswick, V. O. Garlea, R. L. Donaberger and J. Siewenie, *J. Am. Chem. Soc.,* **134** 3215-3227 (2012)

30. Y Nakahara, S. Kato, M. Sugai, Y. Ohshima and K. Makino, *Mater Lett.,* **30,** 163-167 (1997)

31. A. D. Smith, M. S. James and P. R. Slater, *ECS Trans,* **91**(1), 1425-1436 (2019)

32. B. H. Toby, R. B. Von Dreele, *J. Appl. Chem,* **46**(2), 544-549 (2013)

33. L. d. Santos-Gómez, J. M. Porras- Vazquez, E. R. Losilla, D. Marrero-Lopez, P. R. Slater, *J. Alloys Compd.,* **835,** 155437 (2020)

34. V.V Kharton, A.A. Yaremchenko, A.V. Kovalevsky, A.P. Viskup, E.N. Naumovich, P.F. Kerko, *J. Membr.Sci.,* **163**(2), 307-317 (1999)

Chapter 4: Synthesis and characterisation of Borate doped (Ba/Sr)$FeO_{3-\delta}$

4.1 Introduction

Research into solid oxide fuel cells and electrolysers (SOFC and SOE) has focused significantly on the development of perovskite systems (ABO_3) which have mixed ionic-electronic conduction for applications as electrode materials. Traditionally, the optimisation of the properties of these materials has focused on doping on the A and/or B cation site with ions of similar size, e.g $La_{1-x}Sr_xMnO_{3-\delta}$, $La_{1-x}Sr_xCo_{1-y}Fe_yO_{3-\delta}$, and $Ba_{1-x}Sr_xCo_{1-y}Fe_yO_{3-\delta}$. (1-5) The perovskite structure is, however, far more flexible towards doping, and has been shown that oxyanions such as phosphate, sulphate, silicate, borate, and carbonate, can be incorporated into perovskite structure. In this doping strategy, the central "cation" occupies the B cation site, the oxygen from the oxyanion group occupying either 3 (carbonate and borate) or 4 (phosphate, silicate and sulphate) of the 6 available positions around the site, with appropriate displacement to achieve the trigonal planar/ tetrahedral coordination of the oxyanion. (6-9)

Barium ferrite ($BaFeO_{3-\delta}$) has been shown to give rise to proton conductivity via incorporation of water molecules into the anion vacancies. Clemens et al showed that barium ferrite had two different hydrated phases dependent on temperature, with one phase showing bulk proton conductivity of around a 10^{-6} to 10^{-7} S cm^{-1} in ambient temperatures. (10-13) Barium ferrite has also been observed to be a highly complex vacancy-ordered perovskite leading to modifications from a cubic perovskite to monoclinic (Space group $P2_1/c$) which influences the materials proton conductivity.

A possible way to optimise $BaFeO_{3-\delta}$ for proton and electronic conductivity is to substitute on both A and B site cations. Anion strategies have been successfully employed via incorporation of oxyanions (BO_3^{3-}, SO_4^{2-}, SiO_4^{4-}) as anion dopants within $SrFeO_{3-\delta}$, transforming the cell from tetragonal to cubic. By changing the cell structure, oxyanion doping has been shown to improve the long-term stability of the disordered structure within higher temperatures, 500-800 °C, and the operating temperatures of SOFC's. (14) Sulphate and Boron doping demonstrated improved stability whilst maintaining comparable electronic conductivity of the original perovskite.

Similarly, the combination of Ba^{2+} and Sr^{2+} as a mixed system $Ba_{1-x}Sr_xFeO_{3-\delta}$ has also been observed with the perovskite-type structure. Varying the Ba^{2+}/Sr^{2+} ratio leads to structural changes from Monoclinic/Hexagonal -> Trigonal -> Cubic -> Tetragonal as the x axis increases.

Herein, this work demonstrates the successful incorporation of borate into $Ba_{1-x}Sr_xFeO_{3-\delta}$ (x = 0.10 and 0.50) and characterises the effect on the structure and conductivity with a view to possible utilization as a cathode material in a ceramic fuel cell (H^+ or O^{2-} conducting). The incorporation of low levels of borate was sufficient to cause a change in crystallography to form cubic perovskite structure.

4.2 Experimental

High purity $SrCO_3$, $BaCO_3$, Fe_2O_3 and H_3BO_3 were used to prepare a range of $Ba_{1-x}Sr_xFe_{1-y}B_yO_{3-\delta}$. These starting materials were ground together in correct stoichiometric ratios and heated at 900 °C for 12 hours and then 1025 °C for 12 hours.

Powder X-ray diffraction experiments collected on a Panalytical Empyrean diffractometer (Cu Kα radiation) were used to determine phase purity and the GSAS II suite of programs were used for preliminary structure refinements of these systems. (15)

^{57}Fe Mössbauer spectroscopy were recorded at 298 K in constant acceleration mode using an approximately 25mCi Co/Rh source. The isomer shifts were referred to the centroid of the spectrum of metallic iron at room temperature.

Samples heated in air were analysed using thermogravimetric analysis (Netzch STA 449 F1 Jupiter Thermal Analyser with mass spectrometry attachment). Samples were heated to 1000 °C in N_2 (10 °C min^{-1}).

Pellets for conductivity measurements were prepared by ball milling samples for 30 minutes and adding a small amount of hexane before pressing and sintering at 1025 °C in air for 12 hours, Four Pt electrodes were attached with Pt paste and the samples were heated at 900 °C for 1 hour in air and cooled to 350 °C and held at 12 hours for ensuring maximum oxygen content. Conductivities were measured using the four probe DC method.

4.3 Results and discussion

4.3.1 Structural Characterisation

4.3.1.1 $Ba_{0.90}Sr_{0.10}Fe_{1-x}B_xO_{3-\delta}$

The X-ray diffraction analysis showed that without borate doping the $Ba_{1-x}Sr_xFeO_{3-\delta}$ forms a variety of distorted perovskites in line with prior results. This is illustrated in Figure 4.1 which shows the x=0.10 being a mixed cubic phase.

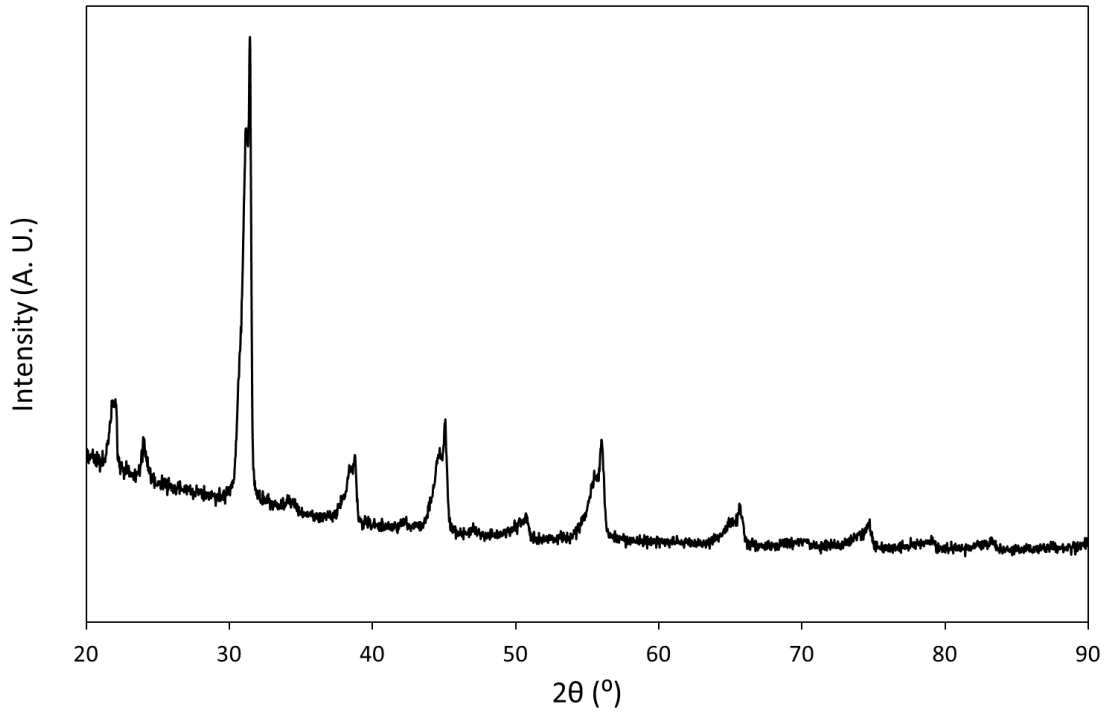

Figure 4.1. Powder X-ray diffraction patterns of $Ba_{0.90}Sr_{0.10}FeO_{3-\delta}$

Powder X-ray diffraction shows the formation of a single-phase cubic perovskite phase with a space group of *P m -3 m* for $Ba_{0.90}Sr_{0.10}Fe_{1-x}B_xO_{3-\delta}$ ($0.05 \leq x \leq 0.15$), Figure 4.2. The materials with higher borate doping $x > 0.15$ shows impurities suggesting that the borate limit has been

exceeded. Previous studies of oxyanion doped perovskites above x = 0.15/0.20 results in decreased conductivity and therefore the investigation of higher borate contents was not attempted.

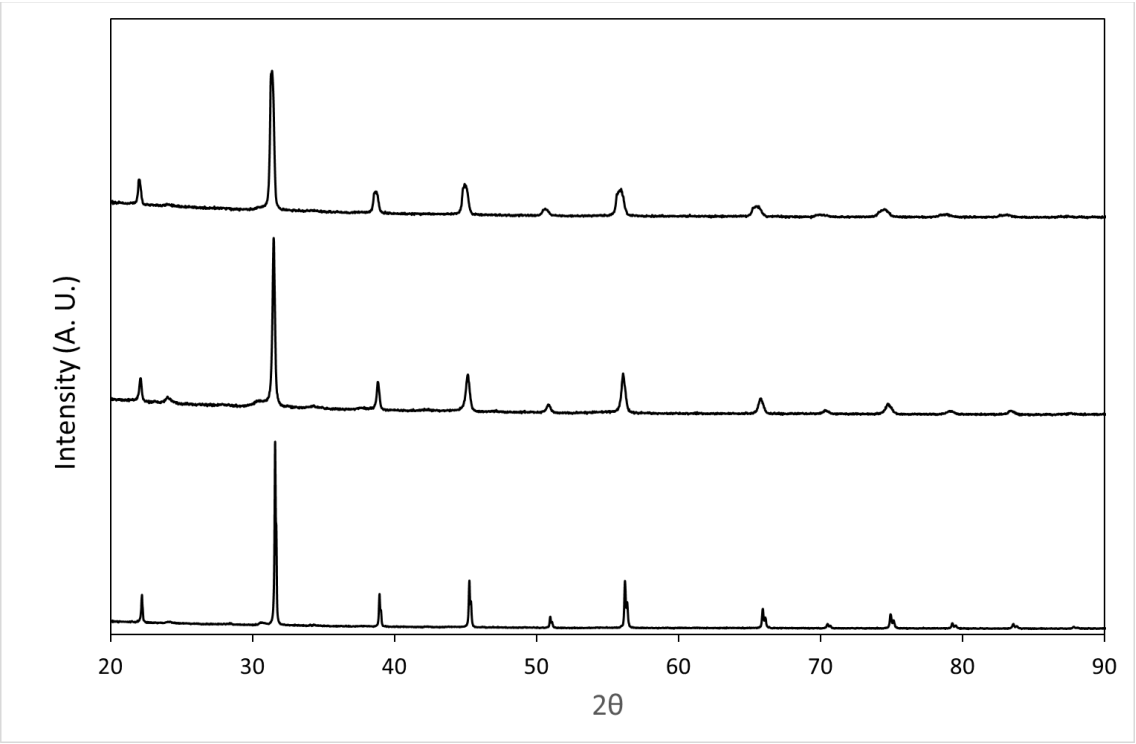

Figure 4.2. Powder X-ray diffraction from top to bottom: $Ba_{0.90}Sr_{0.10}Fe_{0.85}B_{0.15}O_{3-\delta}$, $Ba_{0.90}Sr_{0.10}Fe_{0.90}B_{0.10}O_{3-\delta}$ and $Ba_{0.90}Sr_{0.10}Fe_{0.95}B_{0.05}O_{3-\delta}$

Thermogravimetric analysis was performed on the materials to determine the mass loss in N_2, from which the average Fe-site oxidation state could be determined. The results of these analyses are shown in Table 4.1, indicating the oxygen content increases with increasing borate doping.

TABLE 4.1. Oxygen content and average Fe oxidation state for $Ba_{0.90}Sr_{0.10}Fe_{1-x}B_xO_{3-\delta}$

X	**% Mass Loss**	**δ Value**	**Average Fe Oxidation State**
0.00	1.80	0.24	3.71
0.05	2.91	0.08	3.89
0.10	2.81	0.10	3.90
0.15	2.16	0.19	3.72

A structural model with space group *P m -3 m* was refined using the GSAS-II suite of programs using the experimental powder X-ray diffraction data. As with other oxyanion doped perovskite materials, the iron and boron were fitted to the B-site with the theoretical stoichiometric amounts. The barium and strontium atoms were placed on the A-site with fractional occupancies set at theoretical stoichiometric amounts. The oxygen occupancy was set to the value calculated from the TGA data discussed above. The unit cell parameters from the refinement are shown in Table 4.2.

TABLE 4.2. Cell parameters and goodness of fit values for $Ba_{0.90}Sr_{0.10}Fe_{1-x}B_xO_{3-\delta}$

X	**a (Å)**	**$_w$Rp**	**Rp**	**χ^2**
0.05	4.0052(2)	4.81	2.57	1.87
0.10	4.0127(5)	4.20	2.64	1.59
0.15	4.0288(1)	4.62	2.63	1.76

The unit cell parameters were found to show a small increase with increased borate incorporation. As the average oxidation state of iron is constant within borate doped materials (with the exception of x = 0.15), this increased in volume may be attributed to an increase in oxygen content on the introduction of B^{3+} in place of Fe, as suggested by the TGA data.

^{57}Fe Mössbauer spectroscopy data was collected in order to determine Fe oxidation states within the undoped and doped systems. All samples were measured at room temperature (298 K).

Undoped $Ba_{0.90}Sr_{0.10}FeO_{3-\delta}$ was determined to be paramagnetic, Figure 4.3. There are 3 doublets seen. The first with the chemical isomer shift of δ = 0.32 mms^{-1} is from Fe^{3+} in an octahedral co-ordination while the other shift δ = 0.09 mms^{-1} and δ = 0.15 mms^{-1} are from Fe^{4+} and $Fe^{3.5+}$ respectively.

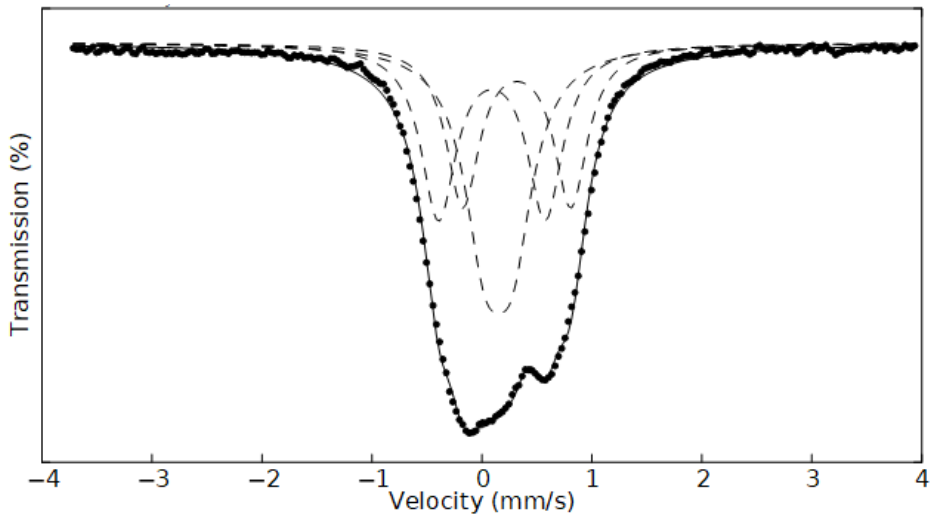

Figure 4.3. ^{57}Fe Mossbauer spectroscopy recorded of $Ba_{0.90}Sr_{0.10}FeO_{3-\delta}$ at 298K

Doped samples showed a range of oxidation states and difficulty with fitting due to possible magnetic impurity, potentially presences of iron oxide (Fe_2O_3) distorting the paramagnetic absorptions, Figure 4.4. Therefore, finding a trend between oxidation states and the amount of doping within the structure was difficult. The oxidation states assigned to $Ba_{1-x}Sr_xFe_{1-y}B_yO_{3-\delta}$ were; Fe^{3+} in an octahedral co-ordination (δ = 0.32-0.37 mms^{-1}), Fe^{3+} in a lower co-ordination (δ = 0.20-0.24 mms^{-1}), $Fe^{3.5+}$ (δ = 0.14-0.15 mms^{-1}) and Fe^{4+} (δ = 0.00-0.14 mms^{-1}).

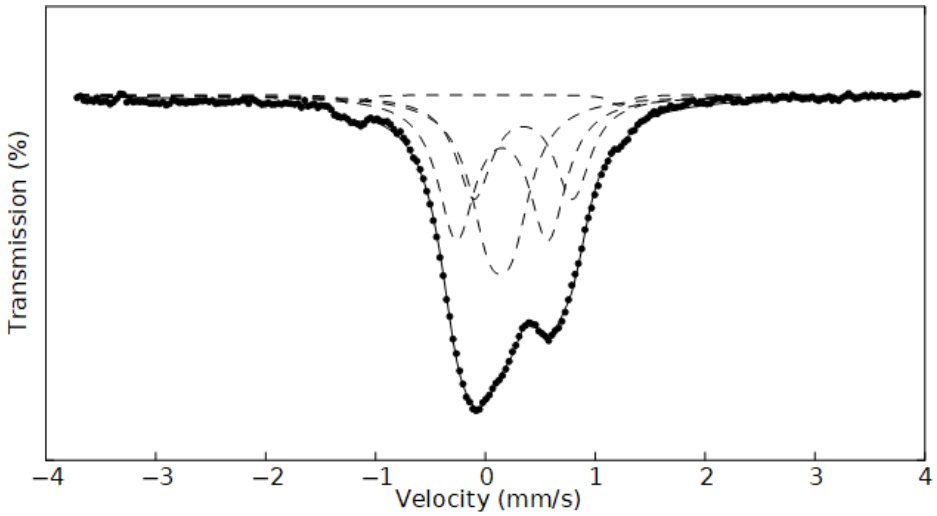

Figure 4.4. ^{57}Fe Mossbauer spectroscopy recorded of $Ba_{0.90}Sr_{0.10}Fe_{0.95}B_{0.05}O_{3-\delta}$ at 298K

An interesting observation is no chemical isomer shift from Fe^{5+}, usually seen around δ = -0.09 mms^{-1}. Previous literature on oxyanion doping, specifically silicate incorporation has shown disproportionation of Fe^{4+} to Fe^{3+} and Fe^{5+} due to substitution of Fe^{4+} and Si^{4+}. However, disproportionation seems not to occur with borate doping and may explain the high Fe oxidation state compared to other oxyanion doped perovskite system.

Table 4.3 ^{57}Fe Mössbauer Spectroscopy spectrum from $Ba_{0.90}Sr_{0.10}FeO_{3-\delta}$ and $Ba_{0.90}Sr_{0.10}Fe_{0.95}B_{0.05}O_{3-\delta}$ at 298K

Compound	**Assignment**	**δ ± 0.02 (mms^{-1})**	**Δ ± 0.08 (mms^{-1})**	**Area ± 5% (%)**
$Ba_{0.90}Sr_{0.10}FeO_{3-\delta}$	Fe^{3+} oct	0.32	0.98	29
	$Fe^{3.5+}$	0.15	0.97	32
	Fe^{4+}	0.09	0.25	39
$Ba_{0.90}Sr_{0.10}Fe_{0.95}B_{0.05}O_{3-\delta}$	Fe^{3+} oct	0.34	0.90	27
	$Fe^{3.5+}$	0.15	0.83	39
	Fe^{4+}	0.14	0.21	33

4.3.1.2 $Ba_{0.50}Sr_{0.50}Fe_{1-x}B_xO_{3-\delta}$

Powder X-ray diffraction data were collected on $Ba_{0.50}Sr_{0.50}Fe_{1-x}B_xO_{3-\delta}$ compositions for x = 0.05, 0.10, showing the formation of a pure cubic perovskite phase, Figure 4.5. However at higher values such as x = 0.15, a small impurity is noted around 29^o and therefore higher values of x were not investigated.

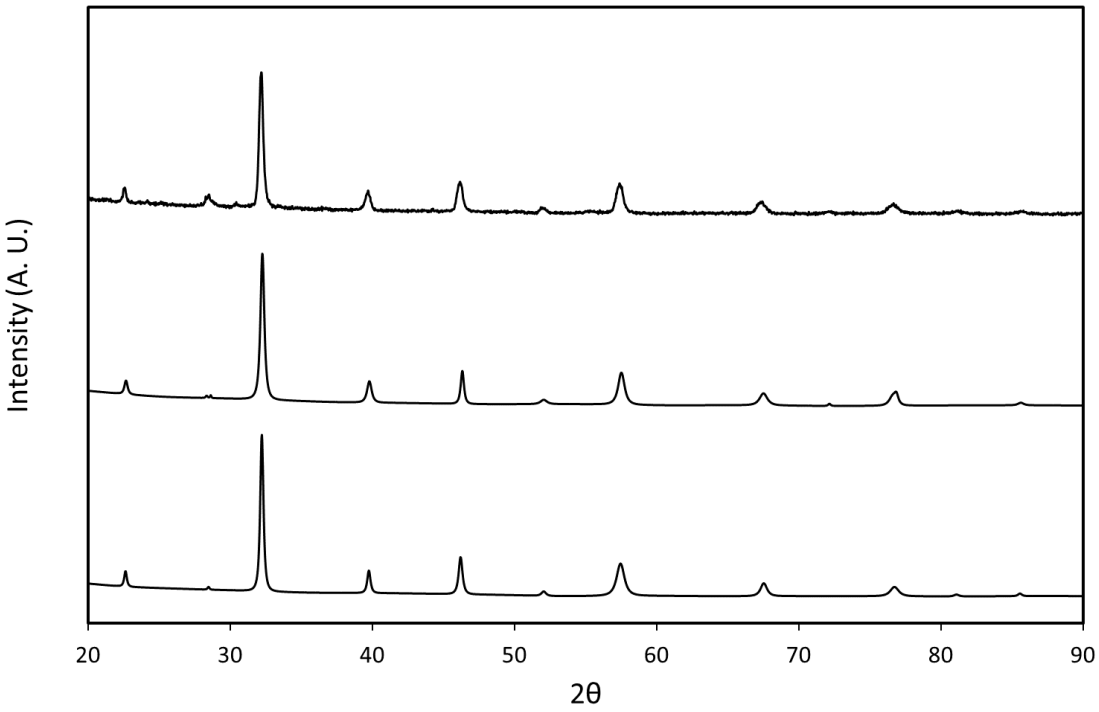

Figure 4.5. Powder X-ray diffraction from top to bottom: $Ba_{0.50}Sr_{0.50}Fe_{0.85}B_{0.15}O_{3-\delta}$, $Ba_{0.50}Sr_{0.50}Fe_{0.90}B_{0.10}O_{3-\delta}$, $Ba_{0.50}Sr_{0.50}Fe_{0.95}B_{0.15}O_{3-\delta}$. Weak impurity for $Ba_{0.50}Sr_{0.50}Fe_{0.85}B_{0.15}O_{3-\delta}$ was highlighted within a box.

Thermogravimetric analysis was undertaken to measure the mass loss of the material under N_2, and so calculate the oxygen content and the average Fe oxidation state for the $Ba_{0.50}Sr_{0.50}Fe_{1-x}B_xO_{3-\delta}$ series, Table 4.4.

Table 4.4 Oxygen content and Fe-site oxidation state for $Ba_{0.50}Sr_{0.50}Fe_{1-x}B_xO_{3-\delta}$

X	**% Mass Loss**	**δ Value**	**Average B-site Metal Oxidation State**
0.00	3.19	0.07	3.85
0.05	1.75	0.27	3.48
0.10	2.40	0.19	3.69
0.15	2.43	0.19	3.73

Upon borate doping, an increase in oxygen vacancies is observed. The Fe oxidation state was shown to substantially decrease with initial borate doping and then increase, but not to the highs of the undoped. Fe site oxidation state was shown to be lower than reported for $Ba_{0.90}Sr_{0.10}Fe_{1-}B_xO_{3-\delta}$ series of materials.

Rietveld refinement was performed using the GSAS-II suite of programs based on the space group *P m -3 m* perovskite model using the collected powder X-ray diffraction data for the borate doped phases. As discussed above, the protocol for refinement was the same with the only difference being the occupancies of the barium and strontium atoms placed on the A-site changed to match the theoretical stoichiometric amounts. Unit cell parameters and goodness of fit parameters are presented in Table 4.5.

Table 4.5 Cell parameters and goodness of fit values for $Ba_{0.50}Sr_{0.50}Fe_{1-x}B_xO_{3-\delta}$

X	**a (Å)**	**$_w$Rp**	**Rp**	**χ^2**
0.05	3.9267(4)	2.86	2.03	1.41
0.10	3.9283(9)	2.98	2.02	1.47
0.15	3.9309(9)	3.30	1.97	1.62

The lattice parameters were found to show a small increase with increase in borate content, slightly smaller to that of the $Ba_{0.90}Sr_{0.10}$ series. This increase in volume may be attributed to an increase in oxygen content on the introduction of B^{3+} in place of Fe, given the average Fe oxidation state is approximately constant.

4.3.2 Conductivity Measurements

4.3.2.1 $Ba_{0.90}Sr_{0.10}Fe_{1-x}B_xO_{3-\delta}$

Conductivity measurements of the borate doped $Ba_{0.90}Sr_{0.10}Fe_{1-x}B_xO_{3-\delta}$ materials in air are shown in Figure 4.6 and Table 4.6.

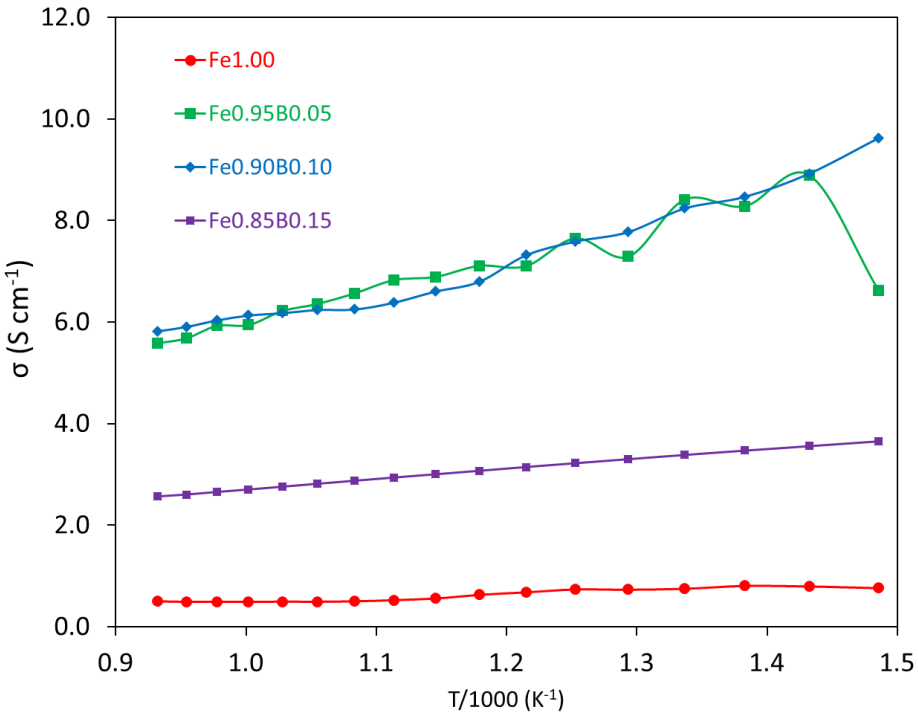

Figure 4.6. Plot of σ versus 1000/T for $Ba_{0.90}Sr_{0.10}Fe_{1-x}B_xO_{3-\delta}$

Table 4.6. Total conductivity data for $Ba_{0.90}Sr_{0.10}Fe_{1-x}B_xO_{3-\delta}$ in air at 700 °C.

Compound	**Conductivity (S cm^{-1})**
$Ba_{0.90}Sr_{0.10}FeO_{3-\delta}$	0.49
$Ba_{0.90}Sr_{0.10}Fe_{0.95}B_{0.05}O_{3-\delta}$	6.22
$Ba_{0.90}Sr_{0.10}Fe_{0.90}B_{0.10}O_{3-\delta}$	6.18
$Ba_{0.90}Sr_{0.10}Fe_{0.85}B_{0.15}O_{3-\delta}$	2.75

The data reveal a slight enhancement in conductivity as a result of the transition from a hexagonal to a more symmetrical cubic system with borate doping up to x = 0.10. Beyond this concentration, however, there's a decrease in conductivity with further borate doping. This reduction in conductivity at higher doping levels is likely attributed to the formation of impurity phases in the samples, a consequence of surpassing the solubility limit of borate for concentrations greater than x = 0.10.

The value at 400 °C for $Ba_{0.90}Sr_{0.10}Fe_{0.95}B_{0.05}O_{3-\delta}$ is also an outlier that does not match the trend. This measurement should be repeated.

4.3.2.2 $Ba_{0.50}Sr_{0.50}Fe_{1-x}B_xO_{3-\delta}$

Conductivity measurements of borate doped $Ba_{0.50}Sr_{0.50}Fe_{1-x}B_xO_{3-\delta}$ materials in air are shown in Figure 4.7 and Table 4.7.

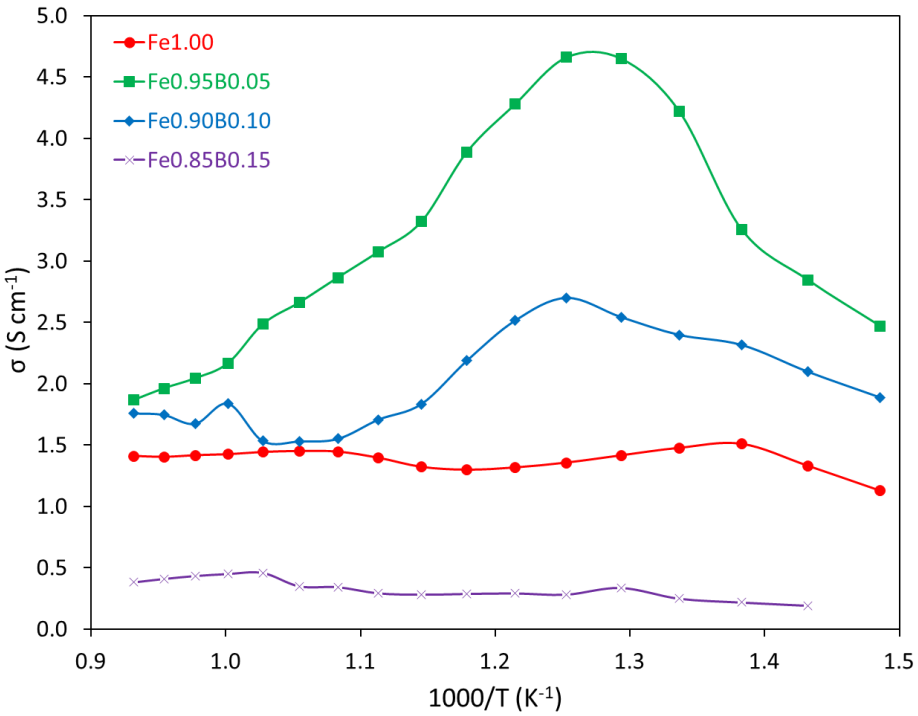

Figure 4.7. Plot of σ versus 1000/T for $Ba_{0.50}Sr_{0.50}Fe_{1-x}B_xO_{3-\delta}$

Table 4.7. Total conductivity data for $Ba_{0.50}Sr_{0.50}Fe_{1-x}B_xO_{3-\delta}$ in air at 700 °C.

Compound	**Conductivity (S cm^{-1})**
$Ba_{0.50}Sr_{0.50}FeO_{3-\delta}$	1.44
$Ba_{0.50}Sr_{0.50}Fe_{0.95}B_{0.05}O_{3-\delta}$	2.49
$Ba_{0.50}Sr_{0.50}Fe_{0.90}B_{0.10}O_{3-\delta}$	1.53
$Ba_{0.50}Sr_{0.50}Fe_{0.85}B_{0.15}O_{3-\delta}$	0.46

The results highlight that $Ba_{0.50}Sr_{0.50}Fe_{1-x}B_xO_{3-\delta}$ samples showed slightly lower conductivity than $Ba_{0.90}Sr_{0.10}Fe_{1-x}B_xO_{3-\delta}$. The initial increase in conductivity for x = 0.05 may result from the observed change in the Fe oxidation state. When the dopant level increased further, the conductivity then deceases due to the borate disrupting the Fe-O network and presence of impurities. Further decreases in conductivity of x = 0.05 and 0.10 borate doped samples are due to oxygen loss at these higher temperatures reducing the Fe^{4+} content.

4.4 Conclusions

In this work we have shown that borate can be successfully incorporated into $Ba_{1-x}Sr_xFeO_{3-\delta}$. Thermogravimetric analysis was used to calculate the oxidation states of the Fe and found that in both $Ba_{0.90}Sr_{0.10}$ and $Ba_{0.50}Sr_{0.50}$ show contrasting trends. ^{57}Fe Mössbauer Spectroscopy studies of $Ba_{0.90}Sr_{0.10}FeO_{3-\delta}$ and $Ba_{0.90}Sr_{0.10}Fe_{0.95}B_{0.05}O_{3-\delta}$ indicating an increase in $Fe^{3.5+}$ upon borate doping, although no disproportion was seen, as observed within other oxyanion doped systems.

Conductivity measurements showed there was a general improvement upon borate within both $Ba_{0.90}Sr_{0.10}$ and $Ba_{0.50}Sr_{0.50}$ although $Ba_{0.90}Sr_{0.10}Fe_{0.95}B_{0.05}O_{2.81}$ showed the largest value. Both series of samples also demonstrated a decrease at higher borate levels attributed to the presence of impurities as the solubility limited was exceeded.

Whilst the conductivity of both series of materials were not as high as other reported within literature or this thesis and therefore should not be further investigated for the potential use as SOFC cathode materials, there could be potential interest as an ORR (oxygen reduction reaction) catalyst at lower temperature (300-500 ^{o}C).

4.5 References

1. A Orera, P Slater, *Chem. Mater.,* **22**, 675-690, (2010)
2. A. J. Jacobson, *Chem. Mat.,* **22**, 660-674,(2010)
3. A. Lashtabeg and S. J. Skinner, *J. Mater. Chem.,* **16**, 3161-3170, (2006)
4. J. H. Kuo, H. U. Anderson and D. M. Spalin, *J. Solid State Chem.,* **87**, 55-63, (1990)
5. H. Yokokaw, N. Sakai, T. Kawada and M. Dokiya, *Solid State Ion.,***40-1,** 398-401 (1990)
6. J. Deakin, I.Trussov, A. Gibbs, E. Kendrick and P. R. Slater, *Dalton Trans.,* **47,** 12901-12906, (2018)
7. A. Jarvis and P. R. Slater, *Crystals,***7,** 169 (2017)
8. D. Perez-Coll, J. C. Perez-Flores, N. Nasani, P. R. Slater and D. P. Fagg, *J. Mater. Chem. A.* **4,** 11069-11076 (2016)
9. C. A. Hancock, J. M. Porras-Vazquez, P. J. Keenan and P. R. Slater., *Dalton Trans.,* **44,** 10559-10569 (2015)
10. A Benes, A Molinari, R Witte, R Kruk, J Brotz, R Chellali, H Hahn, O Clemens, *Materials,* **11,** 52 (2018)
11. P Sukkurji, A Molinari, A Benes, C Loho, V Chakavadhanula, S Garlapati, R Kruk, O Clemens, *J. Phys. D.,* **50,** 11, (2017)
12. P. Knochel, P Keenan, C Loho, C Reitz, R Witte, K Knight, A Wright, H Hahn, P Slater, O Clemens, *J. Mat Chem A.,* **4,** 3415-3450 (2016)
13. O Clemens, R Haberkorn, P Slater, H Beck, *Solid. State. Sci*, **12,** 1455-1463 (2010)
14. J Porras-Vazquez, T Pike, C Hancock, J Marco, F Berry, P Slater *J. Mater. Chem. A.*, **1**, 11834-11841, (2013)
15. B. H. Toby, R. B. Von Dreele, *J. Appl. Chem,* **46**(2), 544-549 (2013)

Chapter 5: Synthesis of borate doped $La_{10-x}Y_xGe_6O_{27}$

5.1 Introduction

One of the main research areas for solid oxide fuel cells and electrolysers (SOFC/SOEs) is the production of electrolytes which can be used at lower operating temperatures (below 600 ^oC). (1-3) This is due to the fact that high temperature operation can lead to rapid degradation of fuel cells, increased operating costs, and limited usage within portable devices. A proposed alternative electrolyte to fluorite-based materials is lanthanum apatite materials with the general formula $La_{10}(Si/Ge)_6O_{26+y}$. (4-5)

In these apatite materials, Figure 5.1, the conventional oxygen vacancy conduction mechanism of other electrolyte materials does not dominate; instead, they are thought to conduct via oxygen ions located in interstitial sites which is mediated by the high oxygen excess in the structure. For the Si based systems, it is believed that the main form of interstitial oxide ion conductivity is down the centre channels which exist in apatite-type structures. In these systems the oxygen excess achievable is limited to y = 0.5. (6-8) However, the Ge based analogues can have a higher oxygen excess than their corresponding silicates, leading to higher conductivities.

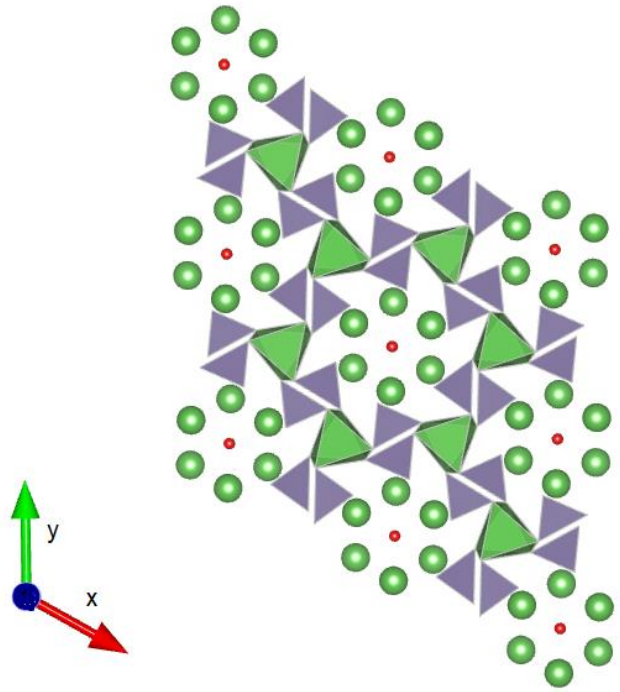

Figure 5.1: A visualisation of a lanthanum apatite structure (Space Group P 63/m) showing a $La_4(MO_6)_6$ with the La_6O_2 units filling the channels within the framework.

Modelling and experimental studies suggest that oxygen interstitials preferentially incorporate between two GeO_4 tetrahedra. There is local relaxation around the oxygen interstitial sites leading to Ge increasing its coordination number, resulting in the formation of five coordinate Ge which provides an alternative conduction pathway across the material. A complication with lanthanum germanate structures is their distortion from hexagonal to triclinic for high oxygen excess ($y > 0.5$). Apatite germanate structures are made of a $La_4(GeO_4)_6$ framework containing the GeO_4 tetrahedra and LaO_6 trigonal prisms; La_6O_2 units then occupy the gaps within the structure. (9-11) As these are large, there is a mismatch in size which leads to the tetrahedra tilting and, therefore, distortion to a triclinic unit cell. This increases the defect trapping due to the lower symmetry, resulting in lower oxide ion conductivity. Doping with a smaller rare earth metal, such as Y, stabilises the hexagonal structure due to preferential substitution within the framework increasing the size of the

cavities and removing the need for tetrahedral tilting. Research conducted by Orera et al. showed that $La_{10-x}Y_xGe_6O_{27}$ $1 \leq x \leq 3$ successfully stabilised the hexagonal structure, increasing conductivity through a range of temperatures. Increasing the Y content further, $x \geq 4$ showed distortions back to the lower symmetry triclinic structure. (12-14)

There are two proposed interstitial-oxide ion conduction pathways in apatite germanates; the conventional route, where ions move down the channel, and the alternative, across the structure perpendicular to the channel via five coordinate Ge involving the sequential bond forming and breaking between Ge and oxygen ions. (15) The aim of this chapter was to confirm which mechanism are present within the $La_{10}Ge_6O_{27}$ and $La_{10-x}Y_xGe_6O_{27}$ (X = 1 and 2) structures by doping with borate. If oxyanions (such as borates) could block the centre channel in the apatite structure, proof may be found for the alternative oxygen interstitial conduction method perpendicular to the channel. It is also hypothesised that the addition of borate into the structure would introduce larger amounts of interstitial oxide ions, therefore increasing conductivity. (16-19) Herein, the successful synthesis of boron doped lanthanum germanate appetites are reported via a Pechini synthesis route. Two series were studied one with boron doped into the channel and a second with boron substitution into the Ge site of $(La_{10-x}Y_x)Ge_6O_{27}$ materials via a Pechini synthesis route. (20-22) These samples were shown to have a good oxide ion conductivity associated with their high levels of interstitial oxide ions.

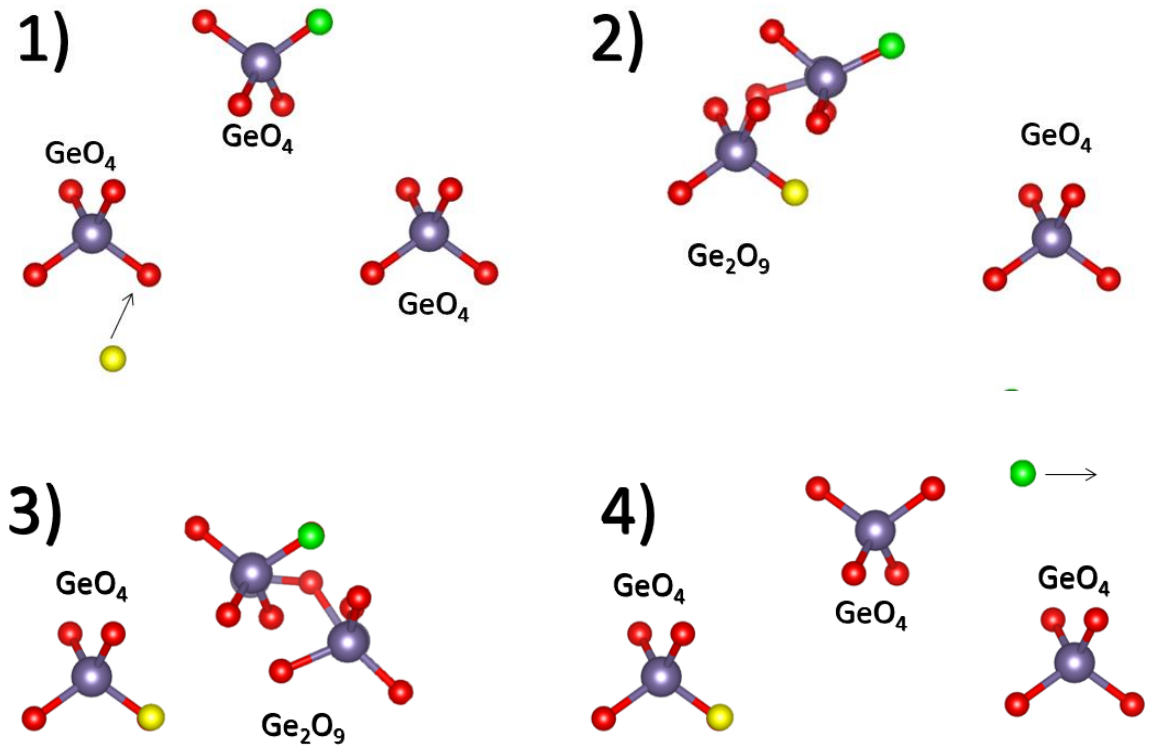

Figure 5.2: Visualisation of secondary conduction mechanism perpendicular to the centre channel. Reproduction with permission form Kendrick et al. (5)

5.2 Experimental

Samples were synthesised via a Pechini Methodology. $La(NO_3)_3$, $Y(NO_3)_3$, and soluble GeO_2 were weighed out according to requirements, and were in stoichiometric quantities were all dissolved in deionised water whilst heating and stirring. Citric Acid and Ethylene Glycol were then added (1:1:3 molar ratio, Reagents: Ethylene Glycol: Citric Acid) and left to stir under heating for roughly 3 hours until the solution gelled. The samples were then heated at 350 ^oC (1 $^oC\ min^{-1}$) for 1 hour. The samples were then ground with required stoichiometric amounts of H_3BO_3 were added. They were then fired at 700 ^oC for 2 hours, reground, and then reheated at 950 ^oC for 12 hours before finishing with a final heat treatment, 1100 °C for 4 hours.

Powder X-Ray diffraction data were collected to determine lattice parameters and phase purity of samples. Data were collected on the Panalytical Empyrean diffractometer equipped with the Pixcel 2D detector (Cu Kα radiation). The GSAS-II suite of programs was used to determine unit cell parameters. (23)

FT-IR Spectroscopy measurements were carried out to confirm the presence of borate and its' coordination. The measurements were collected on a Bruker Alpha II FTIR-Spectrometer with the platinum ATR attachment.

For conductivity measurements, the sintered pellets were coated with platinum paste on either side, platinum electrodes were attached to both faces, and the samples were heated at 950 ^oC for 1 hour to ensure bonding to the pellet. The conductivities were then measured in a temperature range of 400 ^oC to 800 ^oC by AC impedance measurements (Hewlett Packard 4192A impedance analyser) in the range 0.1 to 103 kHz with ac signal amplitude of 100 mV.

5.3 Results and Discussion

5.3.1 B doped $La_{10}Ge_6O_{27}$

Powder X-ray diffraction data were collected for undoped $La_{10}Ge_6O_{27}$ and indicated the formation of triclinic apatite with the space group *P21/c* consistent with previously literature. (12-14)

The synthesis of $La_{10}Ge_6O_{27}(BO_{1.5})_x$ (for x= 0.5, 1.0 and 1.5) was also examined and these resulted in the formation of a hexagonal apatite (*P-63m*) phase according to the powder X-ray diffraction data, Figure 5.3.

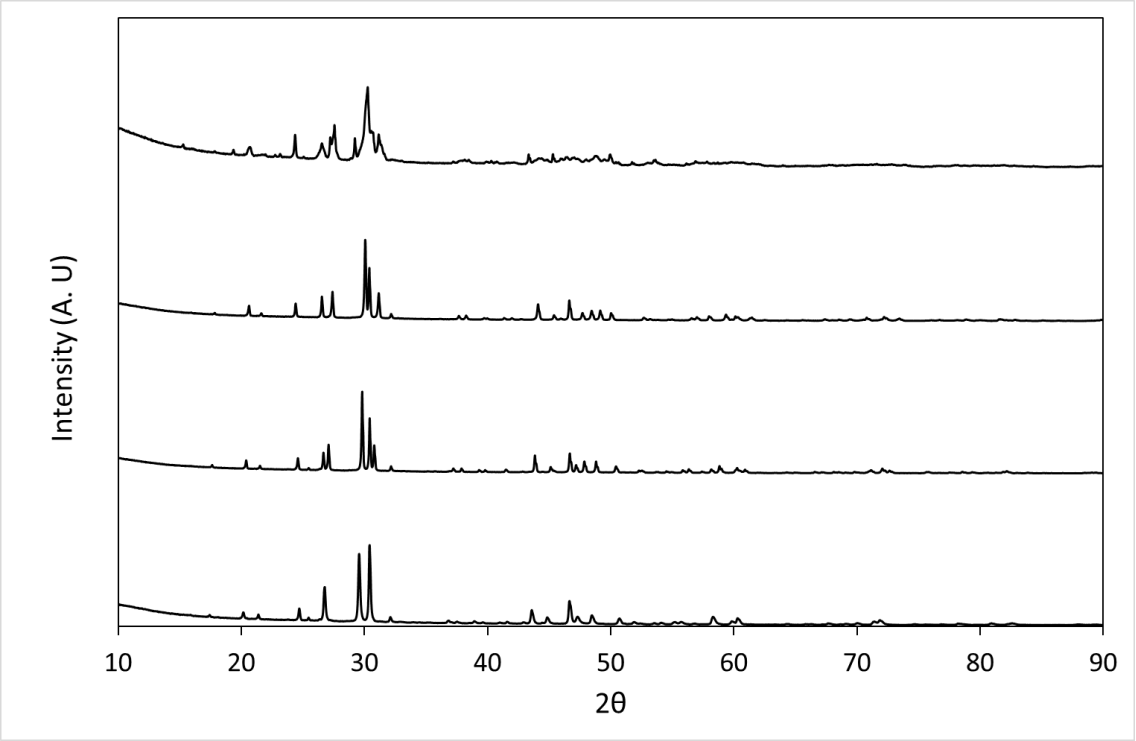

Figure 5.3: Powder X-ray Diffraction from to top to bottom: $La_{10}Ge_6O_{27,}$ $La_{10}Ge_6O_{27}(BO_{1.5})_{0.5}$, $La_{10}Ge_6O_{27}(BO_{1.5})_{1.0,}$ $La_{10}Ge_6O_{27}(BO_{1.5})_{1.5}$

Cell parameters were determined and these are shown in Table 5.1. The unit cell volumes were found to show a small increase, with increased borate present within the central

channel of the hexagonal apatite structure. Interestingly, these were differences in the trends of the a and c parameters. A parameter was shown to increase with increasing borate content, while the c parameter was shown to decrease. These changes are consistent with prior work (5) examining the effect of oxygen content on cell parameters and indicates an increasing in interstitial oxygen. These changes are much higher than that of previous reports for $La_{10-x}Ge_6O_{27-3x/2}$, consistent with the much higher oxygen excess.

Table 5.1: Cell parameters and goodness of fit values for $La_{10}Ge_6O_{27}(BO_{1.5})_x$

x	**a (Å)**	**c (Å)**	**Unit Cell Parameters ($Å^3$)**	**$_wRp$**	**Rp**	**χ_2**
0.5	9.9320(4)	7.2820(7)	622.103	5.53	1.89	2.92
1.0	10.0466(7)	7.2314(6)	632.122	5.97	1.88	3.18
1.5	10.1509(9)	7.1948(4)	642.049	6.55	1.93	3.48

Overall the cell volume shows a positive linear trend with increasing borate content due to the incorporation of the oxyanion within the channel and consequently increase in oxygen content, Figure 5.4.

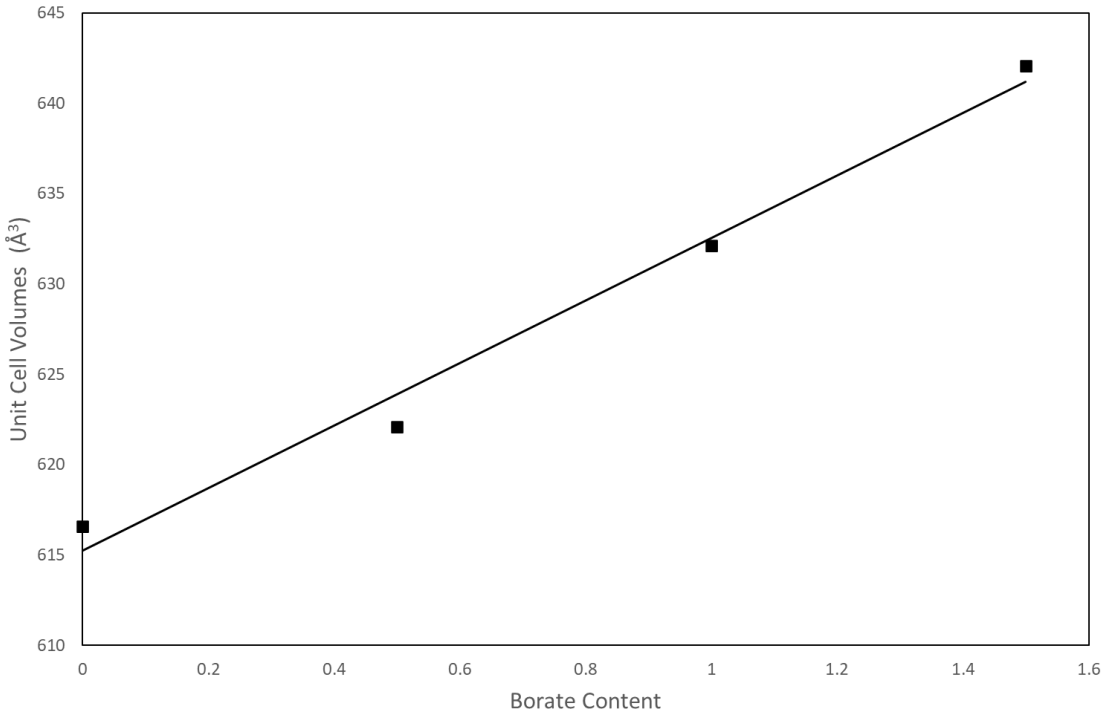

Figure 5.4: Unit Cell Volumes vs Borate content for $La_{10}Ge_6O_{27}(BO_{1.5})_x$

FT-IR spectra analysis was used to confirm the presence of borate composition with the $La_{10}Ge_6O_{27}$ apatite structure. Three key peaks which were evaluated as occurring from borate were examined at 880, 960 and 1300 cm^{-1}. Borate peaks at 880 and 960 cm^{-1} arise from BO_4^{5-} units whilst the peak 1300 cm^{-1} from BO_3^{3-} unit. The undoped material was observed to have no peaks present in these regions with the low level borate material containing 880 and 960 cm^{-1} while for only the highest borate containing material, $La_{10}Ge_6O_{27}(BO_{1.5})_{1.5}$ was a clear 1300 cm^{-1} peak present, Figure 5.5. As the 1300 cm^{-1} region appears to only arise at higher borate concentrations, this suggests the preferred for borate incorporation within the channel is BO_4^{5-} unit with BO_3^{3-} units only observed at higher doping levels.

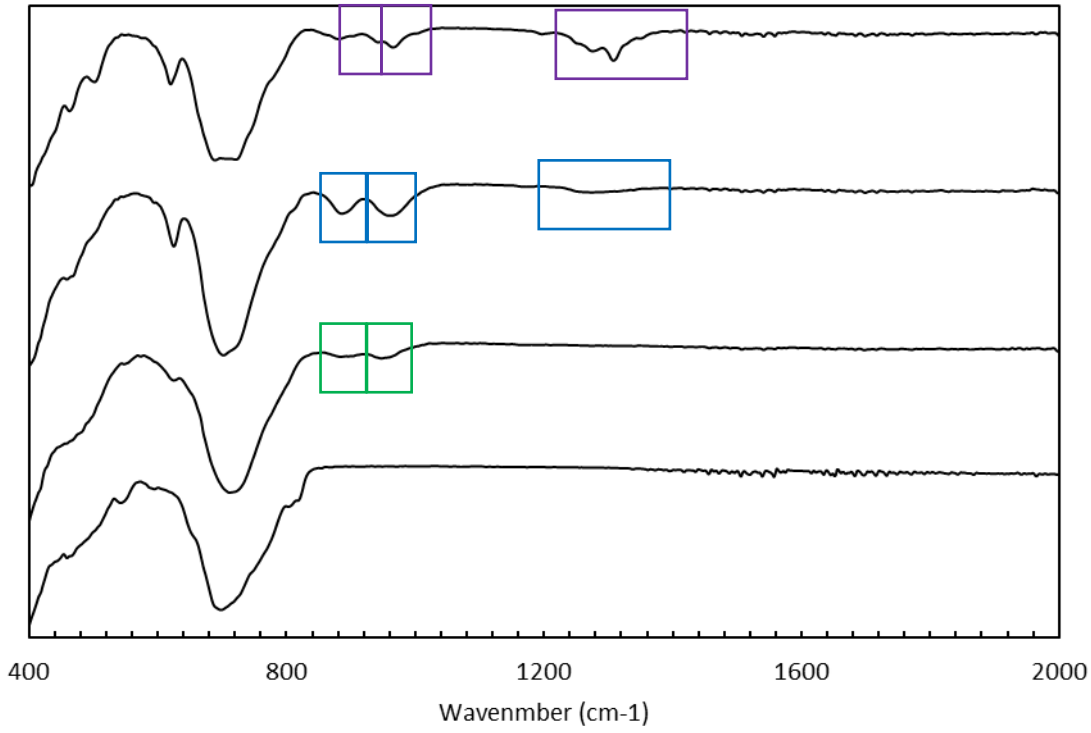

Figure 5.5. IR Spectra from top to bottom: $La_{10}Ge_6O_{27}(BO_{1.5})_{1.5}$, $La_{10}Ge_6O_{27}(BO_{1.5})_{1.0}$, $La_{10}Ge_6O_{27}(BO_{1.5})_{0.5}$ and $La_{10}Ge_6O_{27}$,

The conductivity data (Figure 7.6), show that there is an increase in conductivity when low levels of borate are introduced compared to the undoped variant. This increase in conductivity is attributed to a stabilisation of the higher conducting hexagonal phase when borate is doped as well as an increase in oxygen interstitials.

With higher levels of doping, i.e. $La_{10}Ge_6O_{27}(BO_{1.5})_{1.0}$ and $La_{10}Ge_6O_{27}(BO_{1.5})_{1.5}$ the conductivity is observed to be lower than the undoped at low temperatures. The decrease suggests a surplus or blockage of the central channel with increased concentration of borate and thus a loss of the oxide interstitial conduction mechanism along the channel centre. However, significantly there is still good conductivity in these samples, which is consistent with a secondary mechanism is still being present.

At elevated temperatures, both $La_{10}Ge_6O_{27}(BO_{1.5})_{1.0}$ and $La_{10}Ge_6O_{27}(BO_{1.5})_{1.5}$ exhibit a sharp rise in conductivity, leading to a scenario where, at the highest temperatures measured, the borate-doped samples achieve similar levels of conductivity. This indicates that all samples exhibit enhanced conductivity despite the introduction of borate, which is presumed to obstruct the channel conduction pathway.

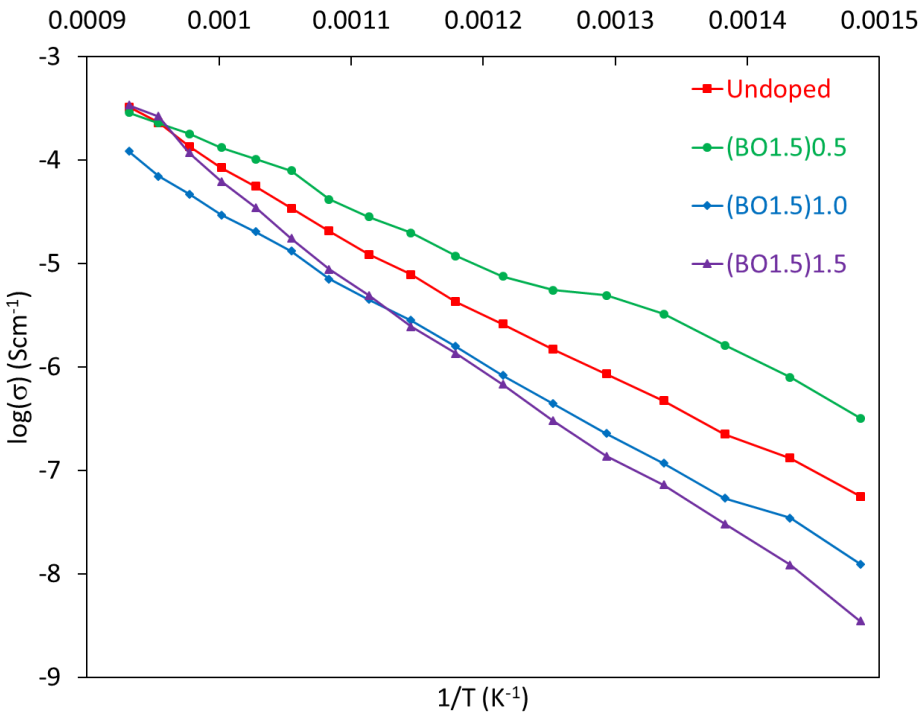

Figure 5.6: Plot of log σ versus 1/T for $La_{10}Ge_6O_{27}$ and $La_{10}Ge_6O_{27}(BO_{1.5})_x$

5.3.2 B doped $La_9Y_1Ge_6O_{27}$

The Powder X-ray diffraction patterns in Figure 5.7 show a transition from the triclinic phase present in undoped $La_9Y_1Ge_6O_{27}$ to hexagonal with increased borate incorporation. However, unlike B-doped $La_{10}Ge_6O_{27}$, an impurity phase is present at around 29° in all borate-doped samples. Due to these significant impurities, no Rietveld refinement was performed.

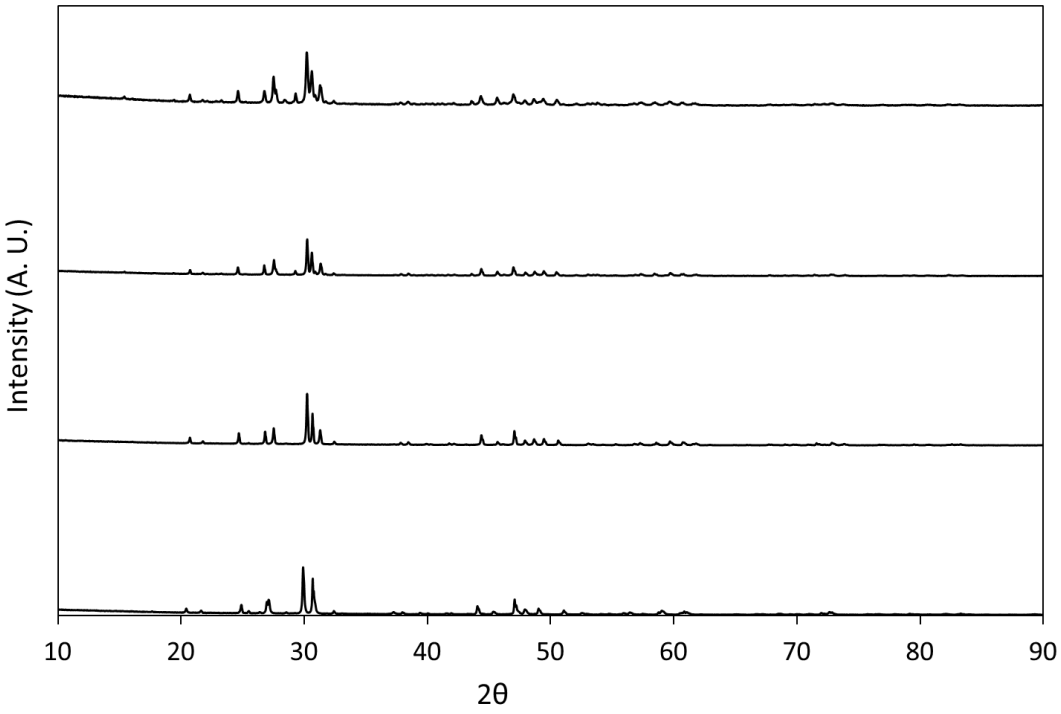

Figure 5.7: Powder X-ray Diffraction data for (from to top to bottom) $La_9Y_1Ge_6O_{27}$, $La_9Y_1Ge_6O_{27}.(BO_{1.5})_{0.5}$, $La_9Y_1Ge_6O_{27}.(BO_{1.5})_{1.0}$, $La_9Y_1Ge_6O_{27}.(BO_{1.5})_{1.5}$.

Similarly, to Figure 5.4, the IR spectra for the borate doped $La_9Y_1Ge_6O_{27}$ structure (Figure 5.8), also show three clear borate peaks at 900, 980, and 1300 cm^{-1}. For the undoped samples, the peaks do not appear in the spectrum; they then grow with increasing borate concentration. Again, the 1300 cm^{-1} peak is only seen for the higher dopant. This confirms the presence of BO_4^{5-} at low B content with BO_3^{3-} being observed for higher B content.

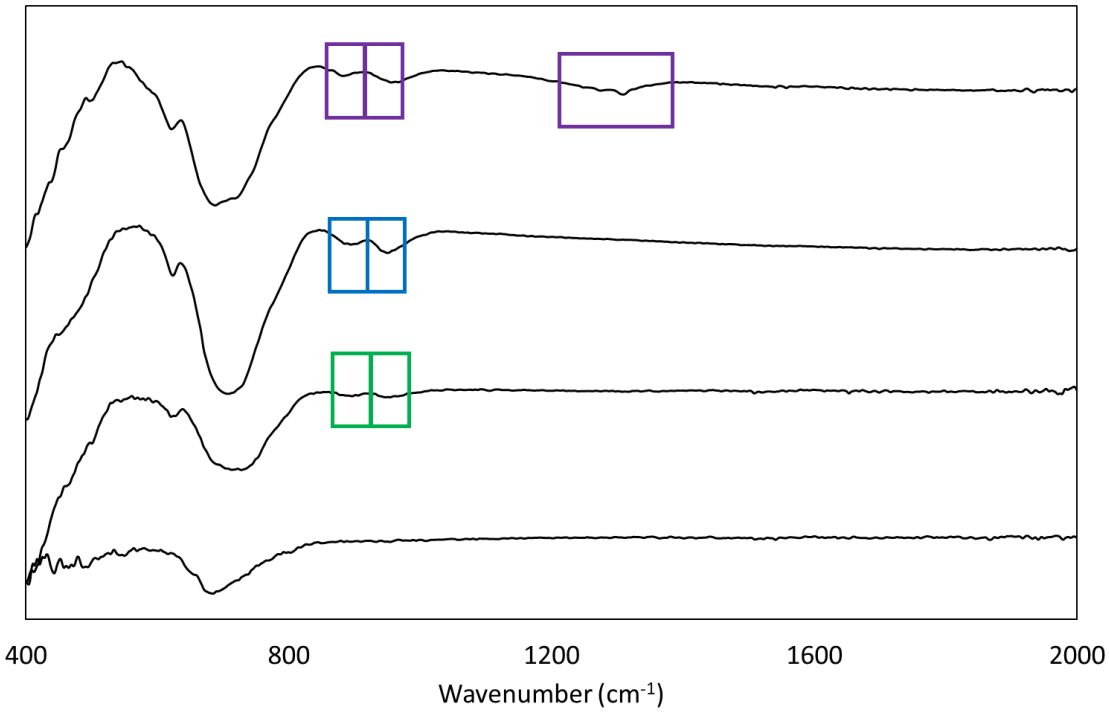

Figure 5.8: IR Spectra from top to bottom: $La_9Y_1Ge_6O_{27}.(BO_{1.5})_{1.5.}$, $La_9Y_1Ge_6O_{27}.(BO_{1.5})_{1.0}$, $La_9Y_1Ge_6O_{27}.(BO_{1.5})_{0.5}$, $La_9Y_1Ge_6O_{27}$

As for the borate doping $La_{10}Ge_6O_{27}$, there is a small increase in conductivity upon low levels of borate introduction for these particular samples, which is likely due to the stabilisation of the hexagonal structure. The conductivity is particularly higher for $La_9Y_1Ge_6O_{27}.(BO_{1.5})_{0.5}$ at lower temperatures compared to the undoped sample. However, upon further borate incorporation the conductivity significantly decreases with that for $La_9Y_1Ge_6O_{27}.(BO_{1.5})_{1.5}$ being significantly lower than the undoped sample, consistent with the centre channel being blocked by borate incorporation, such that the conduction mechanism perpendicular to this channel is only possible.

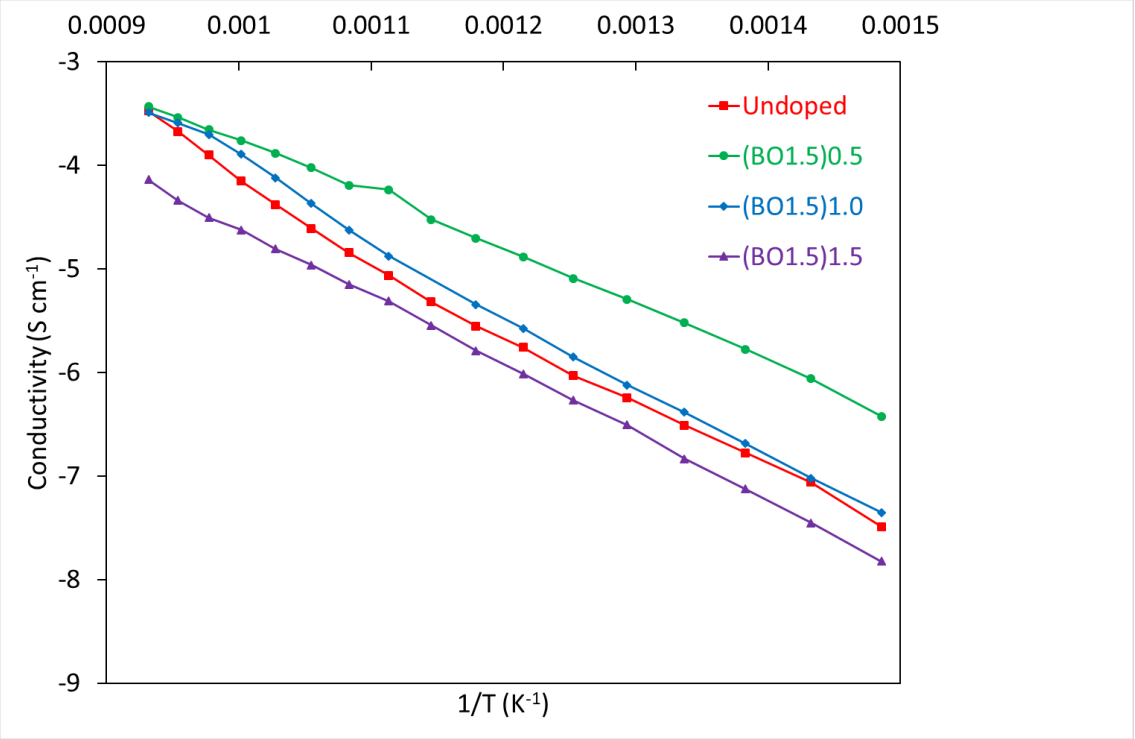

Figure 5.9: Plot of log σ versus 1/T (K^{-1}) for $La_9Y_1Ge_6O_{27}$ and $La_9Y_1Ge_6O_{27}.(BO_{1.5})_x$

5.3.3 B doped $La_8Y_2Ge_6O_{27}$

The Powder X-ray diffraction data, Figure 5.10, indicated all samples were present as a hexagonal apatite phase. The $La_8Y_2Ge_6O_{27}$ was observed to have a small impurity peak at ~28^o whilst the borate samples were shown to be pure.

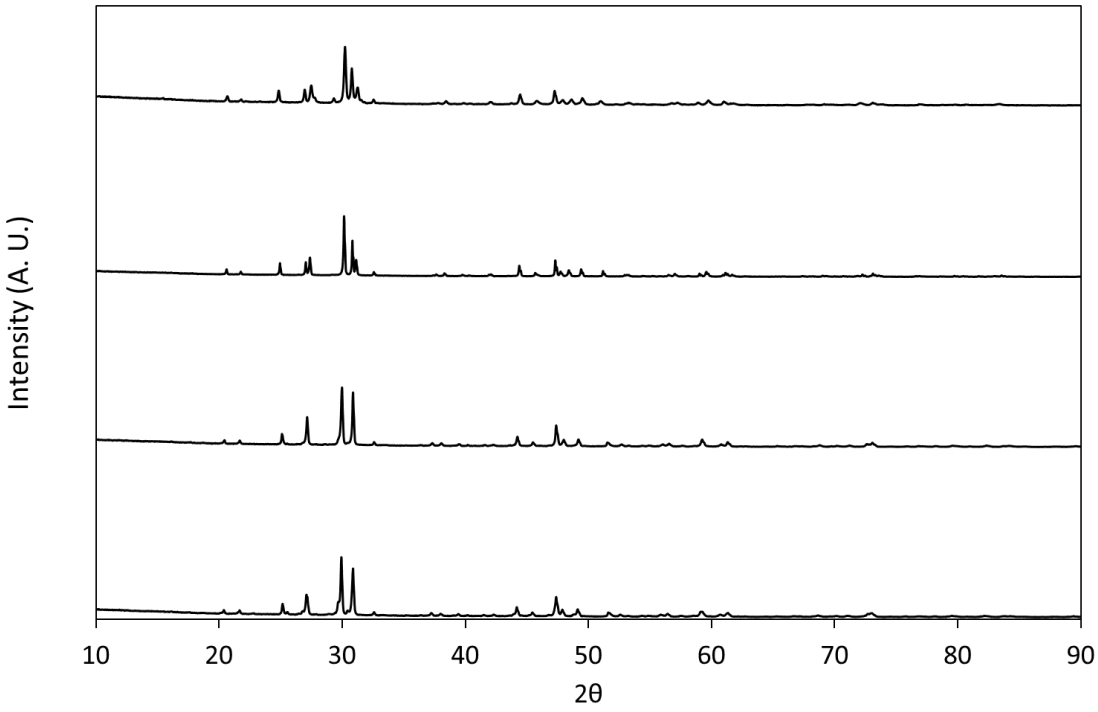

Figure 5.10: Powder X-ray Diffraction from to top to bottom: $La_8Y_2Ge_6O_{27,}$ $La_8Y_2Ge6O27(BO_{1.5})_{0.5}$, $La_8Y_2Ge_6O_{27}(BO_{1.5})_{1.0,}$ $La_8Y_2Ge_6O_{27}(BO_{1.5})_{1.5}$

Rietveld refinement was performed using the GSAS II suite of programs based on the space group *P/63m* apatite model using the collected powder X-ray diffraction data for the borate doped phases. The unit cell parameters and goodness of fit parameters as shown Table 5.3.

Table 5.3: Cell parameters and goodness of fit values for $La_8Y_2Ge_6O_{27}(BO_{1.5})_x$

X	**a (Å)**	**c (Å)**	**Unit Cell Parameters (Å^3)**	**$_w$Rp**	**Rp**	**χ_2**
0.5	9.9413(3)	7.1296(1)	610.21(8)	5.79	1.60	3.61
1.0	10.0267(7)	7.0790(0)	616.34(6)	6.83	1.59	4.30
1.5	10.0501(3)	7.0739(1)	618.77(6)	8.55	1.58	5.41

The cell volumes were found to show a small increase with the increase in borate content, similar to the $La_{10}Ge_6O_{27}$ series, although the overall values were lower than the later. Similar to the borate doped $La_{10}Ge_6O_{27}$ series, the a parameter was shown to expand while the c parameter contracted, consistent with extra O interstitial ions.

The unit cell parameters show an approximately positive linear trend between the unit cell volume and the borate concentration, as expected, Figure 7.10. This again confirms that borate has been successfully added to the structure.

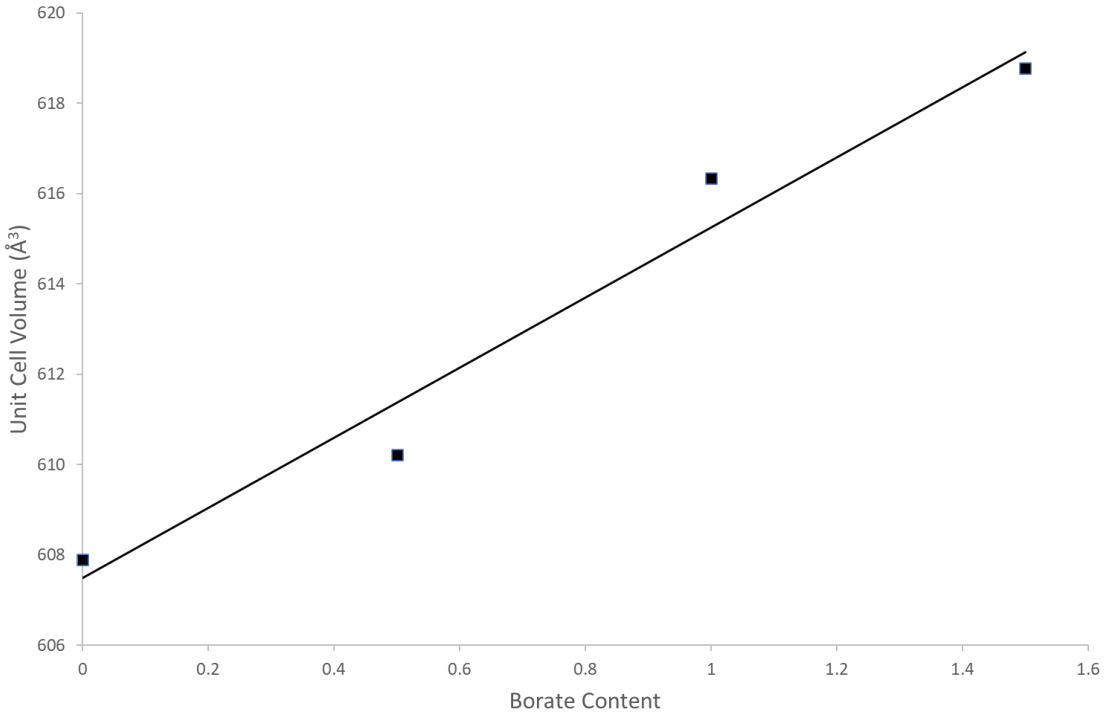

Figure 5.11: Unit Cell Volumes vs Borate content for $La_8Y_2Ge_6O_{27}(BO_{1.5})_x$

To demonstrate that the increase in cell volume is due to increasing borate content within the channels, the substitution of B^{3+} for Ge^{4+} was studied with the composition $La_8Y_2Ge_{5.5}B_{0.5}O_{26.75}$ prepared. This corresponds to B replacing Ge with no borate in the channels.

The Powder X-ray diffraction data, Figure 5.12 indicated that $La_8Y_2Ge_{5.5}B_{0.5}O_{26.75}$ stabilises as a hexagonal phase although there was a small impurity peak at ~28° similar to $La_8Y_2Ge_6O_{27}$.

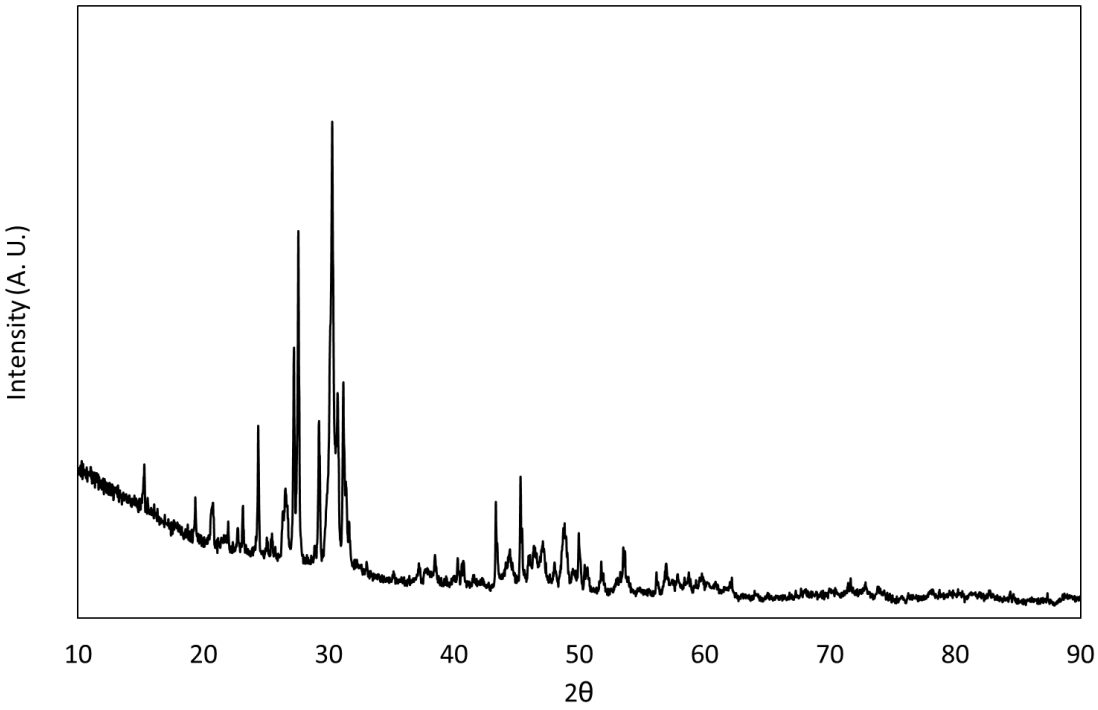

Figure 5.12: Powder X-ray Diffraction of $La_8Y_2Ge_{5.5}B_{0.5}O_{26.75}$

Rietveld refinement was performed using the GSAS II suite of programs based on the space group *P/63m* apatite model using the collected powder X-ray diffraction data for the substituted phase. The unit cell parameters and goodness of fit parameters was shown, Table 5.4.

Table 5.4: Cell parameters and goodness of fit values for $La_8Y_2Ge_{6-x}B_xO_{27-x/2}$

X	**a (Å)**	**c (Å)**	**Unit Cell Parameters (Å^3)**	**$_w$Rp**	**Rp**	**χ_2**
0	9.9015(0)	7.1563(5)	607.60(8)	5.82	2.59	2.25
0.5	9.7914(2)	7.2108(4)	598.69(8)	12.26	3.46	3.54

The lattice parameters were found to decrease with the substitution of germanium for boron for this sample. This is expected due to the replacement of the larger Ge^{4+} with the smaller B^{3+} atom. This therefore confirms that the increased cell parameters within $La_8Y_2Ge_6O_{27}(BO_{1.5})_x$ are due to the introduction of borate into the channels and not the substitution of germanium with boron.

IR spectra for the borate doped $La_8Y_2Ge_6O_{27}$ phases are shown in Figure 5.13. To examine the presence of the three key borate peaks at 900, 980, and 1300 cm^{-1}, Figure 5.13. For the undoped samples, the peaks do not appear in the spectrum; they then grow with increasing borate concentration. As before, the 1300 cm^{-1} peak is only seen for the higher dopant levels. This confirms the presence of BO_4^{5-} mainly with some BO_3^{3-} at higher levels.

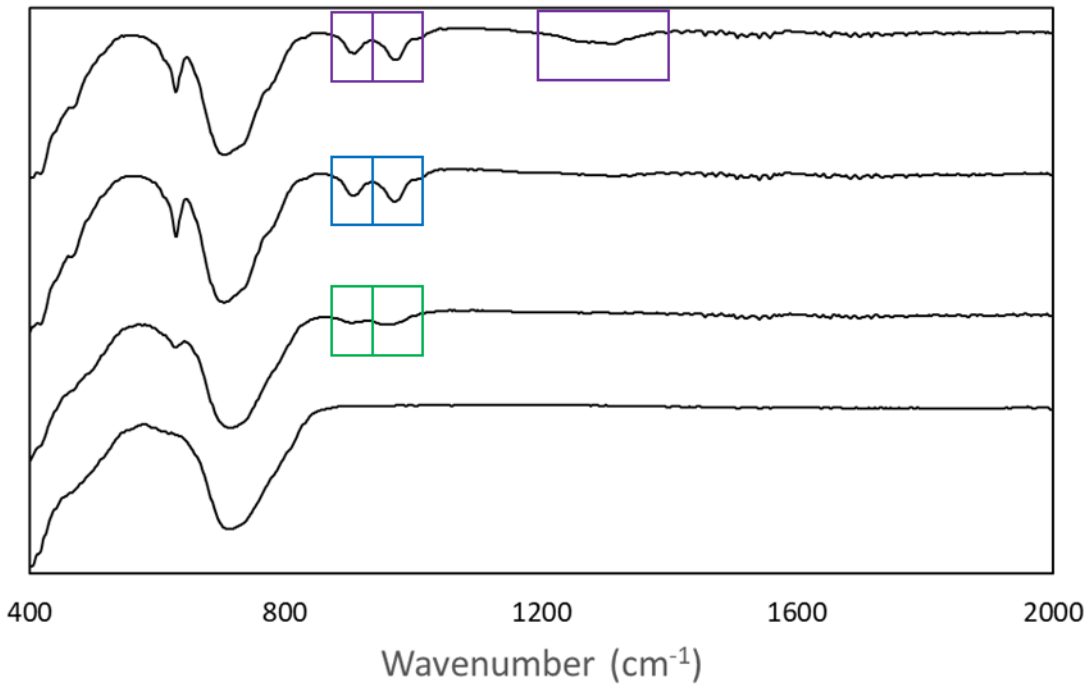

Figure 5.13 IR Spectra from top to bottom: $La_8Y_2Ge_6O_{27}(BO_{1.5})_{1.5}$, $La_8Y_2Ge_6O_{27}(BO_{1.5})_{1.0}$, $La_8Y_2Ge_6O_{27}(BO_{1.5})_{0.5}$ and $La_8Y_2Ge_6O_{27}$

The conductivity data in Figure 5.14, shows a clear trend between doping and conductivity. All the samples show a clear trend that as borate content increased, the conductivity is lowered. Thus for this system there is no conductivity increase on low level boron doping which is due to the fact that all samples are hexagonal and so there is no additional stabilisation effect from boron, due to yttrium stabilising the structure.

There is a significant drop in conductivity between $La_8Y_2Ge_6O_{27}(BO_{1.5})_{0.5}$ and $La_8Y_2Ge_6O_{27}(BO_{1.5})_{1.0,}$ suggesting the increase in borate concentration leads to blocking the central channel and so one of the conduction pathways. When comparing the two highest concentration of borate and $La_8Y_2Ge_6O_{27}(BO_{1.5})_{1.0,}$ $La_8Y_2Ge_6O_{27}(BO_{1.5})_{1.5}$, their conductivity was shown to similar, suggesting that the extra boron content does not limit the conduction mechanism perpendicular to the channel. When comparing to the $La_{10}Ge_6O_{27}$ doped series, the maximum conductivity is similar.

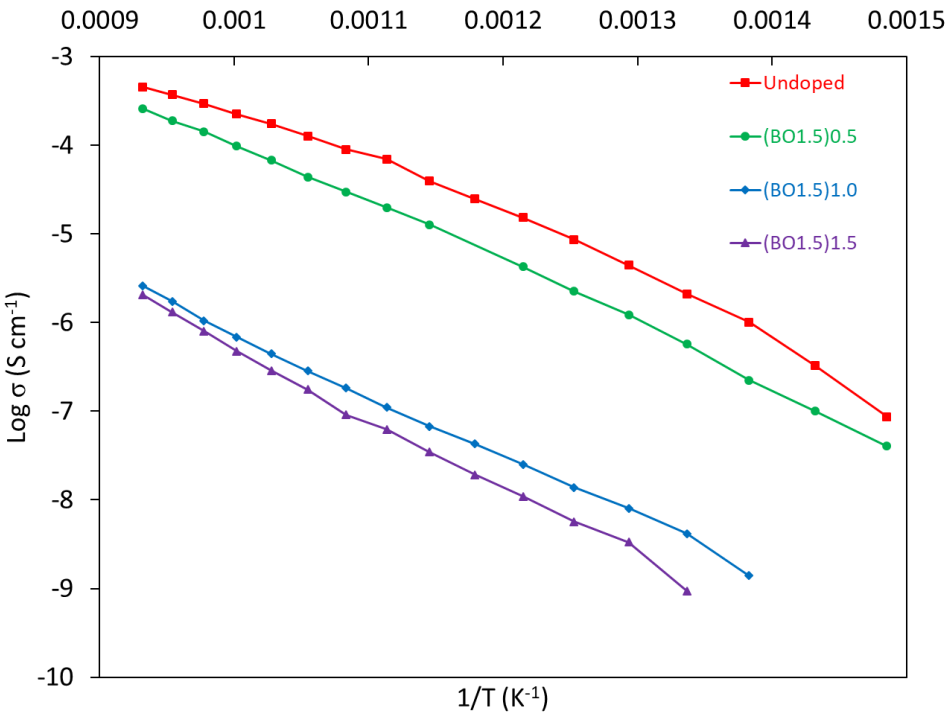

Figure 5.14: Plot of log σ versus 1/T for $La_8Y_2Ge_6O_{27}$ and $La_8Y_2Ge_6O_{27}(BO_{1.5})_x$

5.4 Conclusions

In this chapter, we have shown that borate can be incorporated within $La_{10-x}Y_xGe_6O_{27}$ (x = 0,1,2) resulting in the synthesis of new hexagonal apatite phases. The presence of this borate is confirmed by all IR spectra (peaks at ~900, 980 and 1300 cm^{-1}) showing peaks of increasing intensity with increasing borate concentration.

Conductivity measurements showed there was a general improvement for $La_{10}Ge_6O_{27}(BO_{1.5})_x$ materials for low levels of borate incorporation, with a decrease in conductivity with higher concentration of borate. The fact that significant oxide ion conductivities are observed despite the filling of the channels with borate provides supporting evidence for a secondary conduction pathway perpendicular to the central channel is as proposed by modelling studies. This work therefore provides experimental validation for these prior modelling predictions.

5.5 References

1. M. R. Ormerod, *Chem. Soc. Rev.,***32**, 17-28 (2003).

2. N. Q. Minh, *J. Am. Ceram. Soc.,***76**, 563-588 (1995).

3. E. D. Wachsman and K. Taek, *Science,* **334**, 935-939 (2011).

4. P. M. Panchmatia, A. Orera, G. J. Rees, M. E. Smith, J. V. Hanna, P. R. Slater and M. S. Islam, *Angew. Chem. Int. Ed,* **50**, 9328-9333 (2011).

5. E. Kendrick, M. S. Islam and P. R. Slater, *J. Mater. Chem.,* **17**, 3104-3111 (2007).

6. A.Najib, J. E. H. Sansom, J. R. Tolchard, P. R. Slater and M. S. Islam, *Dalton Trans.,* **19**, 3106-3109 (2004).

7. L. León-Reina, E. R. Losilla, M. Martínez-Lara, M. C. Martín-Sedeño, S. Bruque, P. Núnez, D. V. Sheptyakov and M. A. G. Aranda, *Chem. Mater.,* **17,** 596-600 (2005).

8. H. Yoshioka, *J. Alloys Compd.,***408**, 649-652 (2006).

9. K. Kobayashi, Y. Igarashi, N. Saito, T. Higuchi, Y. Sakka and T. S. Suzuki, *J. Ceram. Soc. Jpn.,* **126**, 91-98 (2018).

10. E. Kendrick and P. R. Slater, *Materials Research Bulletin,* **43**, 2509-2513 (2008).

11. M. S. Chambers, P. Chater, I. R. Evans and J. S. Evans, *Inorg. Chem.,* **58**, 14853-14862 (2019).

12. A. Orera, T. Baikie, P. Panchmatia, T. J. White, J. Hanna, M. E. Smith, M. S. Islam, E. Kendrick and P. R. Slater, *Fuel Cells,* **11**, 10-16 (2011).

13. E. Abram, C. Kirk, D. Sinclair and A. West, *Solid State Ion.,* 176, 1941-1947 (2005).

14. A. Orera and P. R. Slater, *Chem. Mater.,* **22**, 675-690 (2010).

15. K. Matsunaga, *J. Ceram. Soc. Jpn.,* **125**, 670-676 (2017).

16. C. A. Hancock, J. M. Porras-Vazquez, P. J. Keenan and P. R. Slater, *Dalton Trans.,* **44**, 10559-10569 (2015).

17. S. Ide, H. Takahashi, I. Yashima, K. Suematsu, K. Watanabe and K. Shimanoe, *J. Phys. Chem. C,* 124, 2879-2885, (2020).

18. A. Jarvis, P. Slater, *Crystals,* 7, 169, (2017).

19. Smith, M. James, P. Slater, *ECS Trans,* **91**,1425-1436 (2019).

20. A. Kodaira, H. F. Brito and M. C. F. C. Felinto, *J. Solid State Chem.,***171**, 401-407 (2003).

21. A. Kodaira, H. F. Brito, O. L. Malta and O. A. Serra, *J. Lumin.,* **101**, 11-21, (2003).

22. M. Kakihana and T. Okubo, *J. Alloys Compd.,* **266**, 129-133 (1998).

23. B. H Toby, R. B. Von Dreele, *J. Appl. Crystallogr,* **46***,* 544-549 (2013).

Chapter 6: Synthesis and characterisation of $SrFe_{1-x}S_xO_{3-\delta}$, via carrageenan-route synthesis

6.1 Introduction

Sol-gel, a broad descriptor of synthesis to form metal oxides from solution state precursors has become increasingly important as a mixed metal oxide synthesis route due to lower synthesis temperature and shorter synthesis time. (1-4) One of the characteristics of such sol-gel synthesis routes is the use of a variety of gelation (also known as chelating) ligands to form a covalent polymer network to entrap metal ions. One particular eponymous method is named after the original patent holder, Pechini, who used citric acid and ethylene glycol in his process to form a metal/organic gel. (5) Successful synthesis has also been conducted with other polymers and biopolymers such as polyvinyl alcohol (PVA), polyethylene glycol (PEG), polyvinylpyrrolidone (PVP), Starch, Dextran, Chitin, Alginate and Gelatin. (6-24)

Another biopolymer of potential use as a gelation agent is the Carrageenan family, extracted from red seaweed. One of its differentials to other biopolymers is its sulfonated functional side groups.

Oxyanion doping of mixed metal oxides has become an increasingly used strategy to influence the structure and physical properties and as with other anion dopants stands as an alternative to traditional doping strategies i.e doping with aliovalent cations. (25-29)

Over the last three decades the optimisation of cuprate superconductors for higher T_c led to studies showing that such materials have a great propensity to accommodate carbonate (CO_3^{2-}), with the substitution of Cu for C on the B cation with the oxide ions filling 3 of the 6 available anion sites surrounding the B site. (30-35) With further developments, other oxyanions (Borate, Nitrate, Phosphate, Sulphate, Silicate) have been shown to be used as

dopants in a wide variety of structures, such as Perovskites, Rudddlesden-Popper phases, and Apatite. (36-43)

One technology already studied for oxyanion doping strategies are materials for Solid Oxide Fuel Cell application (SOFC's). (44-52) However, due to their high operating temperature, more thermally stable oxyanion species are examined. One such species, sulphates (SO_4^{2-}), was first reported as a dopant to stabilise $YSr_2Cu_3O_y$ and $YSr_{2-x}Ca_xCu_3O_y$ as superconducting materials and has also been shown to introduce oxide ion vacancy disorder into perovskites with potential application as a cathode material. (53-55)

One such material, $SrFeO_{3-\delta}$, has attracted interest due to its low cost and high ionic and electronic conductivity, however under low $p(O_2)$, transforms into an oxygen vacancy ordered brownmillerite structure, $Sr_2Fe_2O_5$. However, work by Jarvis et al showed that low level incorporation of sulphate led to a stable perovskite phase, even at low $p(O_2)$ with a small increase in electronic conductivity. (56) Jarvis et al also note the loss of CO_2 when $SrFe_{1-x}S_xO_{3-\delta}$ samples were heated under N_2, suggesting that carbonate is also present within these materials i.e $SrFe_{1-x-y}S_xC_yO_{3-\delta}$. Computational studies of $SrFeO_3$ phases have also indicated favourable water and carbon dioxide incorporation. (57-59)

However, issues with the larger scale manufacture of $SrFe_{1-x}S_xO_{3-\delta}$, and other oxyanion materials is the limitation of the solid-state synthesis route used, usually requiring high temperature (>1000 ^oC) and long dwell times (total synthesis of 48+ hours). This limitation could cause issues with sulphate loss.

Herein we report the first use of two forms of biopolymer, Iota and Kappa Carrageenan as both a gelation agent and a precursor material with a novel sol-gel synthesis for the

manufacture of $SrFe_{1-x}S_xO_{3-\delta}$ materials and compare the results with the standard high-temperature solid-state synthesis for potential applications as a SOFC cathode material.

6.2 Experimental

The synthesis of $SrFe_{1-x}S_xO_{3-\delta}$ (x = 0, 0.025, 0.050, 0.075 and 0.100) was performed by two methodologies: solid state and sol-gel.

Solid-state samples were prepared following the route from Jarvis et al. (56) A stoichiometric mixture of high purity $SrCO_3$, Fe_2O_3 and $(NH_4)_2SO_4$ was ground and heated to 900 ^oC (4 ^oC min^{-1}) for 12 hours. Samples were reheated to 1000, 1050 and 1100 ^oC for 12 hours with intermediate regrind between each heating stage.

Sol-gel samples were prepared by dissolving high purity $Sr(NO_3)_2$ and $Fe(NO_3)_3.9H_2O$ in water and heating on a hot plate with either Iota or Kappa Carrageenan (Citric Acid was used for $SrFeO_{3-\delta}$) and ethylene glycol added to the correct stoichiometric ratios. Once a gel formed, the samples were slowly heated to 350 ^oC (1 ^oC min^{-1}) to remove all organic products. These materials were then ground and further heated at 950 ^oC (4 ^oC min^{-1}) for 24 hours with an intermediate regrind.

Powder X-ray diffraction data were collected to determine lattice parameters and phase purity of samples. Data was collected on a Panalytical Empyrean diffractometer equipped with Pixcel 2D detector (Cu Kα radiation). The GSAS II suite of programs was used for structure refinements of these systems. (60)

Samples were analysed to determine iron oxidation states using thermogravimetric analysis (Netzch STA 449 F2 Jupiter Thermal Analyser). Samples were heated to 1000 °C (10 °C / min) in N_2 and held at this temperature for 30 minutes to reduce the iron oxidation states to +3, thus allowing the oxygen content and average iron oxidation to be determined.

^{57}Fe Mössbauer spectroscopy was carried out at 298 K in constant acceleration mode using approximately 25mCi Co/Rh source.

Pellets for conductivity measurements were prepared by ball-milling (350 rpm for 30 minutes) in a ZrO_2 container and balls before pressing samples into compacts and sintering at the highest synthesis temperature for 12 hours. Four Pt electrodes were attached with Pt paste and the samples were heated to 950 °C for 1 hour in air to ensure good contact. Samples were then cooled to 350 °C and held at this temperature for 12 hours to ensure the maximum oxygen content. Conductivities were then measured in air with varying temperatures using the four-probe DC method.

6.3 Results and Discussion

6.3.1 Structural Determination

The original solid-state synthesis route outlined by Jarvis et al previously involves the use of a conventional solid-state synthesis route with $(NH_4)_2SO_4$ as the sulphate-dopant. The $SrFe_{1-x}S_xO_{3-\delta}$ samples were successfully prepared, but required 4 heat treatments, with the largest dwell temperature of 1100 ^{o}C and a total time of heating of around 60 hours. The sol-gel synthesis route reported in this work requires only 3 heat treatments in an oven/furnace and reduces the highest dwell temperature by 150 ^{o}C and around 24 hours of heating time.

Two variants of carrageenan (Iota and Kappa or I and K) were assessed for their ability to form the $SrFe_{0.95}S_{0.05}O_{3-\delta}$ material via the novel sol-gel synthesis route. Figure 6.1 shows the Powder X-ray diffraction of both samples compared to the solid-state variant.

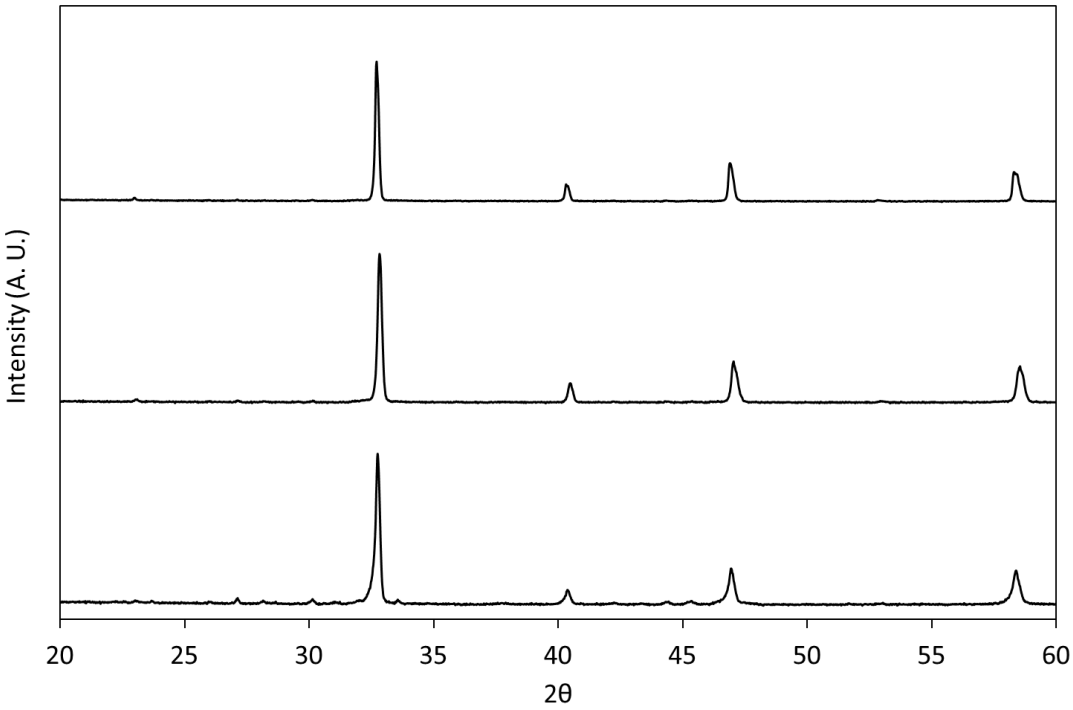

Figure 6.1 Powder X-ray diffraction patterns of $SrFe_{0.95}S_{0.05}O_{3-\delta}$ from top to bottom: solid-state synthesis, sol-gel/I-Carrageenan synthesis, sol-gel/K- Carrageenan synthesis. $SrSO_4$ impurities are observed for sol-gel/K- Carrageenan synthesis (highlighted inside the rectangle)

Upon doping with two forms of carrageenan, I-Carrageenan was shown to form a cubic cell that matches that of the solid-state route. K-Carrageenan was also shown to form a cubic cell, however, small $SrSO_4$ impurities appear, suggesting some issues with K-Carrageenan. Therefore, I-Carrageenan was chosen as the gelation agent/ sulphate precursor going forward.

A range of $SrFe_{1-x}S_xO_{3-\delta}$ with sulphate content (x = 0, 0.025, 0.05, 0.075 and 0.010) were prepared via this sol-gel method. The X-ray diffraction analysis shows the same results as Jarvis et al with a tetragonal perovskite forming within the undoped material and the transformation to a cubic cell with increasing sulphate content. This is illustrated in Figure 6.2. Small impurities were of $SrSO_4$ were shown to appear for x = 0.075, consistent with the solid-

state materials and suggesting a clear solubility limit of sulphate in $SrFe_{1-x}S_xO_{3-\delta}$ within both methods.

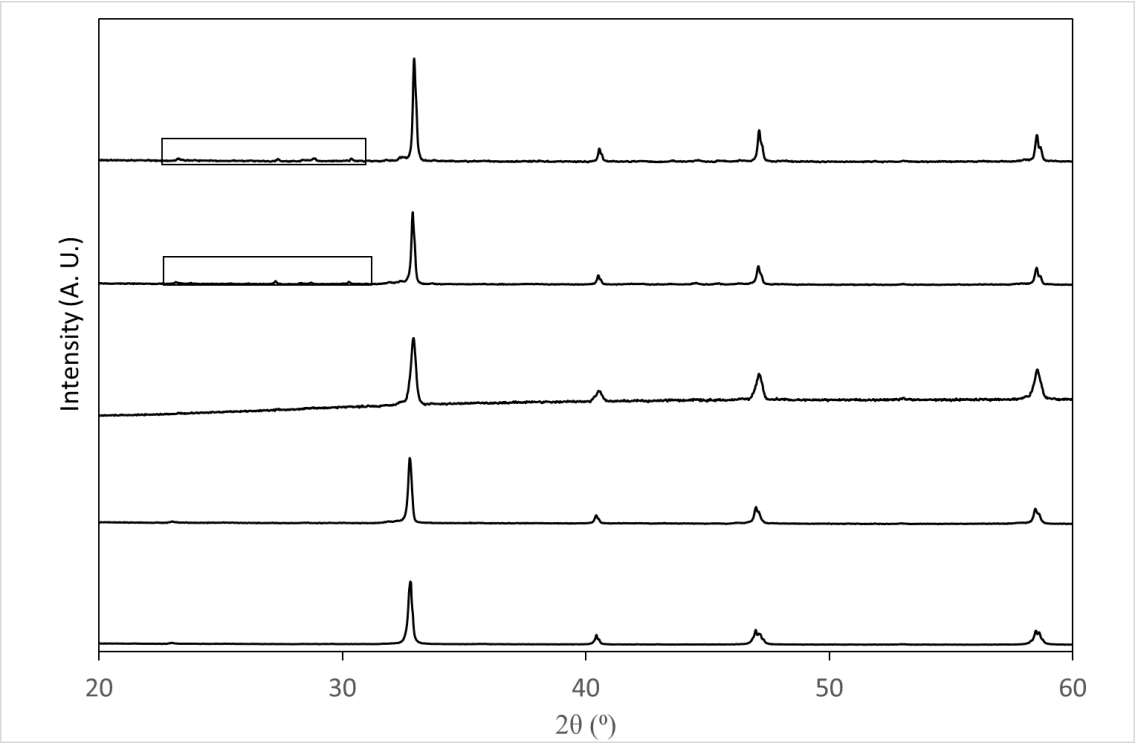

Figure 6.2 Powder X-ray diffraction of sol-gel synthesis using I-carrageenan as gelation/sulphate precursor, from bottom to top: $SrFeO_{3-\delta}$, $SrFe_{0.975}S_{0.025}O_{3-\delta}$, $SrFe_{0.95}S_{0.05}O_{3-\delta}$, $SrFe_{0.925}S_{0.075}O_{3-\delta}$ and $SrFe_{0.90}S_{0.10}O_{3-\delta}$. The data shows with the formation of a tetragonal cell for $SrFeO_{3-\delta}$ whilst the sulphate-doped samples are cubic. $SrSO_4$ impurities are observed for x = 0.075 and x = 0.010 samples (highlighted inside the rectangles).

Thermogravimetric analysis (TGA) was undertaken to determine if carbonate is present in the samples as suggested previously by Jarvis et al, Figure 6.3.

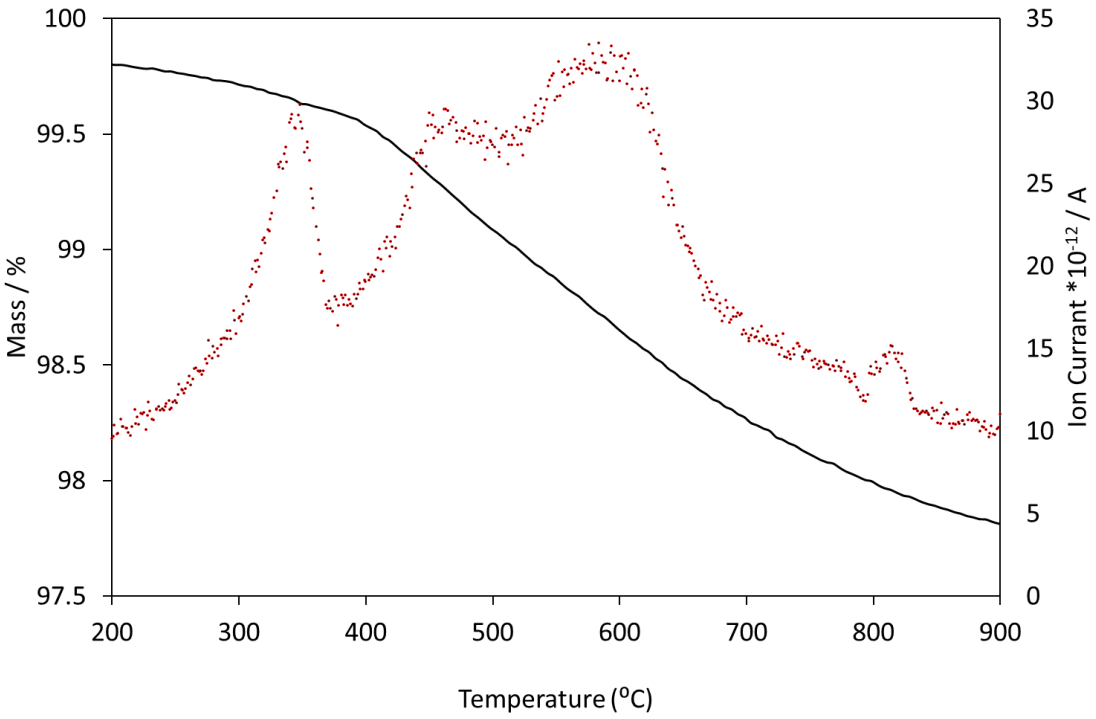

Figure 6.3: illustrates a dual-axis plot that tracks both mass (black line) and ion current (specifically for m/z = 44, corresponding to CO_2 as seen as red dots) as functions of temperature under a nitrogen (N_2) atmosphere for the compound $SrFe_{0.95}Fe_{0.05}O_{3-\delta}$.

The results indicate the presence of carbonate in $SrFe_{1-x}S_xO_{3-\delta,}$ with a greater amount than previously reported by Jarvis et al. We attribute this higher carbonate to the final lower synthesis temperature and the presence of significant carbon from the sol gel route. Therefore, we suggest that the material is a mixed sulphate/carbonate doped perovskite, $SrFe_{1-x-y}S_xC_yO_{3-\delta}$. Jarvis et al previously reported that carbonate may be removed via heat treatment in O_2 (up to 900 ^oC).

Upon increased doping of sulphate, there is an implied reduction in the average Fe site oxidation state. This partial reduction of Fe^{4+} to Fe^{3+} is likely due to two key factors.

1. Fe^{4+} being partially replaced by higher concentrations of higher valent S^{6+}

2. The increased conversion of coordination to tetrahedral (as required for SO_4^{2-}) due to the increased oxygen vacancies leading to a partial reduction of Fe.

To further understand the Fe environments, ^{57}Fe Mössbauer spectroscopy was carried out at 298 K on $SrFe_{0.95}S_{0.05}O_{3-\delta}$ made via two routes; solid-state and sol-gel the with use of I-Carrageenan.

Previous studies have shown that undoped $SrFeO_{3-\delta}$ contains $Fe^{3.5+}$ and Fe^{4+} whilst doping strategies of Si^{4+} and Sn^{4+} on $SrFeO_{3-\delta}$, showed disproportionation of the Fe^{4+} to Fe^{3+} and Fe^{5+}.

Chemical isomers of δ = -0.19, 0.13/0.18, 0.28/0.31 and 0.46/0.48 mm s^{-1} can be assigned Fe^{5+}, $Fe^{3.5+}$, Fe^{3+} and Ionic Fe^{3+} respectively (Figure 6.4 and Table 6.1). The measurements confirm that disproportionation of Fe^{4+} to Fe^{3+} and Fe^{5+} does indeed occur upon sulphate doping which correlates with previous oxyanion doping studies of $SrFeO_{3-\delta}$.

Furthermore, measurements showed that both samples contain the same Fe environments and the same quantities (within the margin of error). This suggests that there is negligible difference between the two synthesis routes with regards to Fe oxidation states.

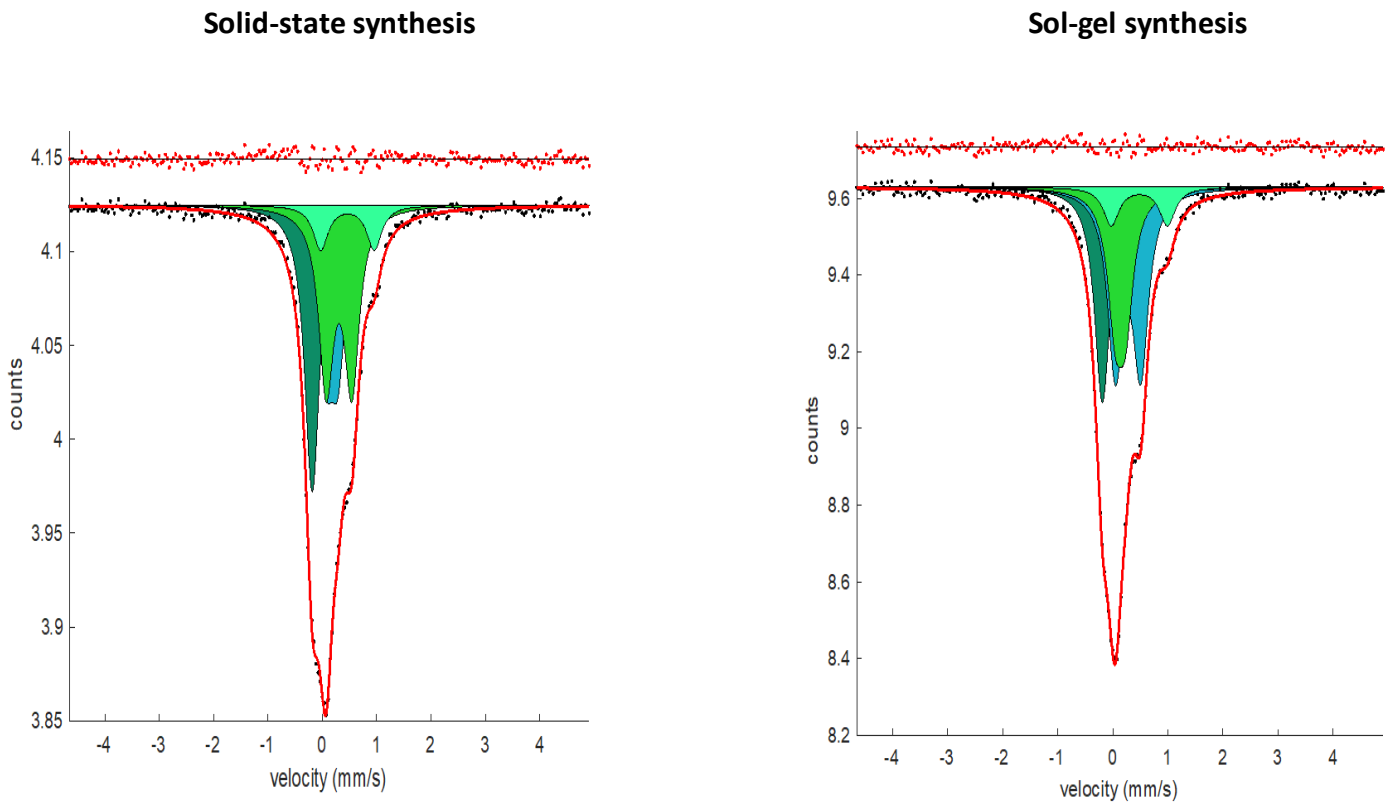

Figure 6.4 ^{57}Fe Mössbauer Spectroscopy for $SrFe_{0.95}S_{0.05}O_{3-\delta}$ samples, left: Solid state synthesis and right: Sol-gel/ Iota-Carrageenan synthesis

TABLE 6.1 ^{57}Fe Mössbauer Spectroscopy data for $SrFe_{0.95}S_{0.05}O_{6-\delta}$ for solid state synthesis

Compound	**Assignment**	**δ (mms^{-1})**	**Δ (mms^{-1})**	**Area ± 5% (%)**
Solid-state synthesis	Ionic Fe^{3+}	0.46	0.99	9
	Fe^{3+}	0.31	0.47	35
	$Fe^{3.5+}$	0.18	0.22	28
	Fe^{5+}	-0.19	---	28
Sol-gel / Iota-Carrageenan Synthesis	Ionic Fe^{3+}	0.48	1.02	9
	Fe^{3+}	0.28	0.46	40
	$Fe^{3.5+}$	0.13	0.19	26
	Fe^{5+}	-0.19	---	24

Cell parameters for the range of I-Carrageenan synthesised $SrFe_{1-x}S_xO_{3-\delta}$ (0.025, 0.050 and 0.075) were determined using the Rietveld refinement (space group *P m -3 m* perovskite model), performed using the GSAS-II suite of programs. The unit cell parameters from the refinements are shown in Table 6.2

TABLE 6.2. Cell parameters and goodness of fit values for I-Carrageenan synthesised $SrFe_{1-x}S_xO_{3-\delta}$ and Solid state $SrFe_{1-x}S_xO_{3-\delta}$ comparison.

x	**a (Å) I-Carrageenan**	**$_wRp$**	**Rp**	**χ^2**	**a (Å) Solid-State samples (56)**
0.025	3.8659(7)	3.82	2.34	1.63	3.8641(1)
0.050	3.8724(4)	4.80	2.42	1.98	3.8692(1)
0.075	3.8766(9)	4.08	2.87	1.42	3.8691(1)

The lattice parameters were shown to increase with the incorporation of sulphate. This observed increase in volume may be attributed to the replacement of smaller Fe^{4+} ions by larger Fe^{3+} ions upon further sulphate doping.

On comparison of the cell parameters of the I-carrageenan synthesised $SrFe_{1-x}S_xO_{3-\delta}$ with the solid-state variant of Jarvis et al, the newly synthesised materials have a slightly larger lattice parameter. This variation may be due to the higher solubility of carbonates at lower temperatures and thus a slightly increased volume. Although we cannot rule out small deviations from the ideal stoichiometry of sulphate content, the general conclusion drawn in this work is that sulphate has been doped within the structure.

6.3.2 Conductivity measurements

In the solid-state synthesised samples, Jarvis et al reported similar conductivities at low dopant levels (below x = 0.075) with higher sulfate content decreasing conductivity, due to disruption of the Fe-O network and low levels of an insulating impurity, $SrSO_4$.

When comparing to solid-state synthesis samples, Table 6.3, the Iota carrageenan synthesised samples have decreased conductivities. One explanation of this decrease may be due to the higher report value of carbonate incorporation into the structure than Jarvis et al.

Table 6.3 The conductivity of I-Carrageenan synthesised $SrFe_{1-x}S_xO_{3-\delta}$ and Solid-state $SrFe_{1-x}S_xO_{3-\delta}$ comparison at 700 ^oC in air.

	σ I-Carrageenan synthesis route (S cm ^{1})	**σ Solid-state synthesis route (S cm ^{1})**
$SrFe_{0.975}S_{0.025}O_{3-\delta}$	6.29	17.80
$SrFe_{0.95}S_{0.05}O_{3-\delta}$	6.84	14.35
$SrFe_{0.925}S_{0.075}O_{3-\delta}$	6.41	14.25

Computational studies of carbon dioxide incorporation in $SrFeO_3$ phases suggest that carbonate may be thermally stable to incorporate and is likely to significantly disrupt the conductivity thus it suggests that the higher carbonate content in Iota carrageenan samples has a detrimental effect on the conductivity. (57-59)

6.4 Conclusions

The use of Iota and Kappa Carrageenan as both a gelation agent and sulphur dopant allowed for the formation of a range of $SrFe_{1-x}S_xO_{3-\delta}$ materials at a lower temperature and shorter time. The ^{57}Fe Mossbauer Spectroscopy suggest that both solid-state and sol-gel synthesised materials had similar Fe environments and lattice parameters followed similar trends upon further doping.

However, there was significantly more carbonate reported in carrageenan synthesised samples than previously reported solid-state route which presumably may be the reason for the reduced the electrical conductivity of the material.

This work further highlights previous literature on the potential incorporation of carbonate in perovskite materials when synthesis temperature is below 1100 ^oC and the fact that gelation agents in sol-gel synthesis are not necessarily inert with respect to the final product. Care should be particularly taken when assessing low-temperature routes for perovskite systems and their potential effects of carbonate on physical properties such as mixed ionic and electronic conductivity.

The work suggests that with the use of biopolymers as gelation/precursor materials may allow for the development of new oxyanion doped perovskite systems. There are also wider implications that may lead to other mixed metal-sulphate containing materials being researched for potential synthesis using Carrageenan or other biopolymers.

6.5 References

1. A. E. Danks, S. R. Hall and Z. Schnepp, *Mater. Horiz.,* **3,** 91-112 (2016)
2. K. Deshmukh, T. Kovářík, T. Křenek, D. Docheva, T. Stich and J. Pola, *RSC Adv.,* **10,** , 33782-33835 **(**2020)
3. L. L. Hench and J. K. West, *Chem. Rev.,* **1,** 33-72 (1990)
4. M. Parashar, V.K Shukla, R. Singh, *J. Mater. Sci.: Mater. Electron.,* **31,** 3729-2749 ***(***2020)
5. M. Pechini, *US Patent,* 3330697A, (1967)
6. S. R. Hall, *Adv. Mater.,* **18,** 487-490 (2009)
7. K. Hayat, M. A. Gondal, M. M. Khaled, S. Ahmed and A. M. Shemsi, *Appl. Catal.,***393,** 122-129 (2011)
8. Y.-K. Sun and L.-H. Oh, *Ind. Eng. Chem. Res.,* **35,** 4296-4300, (1996)
9. T. Liu, Y. Xu and J. Zhao, J. Am. Ceram. Soc., **93,** 3637-3641 (2010)
10. S. R. Lukić, D. M. Petrović, M. D. Dramićanin, M. Mitrić and L. Daćanin, *Scr. Mater.,* **58,** 655-658, (2008)
11. S. Kandhasamy, A. Pandey and M. Minakshi, *Electrochim. Acta,* **60.** 170-176 (2012)
12. A. I. Martin, A. J. Salinas and M. Vallet-Regi, *J. Eur. Ceram. Soc.,* **25,** 3533-3538 (2005)
13. Y. Li, B. P. Bastakoti and Y. Yamauchi, *Chem- Eur. J., **21,*** 8038-8042 (2015)
14. D. C Fletcher, R. Hunter, W. Xia, G. J. Smales, B. R. Pauw, E. Blackburn, A. Kulak, X. HUolin and Z. Schnepp, *J. Mater. Chem. A.,* **7,** 19506-19512 (2019)
15. R. Luque, J. H. Clark, K. Yoshida and P. L. Gai, *Chem. Commun.,* 5305-5307 (2009)

16. V. Raman. O. P. Bahl and U. Dhawan, *J. Mater. Sci.,* **30,** 2686-2693 (1995)

17. R. Boston, A. Carrington, D. Walsh and S.R. Hall, *CrystEngComm,* **15,** 3763-3766 (2013)

18. Z. Schnepp, S. C. Wimbush, S. Mann and S. R. Hall, *Adv. Mater.,* **20,** 1782-1786 (2008)

19. Z. Schnepp, S. C. Wimbush, S. Mann and S. R. Hall, *CryslEngComm,* **12,** 1410-1415 (2010)

20. E. J. Lee, S. H. Jun. H. E. Kim, H. W. Kim, Y. H. Koh and J. H. Jang, *J. Mater. Sci.: Mater. Med.,* **21,** 207-214 (2010)

21. E. J. Lee, D. S. Shin, H. E. Kim, H. W. Kim, Y. H. Koh and J. H.Wang, *Biomaterials,* **30,** 743-750, (2009)

22. M. S. Chambers, D. S. Keeble, D. Fletcher, J. A. Hriljac, Z. Schnepp, *Inorg. Chem.,* **60** 7062-7069 (2021)

23. J. Zhou, F. Zhao, X. Wang, Z. Li, Y. Zhang and L.Yang, *Chem. Mater.,* **22,** 5340-5344 (2006)

24. K. Zheng, J. A. Bortuzzo, Y. Liu, W. Li, M. Pischetsrieder, J. Roether, M. Lu and A. R. Boccaccini, *J. Non-Cryst. Solids,* **354,** 825-832 (2015)

25. E. Smith, Z. Schnepp, S. C. Wimbush and S. R. Hall, *Physica C Supercond,* **468,** 2283-2287 (2008)

26. M. Iijima, M. Takahashi, T. Hatakeyama, H. Hatakeyama, *J. Therm. Anal. Calorim.,* **114,** 895-901 (2013)

27. K. S. Hossain, K Miyanaga, H Maeda, N Nemoto, *Biomarcomolecules,* **2,** 442-449 (2001)

28. V. M. F. Lai, P. A.-L. Wong, C.-Y. Lii, *J. Food Sci,* **65,** 1332-1337, (2006)

29. S. Kera, E. Arda and Ö. Pekcan, *Phase. Transit.,* **78,** 915-926 (2005)

30. H. G. Vonschnering, L. Walz, M. Shwarz, W. Becker, M. Hartweg, T. Popp, P. Hettich, P. Muller and G. Kampf, Angew. Chem., Int. Ed. Engl., **27,** 574, **(**1988)

31. T. G. N. Babu, D. J. Fish and C. Greaves, *J. Mater Chem.,* **1,** 677, (1991)

32. K. Kinoshita and T. Yamada, *Nature,* **357,** 313 (1992)

33. M. G. Francesconi and C. Greaves, *Supercond. Sci, Technol.,* **10,** A29 (1997)

34. M. Uehara, H. Nakata and J. Akimitsu, *Physica C,* **216,** 453 (1993)

35. J. Deakin, I. Trussov, A. Gibbs, E. Kendrick and P. R. Slater, *Dalton Trans.,* **47,** 12901-12906 (2018)

36. J. F. Shin, D. C. Apperley and P. R. Slater, *Chem. Mater.,* **22,** 5945 (2010)

37. J. F. Shin and P. R. Slater, *J. Power Sources,* **196,** 8539, (2011)

38. C. A Hancock and P. R. Slater, *Dalton Trans.,* **40,** 5599 (2011)

39. A. D. Smith, M. S. James and P. R. Slater, *ECS Trans.,* **91,** 1425-1436 (2019)

40. M. S. James, F. J. Berry, J. F. Marco and P. R. Slater, *ECS Trans,* **103,** 2185 (2021)

41. A. Jarvis, F. J. Berry, J. F. Marco and P. R. Slater, *ECS Trans,* **91,** 1467-1476 (2019)

42. A. Jarvis, F. J. Berry. J. F. Marco, M. Sanchez-Arenillas, G. Cibin, O. Clemens and P.R. Slater, *J. Solid. State. Chem.,* **287,** 121372 (2020)

43. S. W. Thomas, M. S. James, M. P. Stockham, J. Deakin, A. Jarvis and P. R. Slater, *ECS Trans.,* **103,** 1885-1897 (2021)

44. A. Orera and P. R. Slater, *Chem. Mater.,* **22,** 675 (2010)

45. J. F. Shin , A. Orera, D. C. Apperley and P. R. Slater, *J. Mater. Chem.,* **21,** 874, (2011)

46. J. F. Shin, K. Joubel, D. C. Apperley and P. R. Slater, *Dalton Trans.,* **41,** 261, (2012)

47. A. D. Smith, J. F. Shin and P. R. Slater, *J. Solid State Chem.,* **198,** 247 (2013)

48. C. A. Hancock, R. C. T. Slade, J. R. Varcoe and P. R. Slater, *J. Solid State Chem.,* **184,** 2972 (2011)

49. J. M. Porras-Vazquez, E. R. Losilla, P. J. Keenan, C. A. Hancock, T. F. Kemp, J. V. Hanna and P. R. Slater, *Dalton Trans,* **42**, 5421 (2013)

50. J. M. Porras-Vazquez, T. F. Kemp, J. V. Hanna and P. R. Slater, *J. Mater. Chem.,* **22,** 8287 (2012)

51. J. M. Porras-Vazquez and P. R. Slater, *Fuel Cells,* **12,** 1056, (2012)

52. J. M. Porras-Vazquez, T. Pike, C. A. Hancock, J. F. Marco, F. J Berry and P. R. Slater, *J. Mater. Chem. A.,* **1,** 11834 (2013)

53. Y. M Yarmoshenko, M. A. Korotin, V. A. Trofimova, V. R. Galakhov, L. V. Elokhina, E. Z. Kurmaec, S. Uhlenbrock, M. Neumann, P. R. Slater and C. Greaves, *Phys. Rev. B.,* **52,** 11830 (1995)

54. P. R. Slater, C. Greaves, M. Slaski, C. M. Muirhead,, *Physica C: Supercond.,* **208.** 193-196 (1993)

55. P. R. Slater, C. Greaves, M. Slaski, C. M. Muirhead, *Physica C: Supercond.,* **213.** 14-16 (1993)

56. A. Jarvis and P. R. Slater, *Crystals,* **7,** 169 (2017)

57. L. J. Ford, P. R. Slater, J. K. Christie, P. Goddard, *Phys. Chem. Chem. Phys.,* **22,** 25146, (2020)

58. K. Yamaura, Q.Huang, J. Lynn, R. Erwin, R. J. Cava, *J. Solid State Chem.,* **152,** 374-380, (2000)

59. Y. Bréard, C. Michel, M. Hervieu and B. Raveau, *J. Mater Chem.,* **10,** 1043-1045 (2000)

60. B. H. Toby, R. B. Von Dreele, *J. Appl. Chem.,* **46**(2), 544-549 (2013)

61. Y. Chin. X. Nie, B. Wang, C. Xia, W. Dong, X. Wang. H. Wang and B. Zhu, *Catal. Today.,* **355,** 295-303 (2020)

Chapter 7: Synthesis and characterisation of fluorine doped $Sr_{2-x}La_xCoO_{4-\delta}$

7.1 Introduction

Interest in fluorination of mixed metal oxides has been increasing with focus on tailoring physical properties such as electronic, optical and magnetic for a range of potential technological applications. The formation of mixed metal oxyfluorides potentially allows for fine control of such properties, by modifying transition metals oxidation states. (1-3).

However, such materials cannot usually be synthesised from metal fluoride and metal oxides starting materials due to the products lower thermodynamically stability than the starting materials. Therefore, a variety of fluorination agents e.g F_2, NH_4F, XeF_2 and PVDF have been previously used to incorporate fluorine into a mixed metal oxide, however, there are disadvantages to each fluorination method. (4-10)

Ruddlesden Popper-phases $A_{n+1}M_nX_{3n+1}$ (A = Alkaline earth or Lanthanum series, M = Tranistion metal and X = N, O or Halides), a group of layered perovskites have been widely reported as being successfully synthesised with mixed O/F occupation, especially n = 1 materials corresponding to the well-known K_2NiF_4 structures. Examples such as $Sr_2CuO_2F_{2+\delta}$ and Sr_2FeO_3F and $LaSrMnO_4F$ have been extensively studied, mainly for study for superconductivity or magnetism. Such materials seem to report a range of anion distribution patterns, with oxygen/fluorine sites either randomly distributed or ordered. (3, 11-13)

Cobalt-based oxyfluorides have been far less studied with limited literature on layered cobalt oxyfluoride materials. Sr_2CoO_3F was first reported by Tsujimoto et al to adopt a K_2NiF_4-type structure and showed an interesting phenomenon of the coexistence of anion disorder

between O and F at the apical sites. (14) However, the synthesis of such material with precursors SrO_2, SrF_2 and Co_3O_4 was only possible under high pressure and temperature.

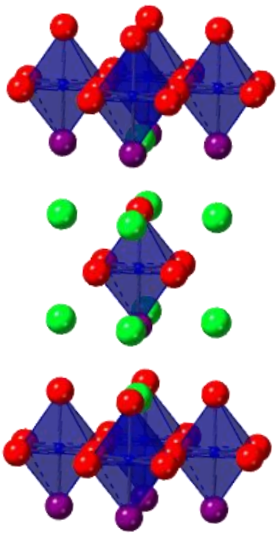

Figure 7.1. Sr_2CoO_3F crystal structure.

One potential route to allow successful synthesis at lower pressure and temperature would be to look at cation doping strategies, either on the Sr and/or Co site. One such method that is presented within this work is the use of a substituting low levels of La on the Sr site. (15)

K_2NiF_4 phases have also been attracting interest research for their potential within electrochemical devices. Most notably, their good electronic properties in addition to ability to introduce interstitial oxide anions allowing for fast oxygen ion conductivity to occur means there a generated significant interest for their use as electrode materials within Solid Oxide Fuel Cells (SOFC's) such as $La_2NiO_{4+\delta}$, $La_{2-x}NiO_{4+\delta}$, $La_2Ni_{0.6}Cu_{0.4}O_{4+\delta}$ and $La_{2-x}Sr_xCoO_{4+\delta}$. (16-21) Furthermore, K_2NiF_4 phases have recently been of interest as intercalation/deintercalation electrodes within Fluorine Ion Batteries (FIB's) with compounds such as $LaSrMnO_4$, La_2CoO_4 and $SrTiO_3F_2$ previous researched. (22-27)

Herein, we report the successful synthesis of a range of K_2NiF_4 structured La doped Sr_2CoO_3F phases under ambient pressure and demonstrate without fluorine (via SrF_2 fluorination agent) that such a material is not formed. We also evaluate these materials for their potential applications as SOFC cathode/ FIB electrode materials via conductivity and thermal characterisation.

7.2 Experimental

High purity $SrCO_3$, La_2O_3, SrF_2 and Co_3O_4 were used to prepare a range of $Sr_{2-x}La_xCoO_{4-y}F_y$ materials. These starting materials were ground together in the correct stoichiometric ratios and then heated to 950 °C (5 $^oC\ min^{-1}$) and 1050 °C (5 $^oC\ min^{-1}$) for 12 hours respectively, with an intermediate regrinding. A small excess of 10% Sr was added to overcome volatility. To ensure maximum oxygen content, the resulting samples were held at 350 °C for 12 hours in air.

Powder X-ray diffraction experiments, collected on a Panalytical Empyrean diffractometer (Cu Kα radiation) equipped Pixcel 2D detector, were used to determine phase purity and lattice parameters of samples. The GSAS II suite of programs was used to determine unit cell parameters of these systems. (28)

Pellets for thermal expansion measurements were prepared by ball milling samples for 30 minutes with small amounts of hexane than pressed into circular pellets and heated at 1100 °C in air 12 hours. C_{TE} was determined by a dilatometer (Netzsch DIL 402C) from 110 to 900 ^oC using Al_2O_3 as a reference with heating rate of 5 $^oC\ min^{-1}$ in air.

Conductivity measurements were obtained by preparing pellets as described above. Four Pt electrodes were attached to pellets with Pt paste and the samples were heated at 900 °C for

1 hour in air and cooled to 350 °C and held at 12 hours for maximum oxygenation. Conductivities were measured in air using the four probe DC method.

7.3 Results and Discussion

7.3.1 Structural Characterisation

Powder XRD patterns were collected on $Sr_{2-x}La_xCoO_{4-y}F_y$ compositions for x/y = (0.2/0.7, 0.3/0.6, 0.4/0.5, 0.5/0.4 and 0.6/0.3. These samples were the optimised amount of fluorine, as increasing fluorine caused impurity phases such as SrF_2 to be present. All patterns confirmed the formation K_2NiF_4 (*I 4 / m m m)* type phase, Figure II, with small peak shift noted on the increasing introduction of La.

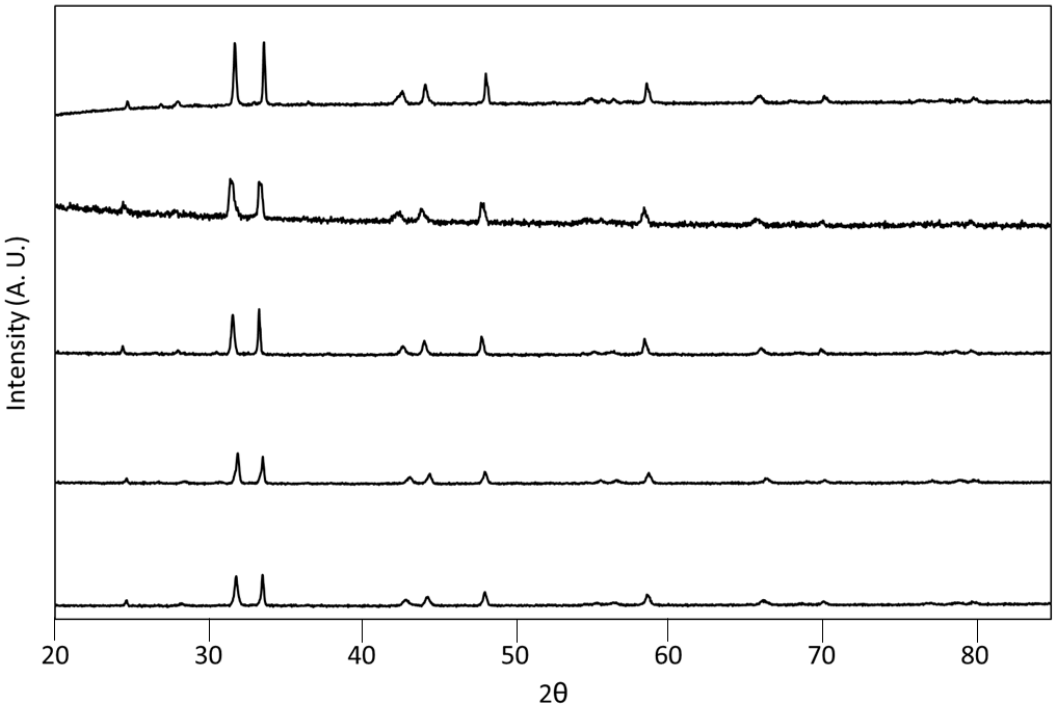

Figure 7.2 Powder X-ray diffraction patterns showing successful formation of the K_2NiF_4 type phase. From top to bottom: $Sr_{1.8}La_{0.2}CoO_{4-\delta}F_{0.70}$, $Sr_{1.7}La_{0.3}CoO_{4-\delta}F_{0.60}$, $Sr_{1.6}La_{0.4}CoO_{4-\delta}F_{0.50}$, $Sr_{1.5}La_{0.5}CoO_{4-\delta}F_{0.40}$, $Sr_{1.4}La_{0.6}CoO_{4-\delta}F_{0.30}$

To highlight the importance of fluorine for the formation of single-phase K_2NiF_4 material, a non-fluorinated material, $Sr_{1.8}La_{0.2}CoO_{4-\delta}$ was synthesised under ambient pressure conditions, Figure 7.3. Whilst some K_2NiF_4 (*I 4 / m m m)* type phase (most likely $Sr_{2-x}La_xCoO_4$ with higher La content)was observed, this was not single-phase like the fluorinated materials with significant impurities present.

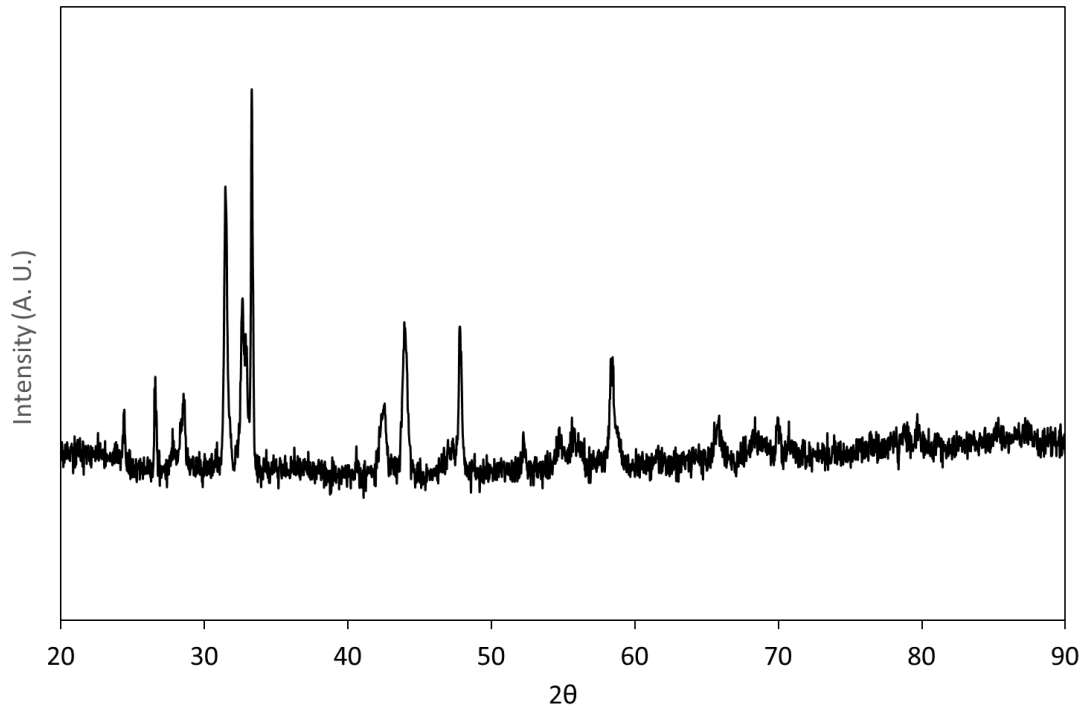

Figure 7.3. $Sr_{1.8}La_{0.2}CoO_4$ Powder X-ray diffraction pattern with $Sr_6(CoO_3)_5$ (*R 3 2)* and $Sr_3Co_2O_{6-\delta}$ *(I m m m)* noted.

Reitveld refinement using GSAS-II suite of programmes, was carried out on powder X-ray diffraction data of $Sr_{2-x}La_xCoO_{4-y}F_y$ compositions (K_2NiF_4 model with a space group *I 4 / m m m).* The unit cell parameter and goodness of fit parameters are shown in Table 7.1

Table 7.1. $Sr_{2-x}La_xCoO_{4-y}F_y$ unit cell parameters

X	Y	a/Å	c/Å	V/Å^3	wRp	Rp	χ^2
0.20	0.70	3.7968(1)	12.8537(6)	185.3	3.07	1.21	2.54
0.30	0.60	3.8003(7)	12.8052(4)	184.9	3.05	1.51	2.02
0.40	0.50	3.8014(6)	12.7816(3)	184.7	3.19	1.50	2.12
0.50	0.40	3.8033(4)	12.7318(1)	184.2	3.04	1.55	1.96
0.60	0.30	3.8004(2)	12.6402(1)	182.6	3.44	1.50	2.29

The unit cell volume was found to show a decrease upon increasing La content. This decrease in lattice parameters can be explained by the substitution of smaller La^{3+} for larger Sr^{2+} ions. What is interesting is the general trend of expansion in *a* and contraction in *c.*

Thermal expansion behaviours for $Sr_{2-x}La_xCoO_{4-y}F_y$ were measured by dilatometry up to 900 ^oC in air, Figure 7.4 and Table 7.2. The thermal expansion curve increase with temperature is linear, Figure 7.4 and Table 7.3.

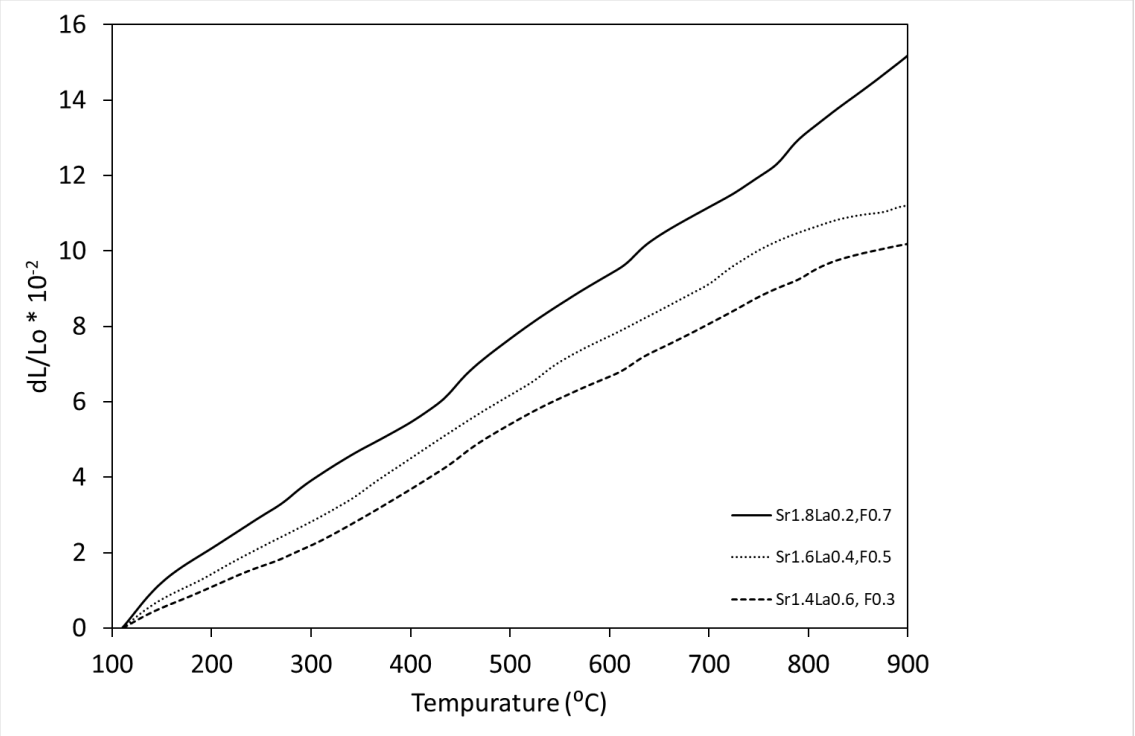

Figure 7.4. Thermal expansion curves of $Sr_{2-x}La_xCoO_{4-y}F_y$ and $Sr_2CoO_{4-\delta}$ in air.

Table 7.2 and 7.3: C_{TE} values of $Sr_{2-x}La_xCoO_{4-y}F_y$ and $Sr_2CoO_{4-\delta}$ in air.

X	y	Temperature range	C_{TE} (10^{-6})
0.20	0.70	110-900	19.23
0.40	0.50	110-900	14.18
0.60	0.30	110-900	12.90

	Temperature range	C_{TE} (10^{-6})
$Sr_2CoO_{4-\delta}$	110-440	15.55
	440-900	20.49
	110-900	18.43

La doping was shown to substantially the reduce thermal expansion behaviour with $Sr_{1.4}La_{0.6}CoO_{4-\delta}F_{0.7}$ having a similar value to fluorite electrolyte materials with relatively low C_{TE}, Table 7.4. When compared to other Co-based cathode materials, $Sr_{1.4}La_{0.6}CoO_{4-\delta}F_{0.7}$ had a far reduced C_{TE}. This is significant as a compatible thermal expansion behaviour to electrolyte materials can avoid polarization losses occurring.

Table 7.4: C_{TE} of $Sr_{1.4}La_{0.6}CoO_{4-\delta}F_{0.7}$ and other Cathode/Electrolyte SOFC materials

	C_{TE} (10^{-6})	Ref
$Sr_{1.4}La_{0.6}CoO_{4-\delta}F_{0.7}$	12.9	This Work
8YSZ	10.3	29,30
10GDC	12.1	31,32
$La_{1-x}Sr_xFe_{0.8}Co_{0.2}O_{3-\delta}$	15.4	33,34
$Pr_{0.6}Sr_{0.4}Co_{0.8}Fe_{0.2}O_{3-\delta}$	19.6	35
$PrBaCo_2O_{5+\delta}$	20.0-21.0	36-39

7.3.2 Conductivity Measurements

Conductivity measurements of $Sr_{2-x}La_xCoO_{4-y}F_y$ materials were measured by the 4 probe DC method in air, Figure 7.5.

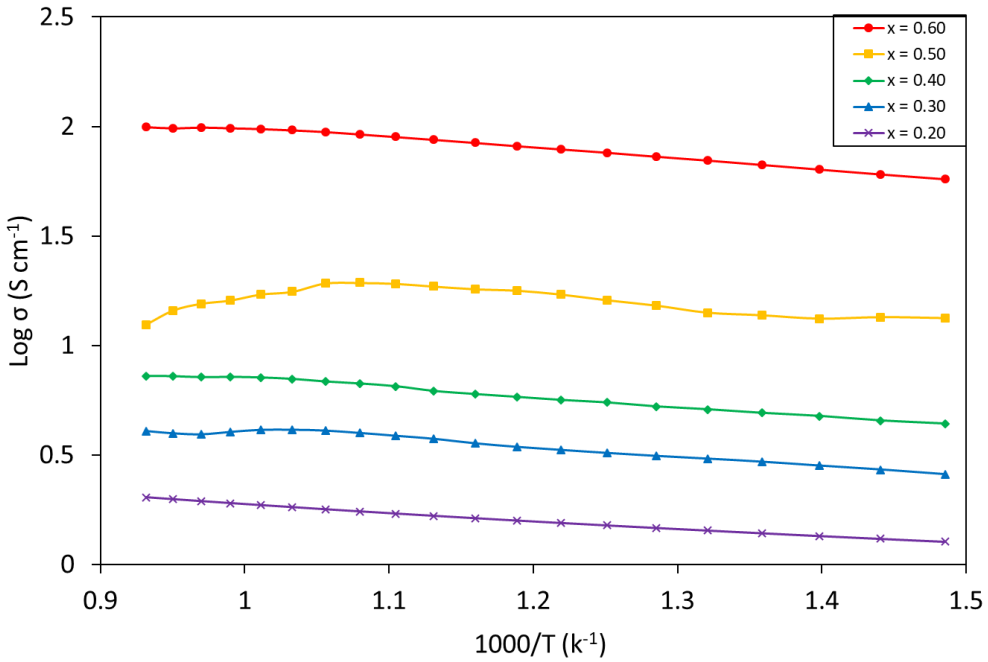

Figure 7.5. Plot of log σ versus 1000/T for $Sr_{2-x}La_xCoO_{4-y}F_y$

All samples were shown to have increasing conductivity as temperature increased until 675 ^oC where either the conductivity plateaued or decreased. The latter is most likely to do with the partial oxygen loss at higher temperatures. Total conductivity was shown to improve with increased La doping with the highest doped sample, $Sr_{1.4}La_{0.6}CoO_{4-\delta}F_{0.7}$ having the highest conductivity across the temperature range tested.

To highlight the effect of La doping and evaluate the materials potential as a SOFC cathode, Figure 7.6 shows the electrical conductivity of $Sr_{2-x}La_xCoO_{4-y}F_y$ at 600 ^oC in air.

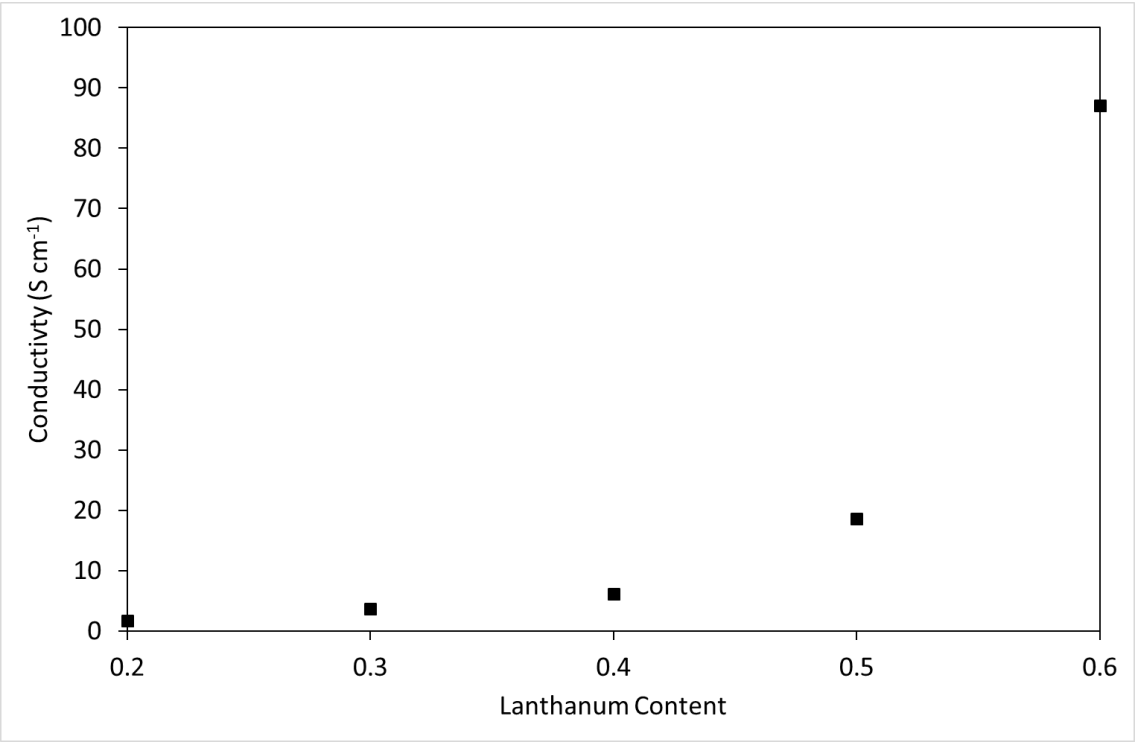

Figure 7.6. Electronic conductivity at 600 °C for $Sr_{2-x}La_xCoO_{4-y}F_y$

The results show a significant enhancement for in electronic conductivity for the highest La doped sample, with $Sr_{1.4}La_{0.6}CoO_{4-\delta}F_{0.3}$.

7.4. Conclusions

In this work we have shown that lanthanum could be incorporated into Sr_2CoO_3F, resulted in the formation of new K_2NiF_4 phases under ambient pressure. Analysis of thermal expansion behaviour showed that La doping substantially decreased C_{TE} to match values of studied SOFC electrolyte materials.

Conductivity measurements showed that there was an improvement for $Sr_{2-x}La_xCoO_{4-y}F_y$ materials on increased lanthanum incorporation with the highest doped material $Sr_{1.4}La_{0.6}CoO_{4-\delta}F_{0.7}$ showing the most promise. Further conductivity studies such as ASR should be considered to compare with other SOFC cathode materials. Further research into such materials is warranted for potential use of such materials as FIB electrodes.

7.5 References

1. James M.S., Slater P.R., Chim Ogg – Chem. Today **38**(6) 50-53 (2020)
2. Slater P., Driscoll L., Photonic and Electronic Properties of Fluoride Materials Chapter **18 (**2016)
3. Al-Mamouri M., Edwards P.P., Greaves C., Slaski M., Nature **369** 382 (1994)
4. Slater P.R., Journal of Fluorine Chemistry **117** 43-45 (2002)
5. Clemens O., Slater P.R., Rev. Inorg. Chem. **33** 105 (2013)
6. Moon E.J., Xie Y., Laird E.D., Keavney D.J., Li C.Y., May S.J. Journal of American Chemical Society **136(6)** 2224-2227 (2014)
7. Morgan-Ruiz A., Aritza W-M., Orera A., Sanjuan M. L., Larranga A., Slater P.R. Slater, Arriortua M., IUCrj **6** 128-135 (2019)
8. Clemens O, Wright A.J., Berry F.J., Smith R. I., Slater P.R., J. Solid State Chem 198 262-269 (2013)
9. Clemens O, Berry F.J., Bauer J., Wright A.J., Knight K. S., Slater P.R., J. Solid State Chem 203 218-226 (2013)
10. Berry F.J., Ren X., Heap R., Slater P., Thomas M.F., Solid State Communications, **134(9),** 621-624 (2005)

11. Hector A.L., Hutchings J.A., Needs R.L., Thomas M.F., Weller M.T., J.Mater Chem., **11** 527 (2001)
12. Hancock C.A., Herranz T., Marco J.F., Berry F.J., Slater P.R., J. Solid State Chem 186 195-203 (2012)
13. Nowroozi M.A., Wissel K., Rohrer J., Munnangi A., Clemens O., Chemistry of Materials **29(8)** 3441-3453 (2017)
14. Tsujimoto Y., Jun J.Li, Kazunari Y., Matsushita Y., Katsuya Y., Tanaka M., Shirko Y., Akaogi M., Takayama-Muromachi E., Chem. Commun **47** 3263-3265 (2011)
15. El Shinawi H, Marco J.F., Berry F.J., Greaves C., J. Mater Chem., **20** 3252-3259 (2010)
16. Rice D. E., Buttrey D.J., Solid State Chem. **105** 197-210 (1993)
17. Amow G., Skinner S.J., J. Solid. State. Electrochem., **10**(8) 538-546 (2006)
18. Munnings C.N., Skinner S.J., Amow G., Whitfield P.S., Davidson I.J Solid State Ion.**176**(23-24) 1895-1901 (2005)
19. Amow G. Davidson I.J., Skinner S.J., Solid State Ion **177**(13-14) 1205-1210 (2006)
20. Skinner S.J., Amow G., J. Solid State Chem **180**(7) 1977-1983 (2007)
21. Zhao F, Wang X.F., Wang Z.Y., Peng R.R., Xia C.R., Solid State Ion **179** (27-32) 1450-1453
22. Reddy A., Fichtner M., J. Mater Chem., **21** 17059-17062 (2011)
23. Nowroozi M.A., Ivlev S., Rohrer J., Clemens O., J. Mater Chem. A., **6** 4658-4669 (2018).
24. Wissel K., Dasgupta S., Benes A., Schoch R., Bauer M., Witte R., Fortes A.D., Erdem E., Rohrer J., Clemens O., J. Mater. Chem. A., **6** 22013-22026 (2018)
25. Aikens L.D, Li R., Greaves C., Chem. Commun., **21** 2129-2130 (2000).

26. Wissel K., Heldt J., Grosewicz P.B., Dasgupta S., Breeitzke H., Donzelli M., Waidha A.i., Fortes A.D., Rohrer J., Slater P.R., Buntkowsky G., Clemens O., Inorg Chem. **57**(11) 6549-6560 (2018)
27. Nowroozi M.A, Wissel K., Donzelli M., Hosseinpourkahvaz N., Plana-Ruiz S., Schoch R., Bauer M., Malik A.M., Rohrer J., Ivlev S., Kraus F., Clemens O., Commun Mater **1**(27) (2020)
28. Toby B.H., Von Dreele R.B., J. Appl. Crystallogr, **46** 544-549 (2013)

Chapter 8: Conclusions

In this thesis, the work presented focuses on the development of anion doping strategies (Oxyanions and Halides) into a variety of different structures for potential use as cathode materials within solid oxide fuel cells and electrolysers. The aim of the work was preparing and characterise new materials, as well as to improve our understanding of these doping strategies. Whilst none of the materials discussed meet the threshold of conductivity desired for a SOFC cathode, there is still interesting findings from this thesis.

Examining the use of phosphate doping of the mixed perovskite Mn/Fe system, $Sr_{2-x}Ca_xMnFeO_{6-\delta}$, to design a novel low-cost cathode material. The work shows the successful incorporation of phosphate into these systems and show that conductivities are higher than the previously reported silicon doped variant. However, overall the conductivities are still a low for potential SOFC/SOEC cathode material applications.

The work on $Ba_{1-x}Sr_xFeO_{3-\delta}$ systems demonstrates the successful incorporation of borate and characterises the effect on the structure and conductivity with a view to possible as ORR catalyst. The incorporation of low levels of borate was sufficient to cause a change in crystallography to form cubic perovskite structure. Once more, conductivity values were, however a little low for what is required for a SOFC cathode material.

In addition to electrode materials, a series of electrolyte materials were also studied. Lanthanum germanate apatite, an interesting new oxide ion conductive electrolyte was studied to confirm which mechanism are present within the $La_{10}Ge_6O_{27}$ and $La_{10-x}Y_xGe_6O_{27}$ (X = 0, 1 and 2) structure. There are two proposed mechanism yet while one is accepted the other remains controversial. Borate could be doped into the apatite which would block the centre channel, but conductivity remained high, adding support for an alternative oxygen

interstitial conduction method perpendicular to the channel was present. The addition of borate into the structure also introduced larger amounts of interstitial oxide ions, therefore increasing the conductivity of some of these systems.

Further work looked at alternative synthesis route for oxyanions incorporation into mixed metal oxides. The first use of two forms of biopolymer, Iota and Kappa Carrageenan as both a gelation agent and a precursor material were demonstrated with a novel sol-gel synthesis for the manufacture of $SrFe_{1-x}S_xO_{3-\delta}$ materials with the resulting products comparable to the standard high-temperature solid-state synthesis. This showed comparable results to the standard solid-state synthesis, highlighting the potential of the materials, and demonstrating that gelation agents are not always, simply burnt off.

Finally, the successful synthesis of a range of K_2NiF_4 structured La doped Sr_2CoO_3F phases was demonstrated. Unlike the synthesis of undoped Sr_2CoO_3F, which could only be achieved under high temperature and pressure, La doping was shown to help to stabilise the phase formation under ambient pressure. We also evaluated these materials, for their potential applications as SOFC cathode/ FIB electrode materials via conductivity and thermal characterisation, with $Sr_{1.4}La_{0.6}CoO_{4-\delta}F_{0.7}$ showing the most potential as a SOFC cathode materials form this thesis. Further studies are still warranted to determine whether this material could be used in either device.

Ultimately, no novel materials researched within this thesis can be considered too superior to the current state-of-the-art materials used as SOFC cathodes, or the target benchmark of 100 S cm^{-1} as can be seen in Table 8.1

Table 8.1: Results of highest conductivity per chapter at 700 °C

	S cm^{-1}
Benchmark	100
Chapter 3 ($Sr_2MnFe_{0.95}P_{0.05}O_{6-\delta}$)	16.48
Chapter 4 ($Ba_{0.90}Sr0_{.10}Fe_{0.95}B_{0.05}O_{6-\delta}$)	6.22
Chapter 6 ($SrFe_{0.95}S_{0.05}O_{3-\delta}$)	6.84
Chapter 7 ($Sr_{1.4}La_{0.6}CoO_{4-\delta}F_{0.3}$)	96.18

Chapter 9: Further Work

The current research indicated that anode doping strategies (Oxyanion and Halides) into a variety of different structures was possible and could lead to interesting structures and properties.

Conductivity measurements showed there was a general improvement for $(Ca/Sr)_2MnFeO_{6-\delta}$ materials on low level of phosphate incorporation, with a decrease at higher phosphate levels attributed to the presence of impurities as the P solubility limit was exceeded. The conductivities are superior to that of silicon doping and although are a little too low for Solid Oxide Fuel Cell / Electrolysers applications, further work is needed to try to improve conductivities, e.g co-doping with cobalt, and additional investigations as potential AFC catalysts.

Borate was to be successfully incorporated into $Ba_{1-x}Sr_xFeO_{3-\delta}$ and whilst the conductivity of both series of materials were rather low, it may be possible to raise this through co-doping with cobalt, and so there is still potential interest for SOFC's, as well as potential interest as an ORR (oxygen reduction reaction) catalyst in AFC's.

Borate was also shown to be able to incorporated within $La_{10-x}Y_xGe_6O_{27}$ (x = 0,1,2) resulting in the synthesis of new hexagonal apatite phases. The fact that significant oxide ion conductivities are observed despite the filling of the channels with borate provides supporting evidence for a secondary conduction pathway perpendicular to the central channel is as proposed by modelling studies. This work therefore provides experimental validation for prior modelling predictions of this conduction pathway. Furthermore, detailed neutron diffraction studies are warranted to gather detail of the orientation of the borate group in the channel.

The use of Iota and Kappa Carrageenan as both a gelation agent and sulphur dopant allowed for the formation of a range of $SrFe_{1-x}S_xO_{3-\delta}$ materials at a lower temperature and shorter time than the standard solid-state synthesis. The work suggests that the use of biopolymers as gelation/precursor materials may allow for the development of new oxyanion doped perovskite systems, or other oxyanion doped materials. There are also wider implications for the literature using Carrageenan or other biopolymers may be unwittingly incorporating additional dopants into materials.

Lanthanum was shown to be incorporated into Sr_2CoO_3F and resulted in the formation of new K_2NiF_4 phases under ambient pressure. Conductivity measurements showed that there was an improvement for $Sr_{2-x}La_xCoO_{4-y}F_y$ materials on increased lanthanum incorporation with the highest doped material $Sr_{1.4}La_{0.6}CoO_{4-\delta}F_{0.7}$ showing the most promise in terms of conductivity. Further research into such materials is warranted for potential SOFC cathodes, AFC catalyst or FIB electrode materials. Detailed structural studies are also warranted to clarify why La doping allows formation under ambient pressure, when undoped Sr_2CoO_3F can be prepared at high pressure.

Chapter 10: Conference List

H2FC Supergen Research Conference, Birmingham, United Kingdom	18/12/2018	Poster
15th International Hydrogen and Fuel Cell Conference, Birmingham, United Kingdom	19/03/2019	Poster
19th European Symposium on Fluorine Chemistry, Warsaw, Poland	25/08/2019	Poster
16th International Symposium on Solid Oxide Fuel Cells (SOFC XVI), Kyoto, Japan	08/09/2019	Talk
Postgraduate Symposium 2020, School of Chemistry, University of Birmingham	19/05/2020	Poster
Postgraduate Symposium 2021, School of Chemistry, University of Birmingham	20/06/2021	Talk
17th International Symposium on Solid Oxide Fuel Cells (SOFC XVI), Online Meeting	23/07/2021	Poster (x2)
Early Career Researcher Meeting, RSC Solid State Chemistry Group, Online Meeting	17/09/2021	Poster

Chapter 11: Publications List

A. D. Smith, M. S. James and P. R. Slater, *Effect of Si-doping on the structure and conductivity of $(Sr/Ca)_2MnFeO_{6-\delta}$ systems,* ECS Transactions, **91**(1), 1425-2436 (2019)

M. S. James and P. R. Slater, *Synthesis and characterisation of fluorine containing perovskite and related phases using polymer reagents,* Chimica Oggi/Chemistry Today, **38**(6), 50-53 (2020)

M. S. James, F. J. Berry, J. F. Marco and P. R. Slater, *Synthesis and Characterisation of P-Doped $Sr_2MnFeO_{6-\delta}$ systems,* ECS Transactions, **103**(1), 2185-2194 (2021)

S. W. Thomas, M. S. James, M. P. Stockham, J. Deakin, A. Jarvis and P. R. Slater, *Synthesis of Borate doped $La_{10}Ge_6O_{27}$: Confirming the Presence of a Secondary Conducting Pathway,* ECS Transactions, **103**(1), 1885-1897 (2021)

M. P. Stockham, B. Dong, M. S. James, Y. Li, Y. Ding and P. R. Slater, *Water based synthesis of highly conductive $Ga_xLi_{7-3x}La_3Hf_2O_{12}$ garnets with comparable critical current density to analogous $Ga_xLi_{7-3x}La_3Zr_2O_{12}$ systems,* Dalton Transactions, **50**(7), 2364-2374 (2021)

M. P. Stockham, B. Dong, M. S. James, Y. Li, Y. Ding, E. Kendrick and P. R. Slater, *Evaluation of $Ga_{0.2}Li_{6.4}Nd_3Zr_2O_{12}$ garnets: exploiting dopant instability to create a mixed conductive interface to reduce interfacial resistance for all solid state batteries,* Dalton Transactions, **50,** 13786-13800 (2021)

B. Dong, A. R. Haworth, S. R. Yeandel, M. P. Stockham, M. S. James, J. Xiu, D. Wang, P. Goddard, K. E. Johnston and P. R. Slater*, Halogenation of $Li_7La_3Zr_2O_{12}$ solid electrolytes: a*

combined solid-state NMR, computational and electrochemical study, Journal of Materials Chemistry A, **10,** 11172-11185 (2022)